# 博士論文

Wall Chemical Effect on Low Temperature

Oxidation in Weak Flame

(Weak Flame の低温酸化反応における壁面の化学的

効果)

万　遂

# Acknowledgement

Foremost, I would like to express my deepest gratitude to my supervisor, Prof. Y. Suzuki, for the continuous support and guidance of my Ph.D. study and research, for his patience, motivation, enthusiasm, and immense knowledge. He is always patient with the mistakes and failures, and encourages me to analysis the causes and conquer the difficulties. He has not just guided me to finish my dissertation, but also taught me how to become a researcher.

Besides my supervisor, I would like to thank the rest of the committee: Prof. M. Tsue, Prof. S. Maruyama, Prof. S. Takagi, Prof. J. Shiomi and Prof. K. Maruta, for their valuable questions and insightful comments.

My sincere thanks also goes to Prof. O. Deutschmann and Prof. J. Kubota, for offering me the opportunities to visit their groups and giving constructive advices on surface reaction mechanism development. Special thanks go to Prof. Y. Saiki for his guidance in laser diagnostics and surface chemistry.

I am grateful to the other faculties in MESL Lab., Prof. K. Morimoto and Prof. Y. Fan, for valuable discussions and constructive suggestions in my research. Prof. K. Morimoto guided me into simulation as far back as my master study, and offered me many helps on managing the simulation platform. Prof. Y. Fan supported me all the way in my Ph.D. study. I would never gain so many results in this limited time period without his assistance. I also would like to express my thanks to Y. Hamana and Y. Goda for their assistance on all detailed issues.

I have spent 5 years in MESL Lab., ever since I got enrolled as a master student. I really appreciate the companies of all my fellow lab-mates, including both current and previous members. In particular, I like to thank M. Lee for all the helps and discussions for combustion study. I would also like to extend my gratitude to S. Oh, Y. Chen, R. Chen for teaching me film deposition related techniques. I also appreciate the helps I received from C. Yeh, A. Zhao and H. Kinoshita for setting experimental and simulation environments.

Last but not the least, I would like express my sincere thanks to my family and friends. The company of my friends is very precious to me. My life becomes more colorful with their presences. The enduring love and support I received from my parents and my grandmother is always the driving force for me to step forward. There

are not enough words to thank them. During my Ph.D. study, I am very blessed to meet the most important person in my life, J. Gollenstede. His love is the constant source for my happiness.

# Abstract

The economic, social and cultural development of our entire human society is highly depended upon a consistent supply of energy, and combustion technology is and will still be the backbone of energy conversion processes. More fundamental understandings of the underlying sub-processes and their mutual interaction in the complex combustion system are indeed needed. Flame-wall interaction (FWI) is one specific problem that demands our great attention. Wall surface acts as both a heat sink and a surface reaction site for species, which may quench the flame due to the decreased flame temperature and the reduced number density of active intermediates. These phenomena are referred as wall thermal and chemical effect respectively. Previously studies with the methane normal flame suggested that the wall chemical effect only exert influence on the flame with high wall temperature (> 1000 K), while wall thermal effect is dominant for low temperature wall. Since for most of the applications, e.g. engine, the wall temperature is hard to reach 1000 K, wall chemical effect has been considered as negligible for many studies.

However, the above conclusion is only given for the high-temperature oxidation (with high gas-phase temperature and reactivity). The wall chemical effect on the low-temperature oxidation (with low gas-phase temperature and reactivity) has not been investigated before. The low-temperature oxidation is the process that prepared the radical pool for the thermal ignition, thus it has a significant influence on ignition control, engine knocking control and emission reduction. Investigation of the wall chemical effect on low temperature oxidation provided an important opportunity to advance our knowledge of the flame-wall interaction during the ignition process.

The weak flame is chosen as the target flame, since it is a stable flame, but has the same characters as the ignition process. In this thesis, the species (DME, CO, $CO_2$, HCHO and OH) distributions of the weak flame in the channel with different wall materials have been measured with gas chromatography (GC) and planar laser-induced fluoresces (PLIF) system. Numerical simulations with detailed gas-phase and surface reactions have been conducted to compare with the experimental data. New surface reaction model has been proposed to reproduce the phenomenon observed in experiments.

This work begins by the development of a detachable rectangular micro flow reactor with a streamwise temperature gradient. Instead of using a circular quartz tube

as in previous studies, a rectangular quartz channel with a detachable wall is adopted for a better optical access and for the thin film deposition on the channel inner surface. The flame response to the mean inlet flow velocity is examined in this rectangular channel, and compared with the result from previous study. The HCHO and OH-PLIF is used to visualized the weak flame, flame with spatially separated low- and high-temperature oxidation zones, checking whether the weak flame is well established or not in the rectangular channel developed for this work.

The radical quenching phenomenon, which has reported for the normal flames, has been examined for the weak flame. Alumina or SUS321 film has been coated on one channel sidewall. The OH wall normal distribution, measured with OH-PLIF, in such an asymmetric channel was compared with that in the pure quartz channel. Comparing the experimental data with the simulated results, the initial sticking coefficients ($S_0$) for alumina, quartz and SUS321 in the weak flame have been estimated and compared with previous estimated value from the normal flame. Sensitivity analysis has been conducted for both weak and normal flame to identify the weight of each adsorption reaction on the OH distribution.

Quartz has been identified as more close to inert material for radical quenching in the weak flame. SiC, SUS321 and Inconel600 have been identified as active to radical quenching in previous work. Thus these materials have been chosen as the typical materials for illustrate the wall chemical effect on cool flame. To further understand the effect of individual component in the alloys, Fe, Ni and Cr are also been tested. SiC, SUS321, Inconel, iron, nickel and chromium are coated as thin films on the both sidewalls of the quartz channel. DME is measured by the gas chromatography-mass spectrometer (GC-MS), while CO and $CO_2$ are measured by the GC with thermal conductivity detector (TCD). OH and HCHO distribution in the quartz and SUS321-coated channel are measured with the planar laser-induced fluorescence (PLIF). The species streamwise distributions in channel with different wall materials are compared to investigate the wall chemical effect on weak flame.

Numerical simulations with detailed gas-phase and surface reactions haven been done to compare with the experimental phenomenon. Firstly, radical quenching model is attempted to describe the wall chemical effect on the species streamwise distribution in the SUS321-coated channel. Since SUS321 has around 10% Ni, the surface reaction of Ni is adopted as a base for developing the new model. Based on the experimental data, two hypotheses have been proposed for SUS321: DME

synthesis and HCHO adsorption. The proposed surface reaction mechanism is also applied to the wall-stabilized cool flame, to examine the wall chemical effect on other flame structure.

This work provides the very first evidence that wall materials will affect both low- and high-temperature oxidation. The experimental results are remarkable, because previous studies suggested that wall chemical effect is weak with the low wall temperature (< 1000 K), however, present work shows that wall materials affect the low-temperature oxidation even when wall temperature is only 600 K. In the other words, the wall chemical effect may not be negligible in practical applications as engine, even when the operating wall temperatures are low. The surface reaction over alloy or metal surface may affect the low-temperature oxidation, further leading to an ignition delay for the hot flame. Some hypotheses for the surface reaction mechanism have been proposed for the SUS321 surface, but further research is needed for completing the surface reaction model.

# Contents

# List of Figures

# List of Tables

# Chapter 1 Introduction

## 1. 1. Internal Combustion

### 1. 1. 1.  Energy Outlook

It can be said without exaggeration that nowadays our world is built around the fossil fuel, which supplies much of the energy needs of our society and the industrial revolution. However, with an urgent need of energy supply, the world fossil fuel consumption has outpaced newfound reserves. According to the statistics published in 2016, energy demand of the world will grow more 30% by 2035 [1] as shown in Figure **1-1**. To address this issue, various efforts has been made, and the global energy map is changing due to a retreat from nuclear power in some country, continued rapid growth in the use of solar and wind technologies and the boosts of unconventional gas production. However, in spite that all those new developments and policies are involved, and regardless of the growth in low-carbon energy sources, fossil fuels, without any doubts, are still dominant in the energy structure. In 2015, fossil fuels contribute to 85% of the global primary energy consumption, and the share will remain to be 78% till 2035 according to the prediction [1]. Moreover, even the share is decreasing, but the total demand will not stop increasing.

In order to solve the sustainability problem, a lot of efforts have been made for the penetration of renewable energy. Renewables is the fastest growing energy source nowadays. Their share of the primary energy consumption will grows from 3% in 2015 to 10% in 2035 [1]. The renewables include solar, geothermal, wind power, hydropower, biomass and biofuels. Figure **1-2** gives the U.S. renewable energy supply summary [2]. It is apparent that biomass and biofuels take a considerable share of the renewable energy supply. In 2016, biofuel contribute to 14% share, while 23% share is contributed from biomass.

The increasing energy demand is a consequence of the fast-growing economy. Without hurting the economy growth, improving the energy efficiency is acknowledged as an alternative to reduce the consumption. Figure **1-3** [1] shows the energy intensity changes in the past 50 years. The world's energy intensity is keep declining, and expected to reach half of the value in 1965 by 2035. Since the chemical

energy in the primary energy as fossil fuel, biomass and biofuels are converted to other energy forms by the combustion process, a better understanding of the combustion phenomenon will be a great help for improving the energy efficiency. On the other hand, combustion of hydrocarbon fuels, as the main source for the $CO_2$ emission, the study of combustion is also critical for reversing the climate change tendency.

**1. 1. 2. Energy Conversion for Vehicle**

The increasing transport demand drives the continual growth of energy demand, especially for oil. As shown in Figure **1-4** [1], transport is one of the largest markets for final energy consumption, which accounts for nearly 20% of the total consumption. According to the forecast shown in Figure **1-5** [1], the global car fleet is expected to double from 0.9 billion cars in 2015 to 1.8 billion by 2035, and the non-OECD countries, including China and India, will attribute to 90% of the increment.

Recent years, many efforts have been made for the electric vehicle and the fuel cell vehicle development, considering them as alternates of conventional internal combustion engine cars. As shown in Figure **1-5**, the number of electric vehicle will rise significantly from 1.2 million in 2015 to 100 million by 2035, but still 94% of the vehicles will remains to be the conventional cars in 2035 [1]. Limited by current technologies, the costs of both electric and fuel cell vehicles are high, which is a fatal weakness considering the major transport demand is coming from the developing countries. Not mention that the electric and fuel cell vehicles are facing the criticism of low efficiency and carbon emission during the electricity generation or $H_2$ production for the fuel cell. Moreover, the improvements in fuel efficiency significantly reduced their potential growth. Therefore, there are reasons to believe that internal combustion engine will still be the dominant energy conversion technology for vehicle for not a short time.

**1. 1. 3. HCCI Engine**

Homogeneous charge compression ignition (HCCI) engine has been considered as one of the ultimate combustion engines due to it feature of ultra-low emission and high efficiency. A comparison of HCCI engine and the conversional compression-ignition (CI) engine and spark-ignition (SI) engine is given in Figure **1-6** [3]. The

biggest difference is that in HCCI engine, ignition happens simultaneously at multiple positions, therefore, it is not necessarily limited by the mixing rate at the fuel jet and oxidizer interface as the CI engine, and also do not have any discernible flame front and localized high-temperature reaction region as the SI engine [4]. This feature allows the HCCI engine operating in a lean and low-temperature condition, which can avoid the soot and NOx formation as shown in Figure **1-7** [5]. However, because of the multiple-point ignition, the ignition control becomes one of the principal challenges for the HCCI engine. And in the meanwhile, due to the homogenous gas-phase reaction in the whole chamber, the flame-wall interaction may also been enhanced.

## 1. 2. Flame-Wall Interaction

The mutual interaction between flame and wall is not avoidable in all types of internal combustion system regardless the scale. The chemical kinetics in the gas-phase is heavily influenced by the presence of wall, and so as the flow field. Figure **1-8** (reproduced form [5]) illustrates the most prominent interaction among the flame, wall and flow field. Wall surface acts as both a heat sink and a surface reaction site for species, which may quench the flame due to the decreased flame temperature and the reduced concentration of active intermediates. These phenomena are referred as wall thermal and chemical effect on the flame respectively. The wall also impacts the approaching flows as the boundary layer forms. In the meanwhile, the near-wall species concentration not only governed by the chemical kinetic but also the species transportation, which is under the control of the flow field. And the near-wall species concentration turns to determine the surface reaction rate. Understanding flame-wall interactions (FWI) based on studying of thermal, fluidic and chemical kinetic properties is of fundamental importance for near-wall flames in all kinds of internal combustion systems [7].

### 1. 2. 1. Flame Quenching

Figure **1-9** [8] demonstrated three typical types of flame quenching: head-on quenching (HOQ), sidewall quenching (SWQ) and quenching in tubes. Flame quenching in tubes with high surface-to-volume ratio has been a bottleneck of micro

3

combustor development for decades. To establish stable combustion in small channels, both thermal and chemical approaches have been proposed. The concept of excess-enthalpy combustion by using heat recirculating burners such as Swiss-roll combustor is proposed by Weinberg et al. (shown in Figure **1-10**), aiming to stabilize the flame by increasing the temperature [9]. On the other hand, catalytic reaction is introduced into the Swiss-roll combustor [10], to promote the reactivity.

The head-on quenching and sidewall quenching have received great attention, since they are highly related to the incomplete combustion caused primary pollution generation in the internal combustion engine and gas turbines. A. Bohlin et al. [11] measured the near-wall temperature development during the ignition in a HOQ case. As shown in Figure **1-11**, the near-wall gas-phase temperature is increased due to the flame propagating towards the wall surface, but cooled down due to the heat loss to the wall, and finally caused the flame quenching in the near-wall region. To further understand the thermo-chemical state during flame-wall interaction, T. Fuyuto et al. measured the near-wall OH, HCHO and CO concentration as well as temperature for a SWQ [12] (shown in Figure **1-12**); M. Mann et al. observed the CO concentration development for a HOQ including both laminar and turbulent cases [13] (shown in Figure **1-13**). The near-wall species concentration may be under the influence of both wall thermal and chemical effect: the near-wall temperature determines the gas-phase kinetic; while the surface acts as a sink or a source for the gas species via adsorption or desorption. It is necessary to decouple these two effects to have a better understand of the FWI.

## 1. 2. 2. Wall Thermal/Chemical Effect

Numerous studies have attempted to investigate the explicit quenching mechanism and reveal the interaction between thermal and chemical effect. Miesse et al. [14] and Kim et al. [15] measured the quenching distance of methane flame separately. Their results, shown in Figure **1-14** and Figure **1-15**, are consistent with each other and suggested that the thermal quenching caused by heat loss is dominant when the wall temperature is lower than 500 ˚C; while the radical destruction becomes more important for higher wall temperatures. However, bulk materials have been used in these two studies, which raise the doubts on the different wall thermal boundaries due to the different thermal conductivity. Instead of using bulk materials, Y. Saiki et al.

developed a narrow combustion channel using quartz plates with thin film deposition of different materials to achieve the identical thermal boundaries for different chemical boundary conditions, and made OH-PLIF measurement of the methane flame [16][17]. As shown in Figure **1-16**, the near-wall OH concentration is identical over different wall materials at low wall temperatures, but becomes different when the wall temperature is over 700 ˚C. In the meanwhile, to characterize the wall materials, initial sticking coefficients, $S_0$, for alumina, quartz and SUS321 are estimated to be 0, 0.01 and 0.1, respectively [17]. Similar experiment has been done for SiC. The estimated $S_0$ is 0.04, as shown in Figure **1-17**, which is closer to the SUS321 results [18].

## 1. 3. Flame Chemistry

New combustion technologies, usually at extreme conditions, often lead to new flame regimes, and break our traditional cognition of the flame chemistry. As such, it is of great importance to advance our fundamental understanding of combustion chemistry. For instant, HCCI engine, as mentioned in section 1.1.3, is expected to operate in the ultra-lean and low temperature conditions. And since the ignition is happening at multiple points, the understanding of chemistry during the ignition process is critical for the combustion phase control.

### 1. 3. 1. Low- & High-Temperature Oxidation

When a fuel has a chain length over 3, a very clear distinction between the types of dominate reactions can be found when temperature rise from below 850 K to beyond 1200 K [19]. If we examine it more carefully, three regimes with respect to temperature can be divided for hydrocarbon oxidation path: (a) low temperature regime, where peroxy oxidation chemistry occurs; (b) intermediate temperature regime, where $HO_2$ and $H_2O_2$ chemistry dominates; (c) high temperature regime, where small size radical chemistry occurs [20]. One example is given in Figure **1-18** [21][22], in which the overall reaction scheme for DME oxidation is illustrated. When the gas-phase temperature is not high enough (< 600 K), fuels cannot directly undergo the $\beta$-scission, but the H atom abstraction takes place. The peroxy oxidation then occurs after the isomerization. With an increased temperature to a range around 600 ~

750 K, $\beta$-scission starts but more stable species such as $HO_2$, $H_2O_2$ and HCHO instead of OH radical are generated, leading to the negative temperature coefficient (NTC) region. As the temperature is further increased, fuels can directly undergo the $\beta$-scission, and more OH is formed from the decomposition of $H_2O_2$, which finally leads to the thermal ignition.

### 1. 3. 2. Cool Flame

Associated with the low and intermediate temperature oxidation, cool flame, a flame accompanied by pale chemiluminescence and low heat release rate, was first reported by Humphry in 1812 [23] and named by Emeleus in 1929 [24]. The cool flame prepares the radical pool for the thermal ignition. As such, the cool flame has been identified as an important contributing factor for ignition control, engine knocking, and other issues related to the unexpected auto-ignition phenomenon. Figure **1-19** illustrates an ignition process of a DME-HCCI engine, operating with an equivalence ratio of 0.28 [25]. A two-stage ignition can be seen from the simulated pressure and heat release rete (HRR) profile, as the first HRR peak locates at the crank angle of 340º, and the second one locates at 360º. The experimental measured species concentration shows that HCHO has a high concentration between the two ignitions in the negative temperature coefficient (NTC) region, while OH is largely generated during the second ignition due to the high temperature oxidation. Ignition delay measurement with shock tube is widely used to examine the low-temperature oxidation mechanism [26]. Figure **1-20** gives the typical pressure and CH emission profiles for a shock tube experiment, in which the pressure and the emission signal rising marks the ignition delay for a certain operating condition. By further comparing the data with the simulated ignition delay, as shown in Figure **1-21** [26], modification of chemistry kinetic can be done.

However, it is not easy to track the gas-phase temperature history and investigate the concentration of different species in such a short time scale. Therefore, researches have been made to obtain a stabilized cool flame. Y. Ju and his group [28][29] used ozone to establish a self-sustaining cool diffusion flame with an experimental setup shown as Figure **1-22** (a). It can be seen in Figure **1-22** (b) and (c), once it had been ignited, the cool flame can sustain even after turning off the ozone addition. K. Maruta and his group [30][31][32] discovered the weak flame in a micro flow reactor

with a controlled temperature profile. In the weak flame, reactions in different temperature level can be spatially separated.


### 1. 3. 3. Flame Chromatography

Figure **1-23** shows a micro flow reactor with a prescribed temperature profile, which adopted by K. Maruta and his group as a flame chromatography [31]. Three flame patterns can be found in this reactor as shown in Figure **1-24**: 1) when flow velocity is over 30 cm/s, a stable normal flame appears; 2) when flow velocity is between 4 cm/s to 30 cm/s, unstable dynamic oscillatory combustion was observed; 3) when flow velocity is lower than 4 cm/s, a stable weak flame with weak luminescence which is marked as the multiple reaction zones were observed [31].

In the weak flame, the first reaction zone is the cool flame, where the low temperature oxidation happens. After the cool flame, an NTC zone can be seen, as no luminescence can be noticed. The second reaction zone is referred as a blue flame, where intermediate species, as HCHO and $H_2O_2$, are consumed, and lead to a thermal ignition, in where the third reaction zone, hot flame, locates. The weak flame has the same characters as the ignition process, which is an ideal tool for chemistry kinetic study.


## 1. 4. Objective and Outline of This Thesis

### 1. 4. 1. Objective and Approaches

Flame-wall interaction and low-temperature oxidation are two important aspects to understand the combustion phenomenon. Previous studies of flame quenching reveal that, for a hot flame, the wall thermal effect is dominant when the wall temperature is low. The wall chemical effect only exerts influence when the wall temperature is over 700 K. Since for most of the applications, especially for macro scale combustors, the wall temperature is hardly to reach such a high level, the wall chemical effect is usually neglected. This is reasonable because in high-temperature oxidation, the gas-phase reactivity is much faster than the surface reactions over a cold wall, so the effect of surface reaction is minor. Moreover, the high gas-phase temperature leads to a high heat loss between the flame and the wall, which makes the thermal effect to be dominant. However, new combustion technologies, as the HCCI engine, lead to new

operating condition, which may break the convectional cognition. In the HCCI engine, the combustion is happened at low temperatures, and the flame is ignited homogenously in the whole chamber, which may close to the wall surface. Due to the low gas-phase temperature, the wall thermal effect is suppressed due to the smaller temperature difference between the gas-phase and the wall. In the meanwhile, when the ignition happens close to the wall, the cool flame will interact with the wall surface. Since the gas-phase reactivity of the cool flame is much lower than that of the hot flame, the surface reaction rate may become comparable to the gas-phase reaction. Therefore, the wall chemical effect may be of great importance of the ignition control. As such, it is worth to investigate weather wall chemical effect is important for low temperature oxidation or not.

The weak flame in the micro flow reactor is an ideal tool for study the wall chemical effect on the low temperature oxidation, since a stable cool flame can be established, in the meanwhile, the micro reactor offers a large surface-to-volume ratio. Therefore, the objective of this study is to reveal the wall chemical effect on the low-temperature oxidation by examine the influence of wall materials on the weak flame. It may shed some important insights on the flame-wall interaction for the ignition process as well.

The approaches in this work for this specific objective include the development of the flow channel, experimental measurements and numerical simulations. A micro flow reactor with a better optical access and with different wall materials is developed in order to investigate the wall chemical effect under the same thermal boundary conditions. In the weak flame established in the micro flow reactor with the steamwise temperature gradient, the species distributions, including DME, CO, $CO_2$, HCHO and OH, are measured with gas chromatography. Planar laser induced fluorescence measurements of OH and HCHO are also made to capture spatial distribution of those species for different wall materials. In addition, numerical simulations with detailed gas-phase and surface reaction mechanisms are made for discussion of possible mechanisms of the wall chemical effect on the flame structures.

### 1. 4. 2. Outline

Contents in this thesis is arranged as following:

In Chapter 1, previous studies about the flame-wall interaction and the low-temperature oxidation have been reviewed. Extensive research has shown that existence of the wall quenches the hot flame and causes the increased emission level. And the wall thermal effect has been considered as the dominant reason for the hot flame quenching when wall temperature is low. On the other hand, the cool flame, as an expression of the low-temperature oxidation, has been identified to be critical for ignition control. However, there has been no existing study, which investigates the chemical interaction between the cool flame and the wall. The present study attempts to reveal the wall chemical effect on the low-temperature oxidation with both experimental and numerical mythologies, which may shed a new insight on the wall effect on the ignition.

In Chapter 2, a rectangular micro flow reactor with a streamwise temperature gradient is introduced. Comparing with the circular tube reactor in previous studies [30][31][32], a better optical access and the variable wall chemical boundaries can be obtained. The flame response to the inlet flow velocity has been examined and compared with previous study, to ensure the weak flame can be established in this rectangular channel.

In Chapter 3, the radical quenching effect has been examined in the hot flame of the weak flame. Quartz, alumina and SUS312 have been chosen as the three typical wall materials. By comparing the measured OH distribution in the weak flame with the simulated results, the initial sticking coefficients in the radical quenching model have been estimated for different materials. The values have been compared with previous results with the normal flame. And the sensitivity analysis for the radical quenching model has been done for identify the critical reactions.

In Chapter 4, DME, CO and $CO_2$ distributions have been measured in the quartz, SiC-coated, SUS321-coated and Inconel600-coated channels with either GC-MS or GC-TCD. For further understanding of the role of individual metal, the DME distributions in the Fe-, Ni- and Cr-coated channel have been also measured with GC-MS. HCHO and OH distributions in the quartz and SUS321-coated channel have been also examined with a PLIF system. Influence of the wall materials on the weak flame has been discussed.

In Chapter 5, the surface reaction mechanism for SUS321 has been discussed. A reaction pathway analysis is conducted with DETCHEM Batch, showing the possible path for the higher DME concentration in the SUS321-coated channel. Radical

quenching model has been examined. To reproduce the experimental results, hypotheses have been proposed. The proposed surface reaction mechanism has been verified with the FLUENT 2-D simulation. The surface reaction model has also been applied to the wall-stabilized cool flame, showing the wall chemical effect may influence the flame structure other than the weak flame as well.

The conclusions are given in Chapter 6.
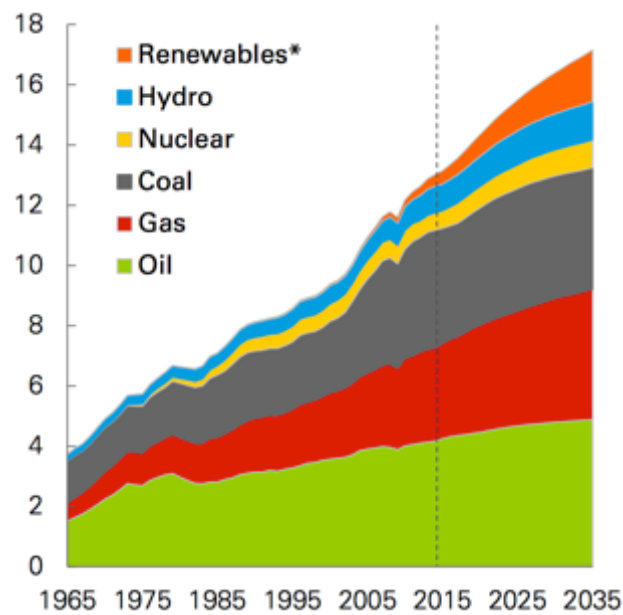
Figure 1-1 Primary energy consumption by fuel [1].

## U.S. renewable energy supply
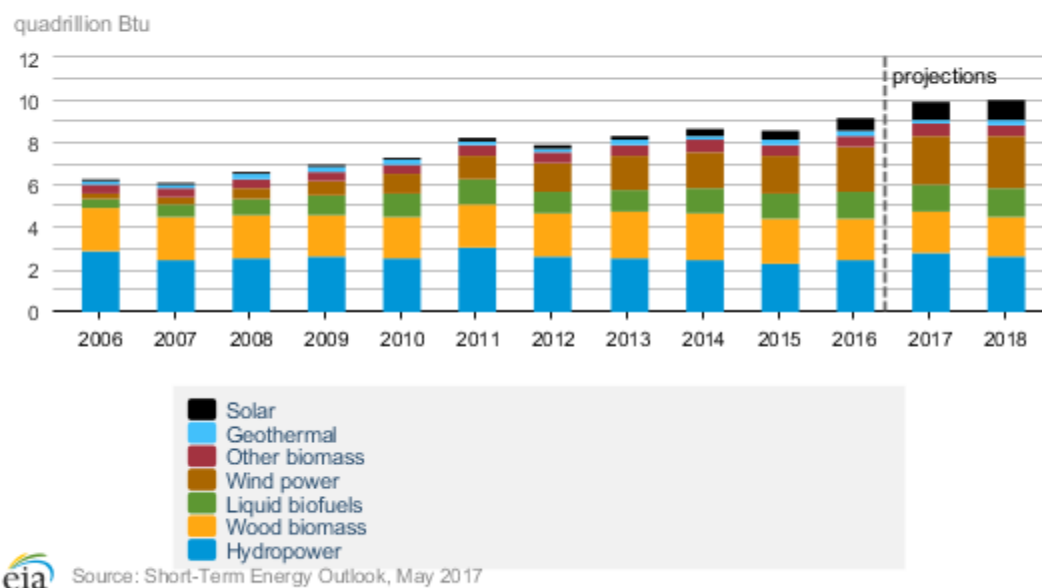
Figure 1-2 U.S. renewable energy supply [2].
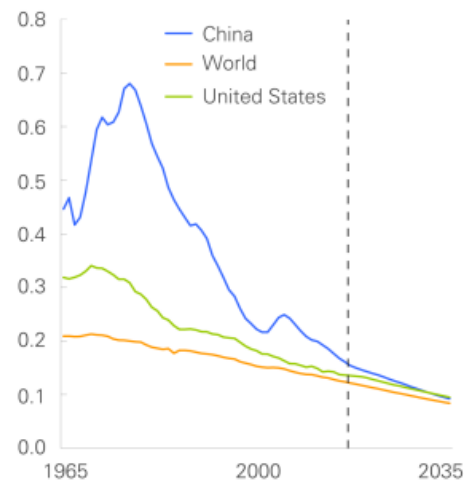
Figure 1-3 Energy intensity (toe per thousand - $2010 GDP) [1].
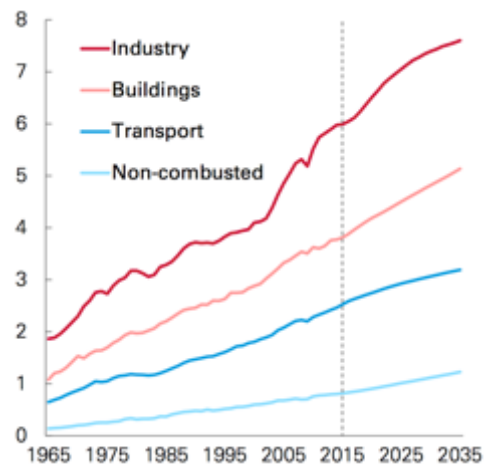


Figure 1-4 Total energy consumption by final sector [1].
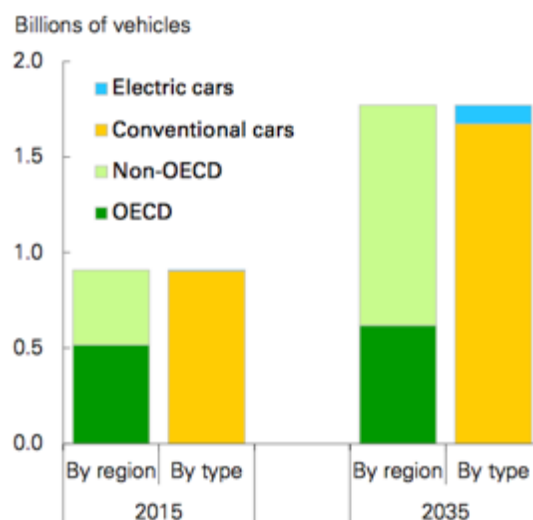


Figure 1-5 The global car fleet: 2015 -2035 (billions) [1].
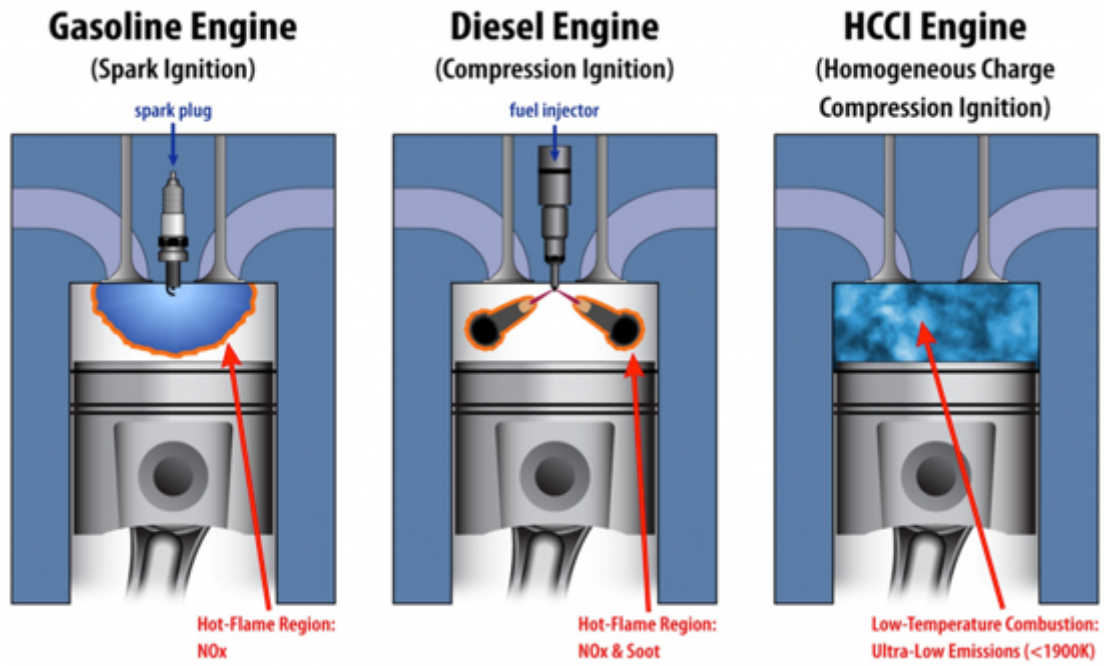
Figure 1-6 Different types of engine [3].
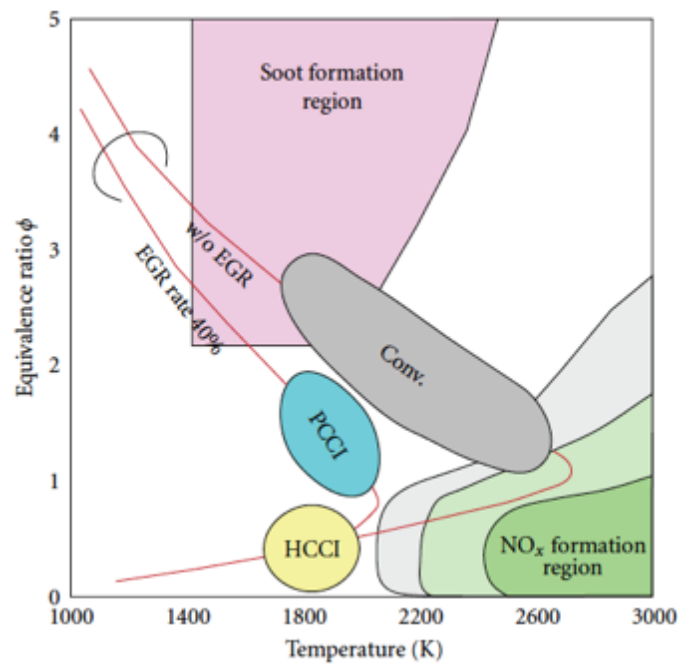


Figure 1-7 NO$_x$-soot map of conventional diesel, PCCI and HCCI combustion [5].
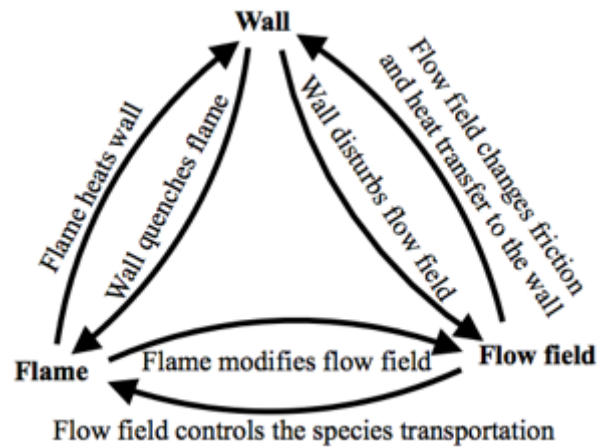
Figure 1-8 Illustration of mutual interactions between flame, wall and flow field. Reproduced from [6].
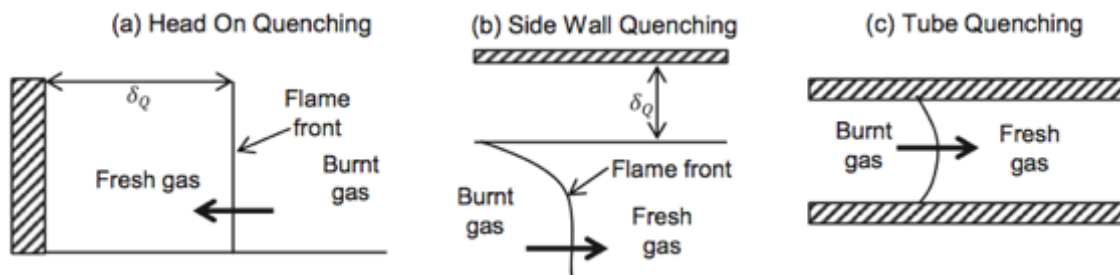


Figure 1-9 Sketches of quenching configurations [8].
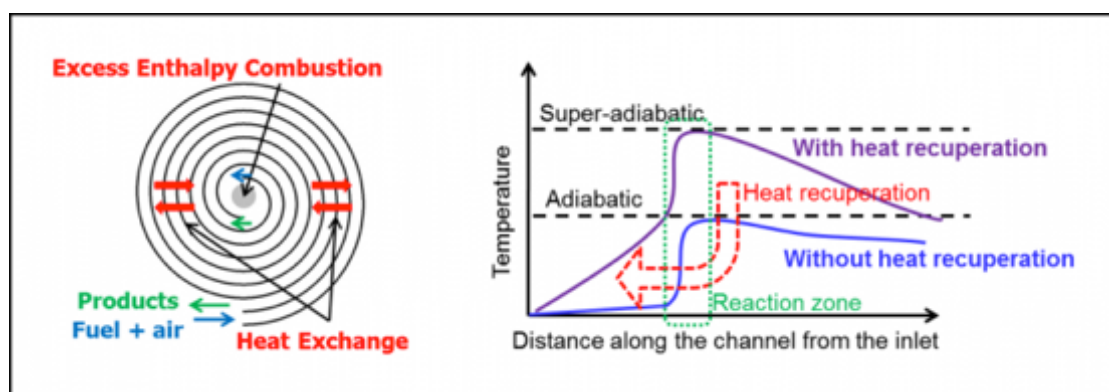


Figure 1-10 Left: Schematic of Swiss-roll combustor. Right: Illustration showing how super-adiabatic combustion temperatures can be achieved. [9]
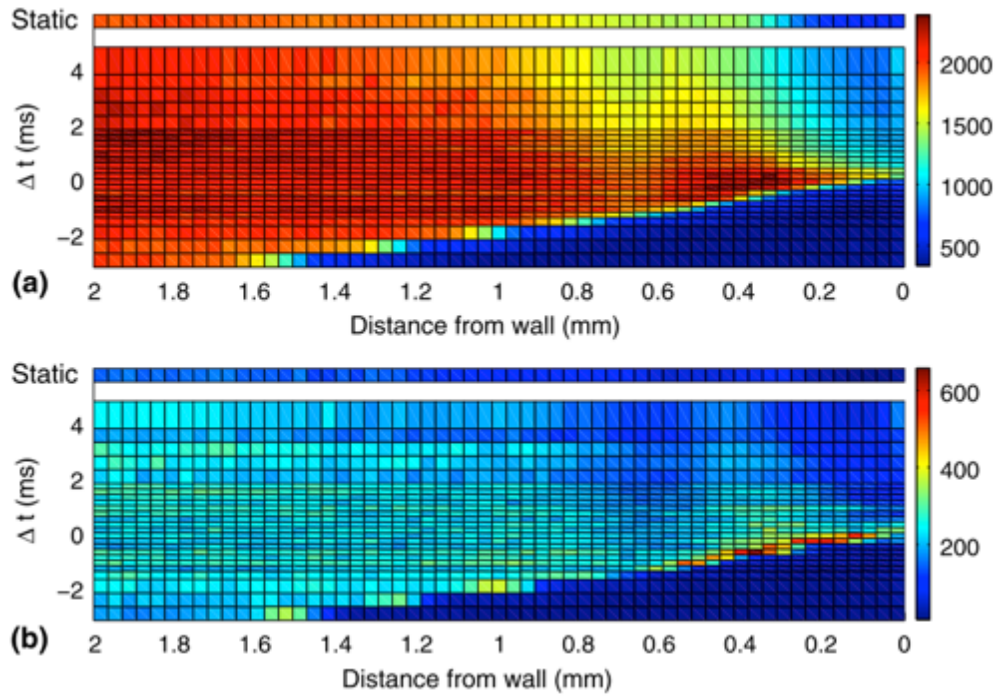
Figure 1-11 (a) Evaluated 1D mean temperature profiles as a function of ignition delay time. Equivalence ratio U = 1.0. Each profile is averaged from 100 single shots. (b) Standard deviation of the evaluated temperatures. [11]
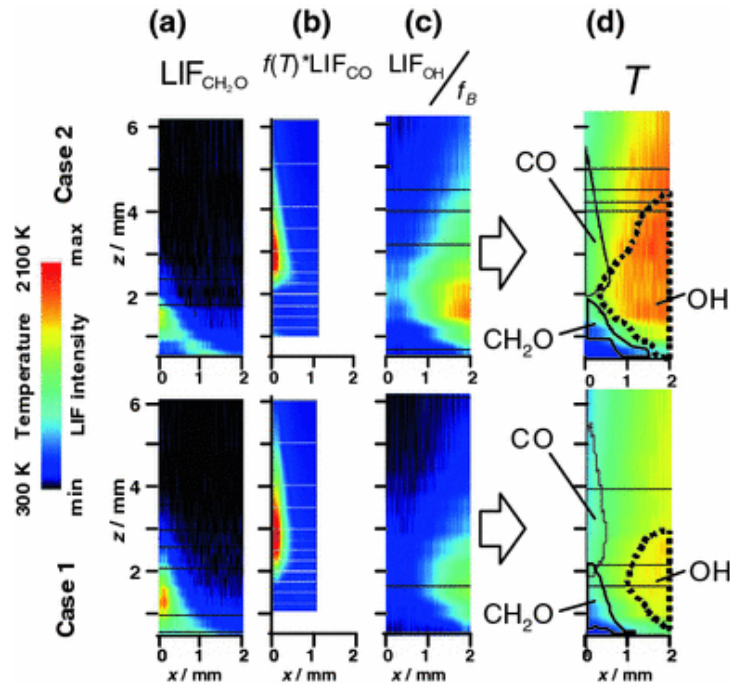


Figure 1-12 LIF signal distribution of measured species in the quenching boundary layer. Case 1: U = 0.1 m/s; Case 1: U = 0.2 m/s. [12]

15
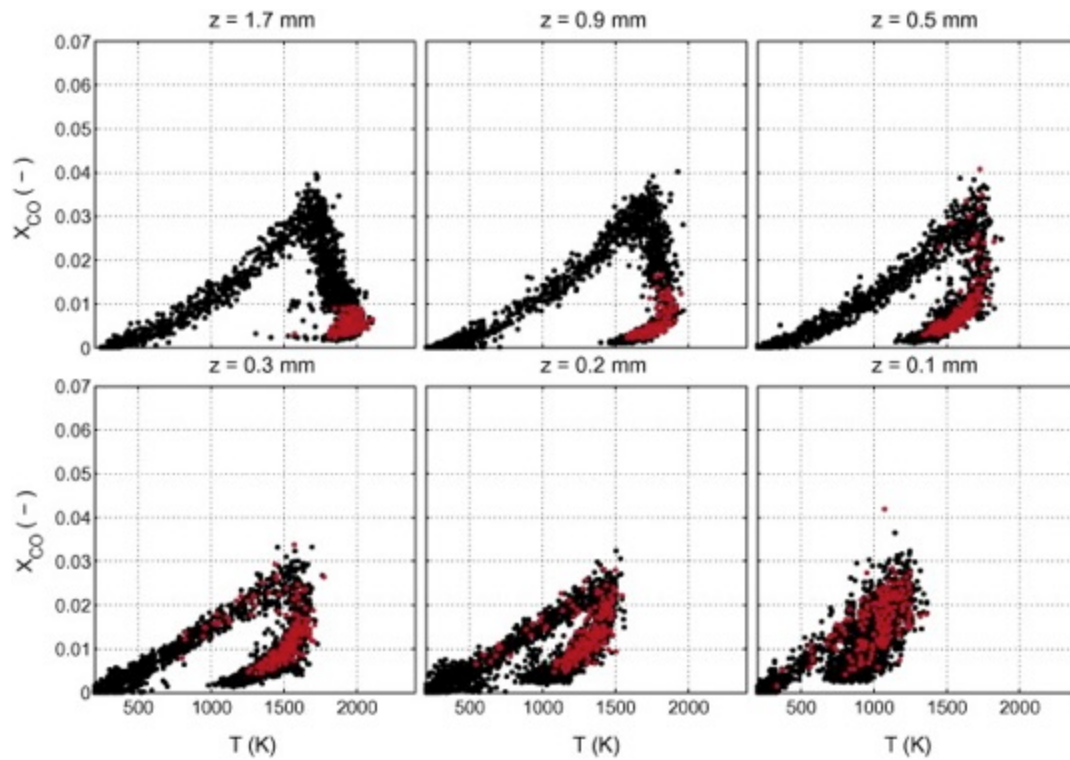
Figure 1-13 CO scatter plots for flame and at quenching for different distances from the solid surface. The instant of quenching is denoted by red data points. [13]



(a) $T_w < 500$ K

(b) $T_w \approx 1273$ K
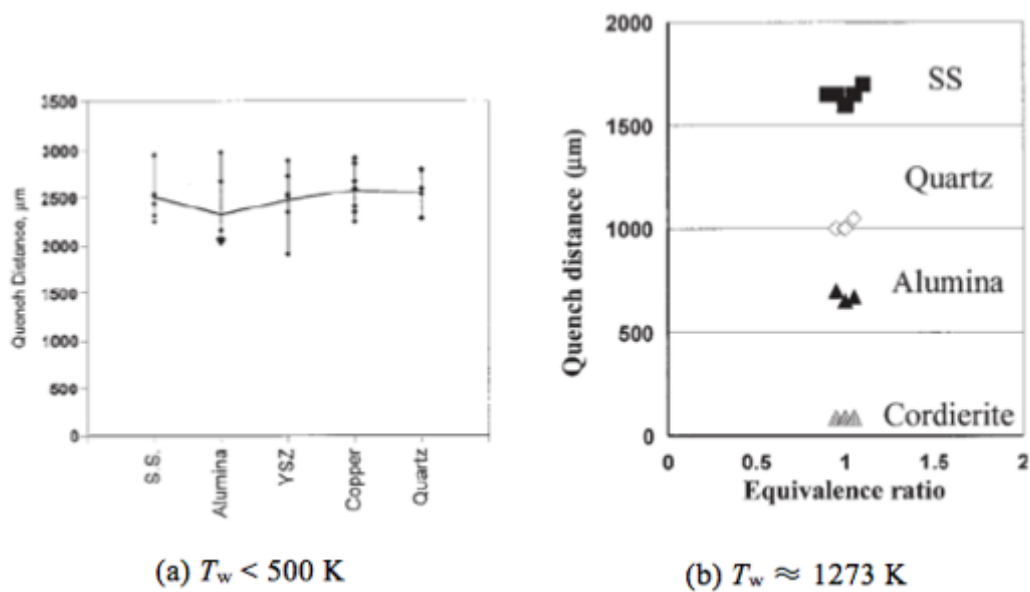
Figure 1-14 Quenching distance over various surface materials [14].

16
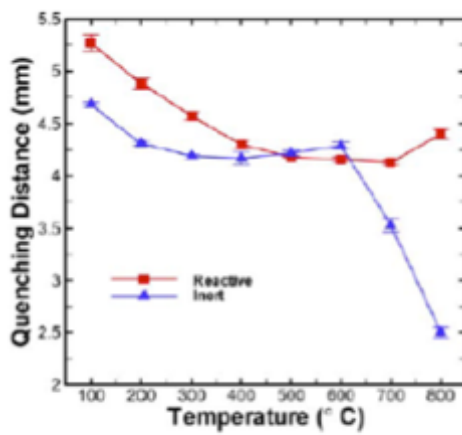
(a) Reactive and inert SUS304          (b) Reactive and inert Al₂O₃
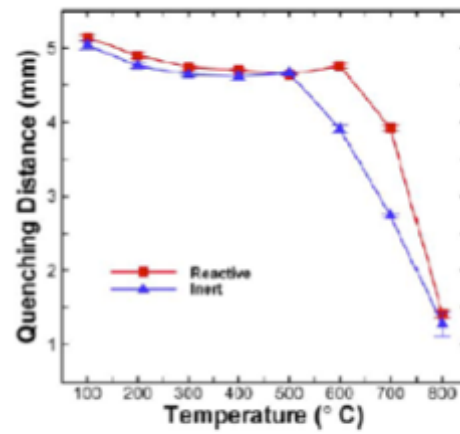
Figure 1-15 Quenching distance for SUS304 and alumina under different wall temperatures [15].
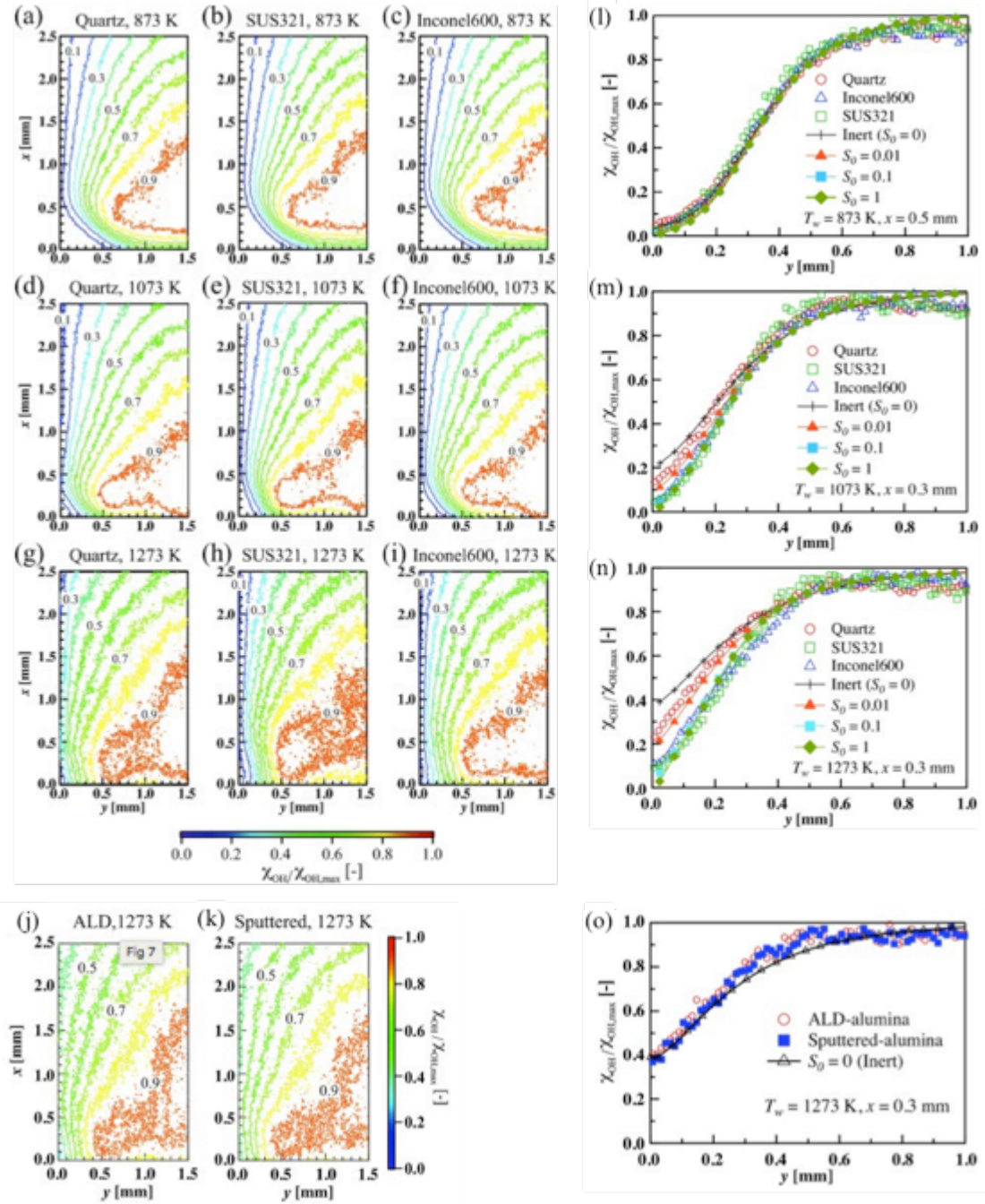
Figure 1-16 OH distributions in the vicinity to the different wall materials under various wall temperate. The simulated OH profiles with different $S_0$ are also plotted. [16][17]
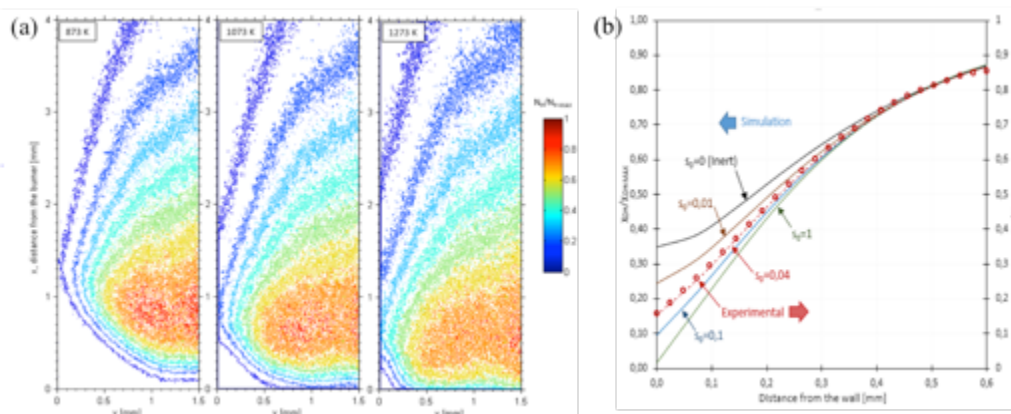
Figure 1-17 OH distribution over SiC surface. The simulated OH profiles with different $S_0$ are also plotted. [18]
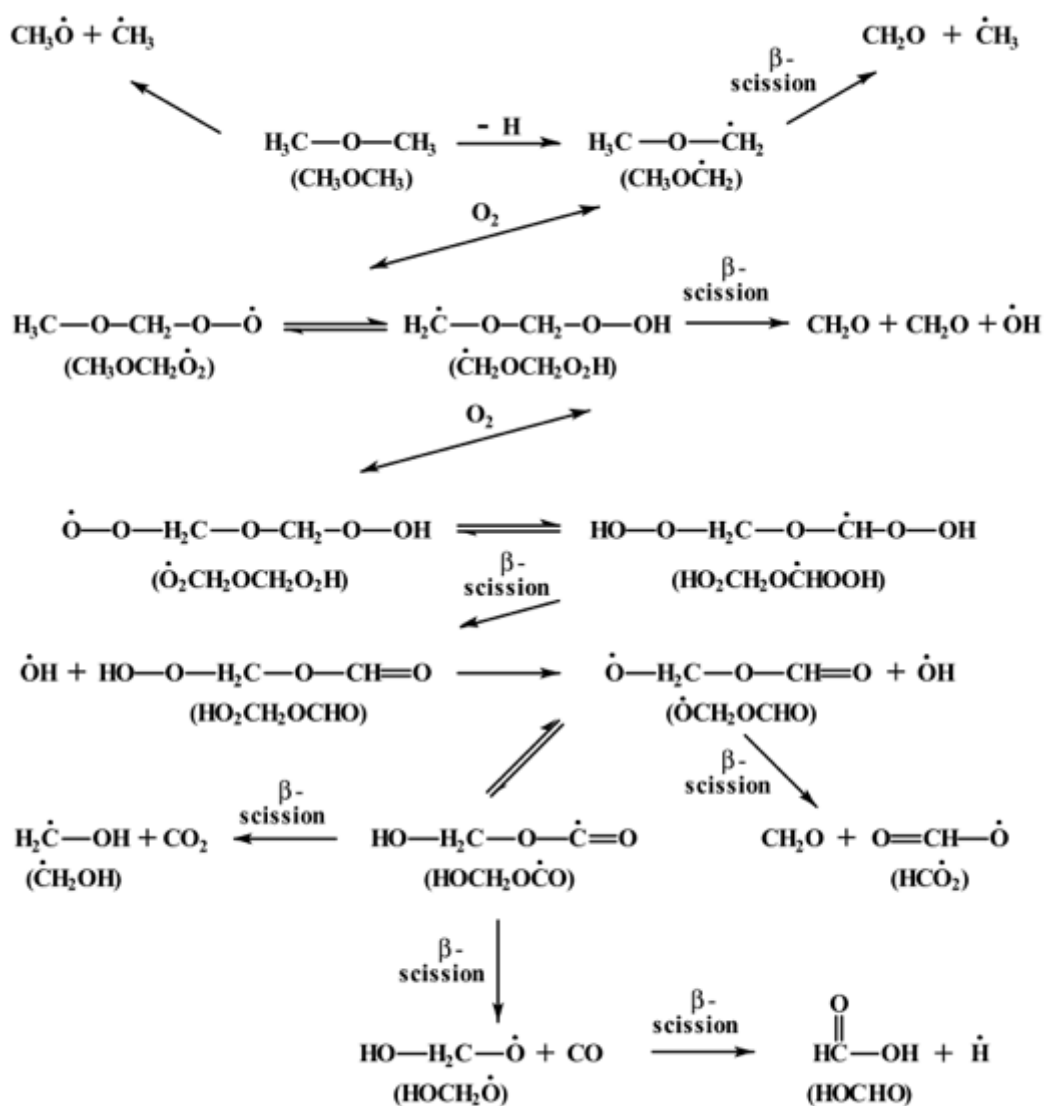


Figure 1-18 Overall reaction scheme of dimethyl ether oxidation [21][22].
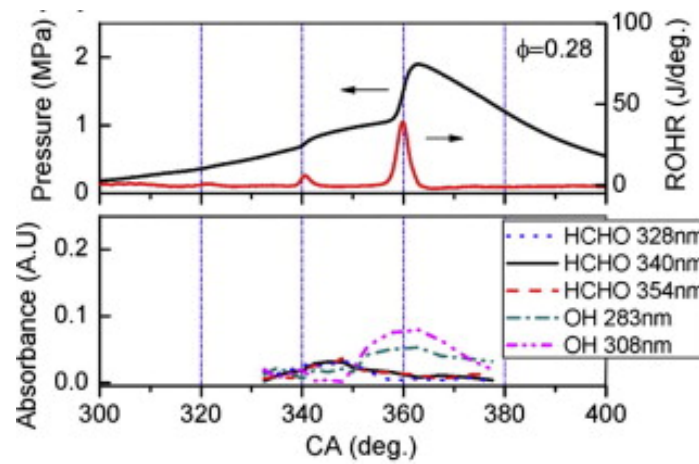
Figure 1-19 Simulated pressure and heat release rate with the measured time-resolved
HCHO and OH distributions in an DME-HCCI engine [25].
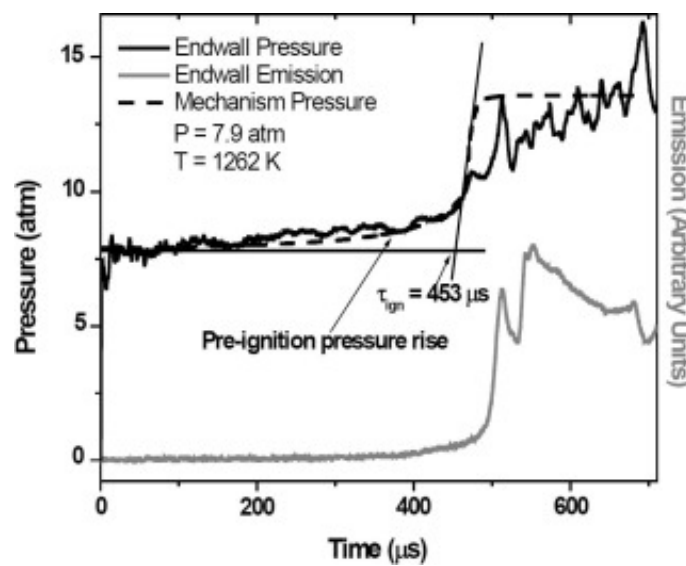


Figure 1-20 Typical endwall pressure and CH emission traces used to determine
ignition delay time for a shock tube study [26].
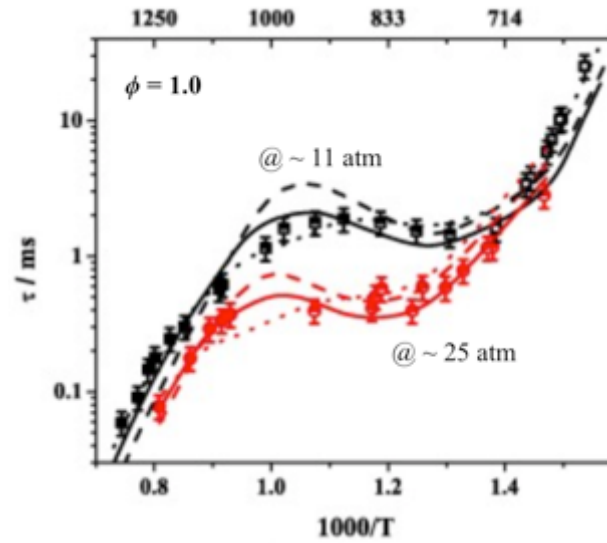
Figure 1-21 Comparison of the measured ignition delays and the simulated results with different mechanisms [26]. Solid line – CH4/DME 2014 [26]; dashed line – Zhao et al. [27]; dotted line – DME 2000 [21][22].
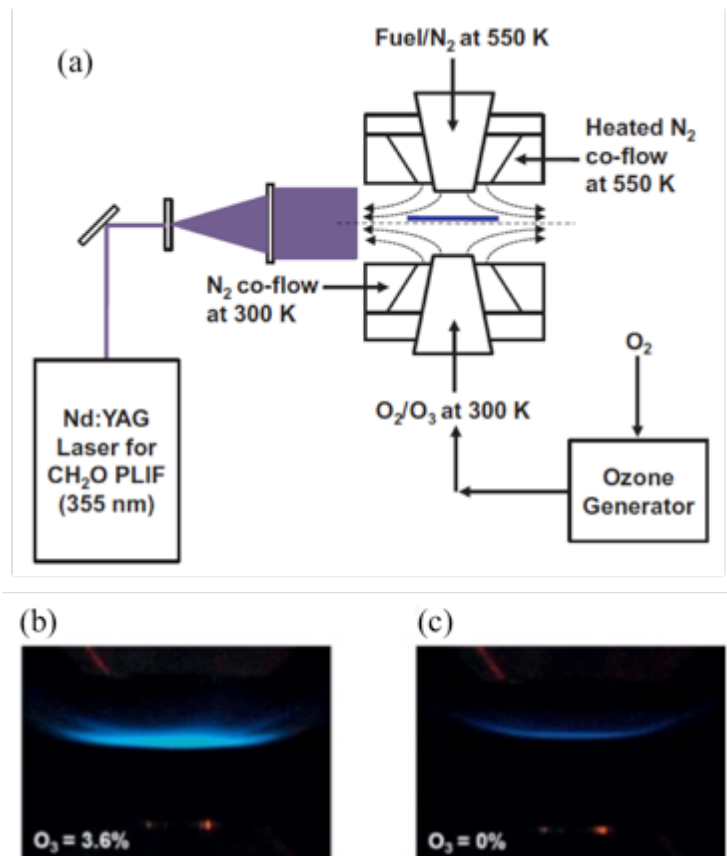


Figure 1-22 (a) Schematic of ozone stabilized cool flame. (b) Cool diffusion flame with ozone. (c) Cool diffusion flame without ozone. [29]
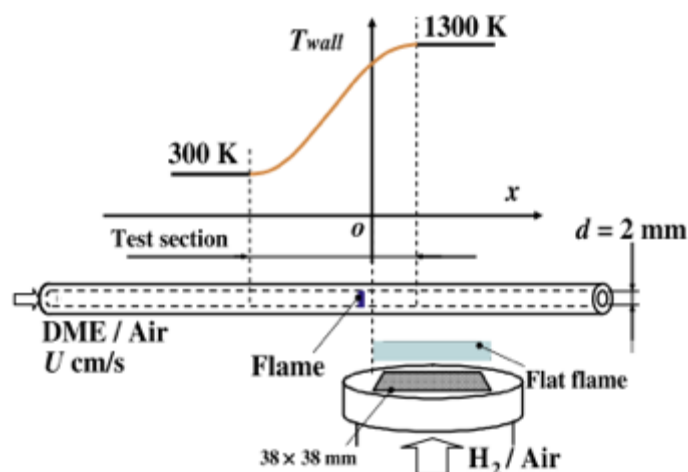
Figure 1-23 Schematic of the micro flow reactor with a prescribed temperature profile
[31].
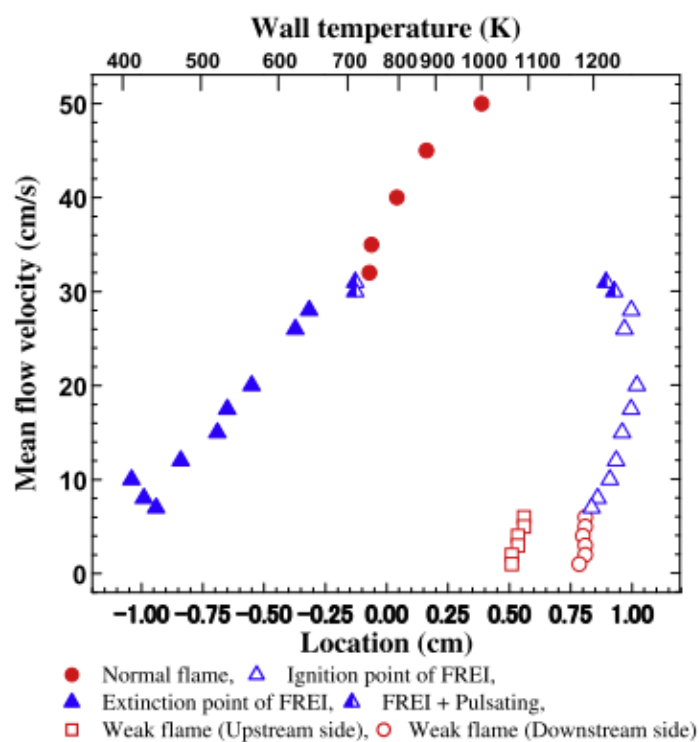


Figure 1-24 Experimental flame responses as a function of a mixture flow velocity at
the tube inlet for a stoichiometric DME/air mixture [31].

# Chapter 2 Micro Flow Reactor for Wall Chemical Effect Study

Flame chromatography is proposed by Maruta et al. [33] for the investigation of gas-phase reactions. By flowing the fuel/air mixture at the flow velocity lower than 4 cm/s into a 2 mm-in-diameter quartz tube, a weak flame with multiple reaction zones can be obtained when the temperature gradient is imposed in the streamwise direction. The weak flame is an ideal tool for the study of ignition process, because it is a stable flame with spatially separated low- and high-temperature oxidation zones.

However, with the circular tube, PLIF measurement near the wall surface is difficult. In addition, it is impossible to make deposition of different materials onto the inner wall surface. Therefore, in the present study, a detachable micro flow channel with a rectangular cross section is developed, and the flame behavior in this rectangular channel is compared with that in previous studies.

## 2. 1. Micro Flow Reactor

### 2. 1. 1. Micro Channel with a Streamwise Temperature Gradient

Figure **2-1** shows the quartz micro flow reactor developed in this study. The flow reactor has a 100-mm-long rectangular channel with a cross-section of 1.5 mm × 5 mm, while the outside dimensions are 130 mm in length and 10.5 mm × 30 mm for the cross-section after assembling. This quartz micro flow reactor made with synthetic silica has a very high transmission both for the ultraviolet range used in OH chemilluminescence and OH PLIF and for the visible light used in HCHO PLIF. Two black quartz (Nb-doped) layers are fusion-bonded to the top and bottom plates at the downstream part for the absorption of infra-red (IR) light from the IR lamp heater (GA298, Thermo Riko). Due to the heat conduction along the quartz channel and the radiation heat loss to the ambient, a wall temperature profile with a streamwise gradient is formed in the channel.

The geometry of this micro flow reactor is designed based on a 1-D energy balance model [34] as show in Eq. (2-1);

$$\lambda\left(a_1 b_1 - a_2 b_2\right)\frac{\partial^2 \theta}{\partial x^2} + 2\varepsilon\sigma\left(a_1 + b_1\right)\left(\theta^4 - T_{amb}^4\right) + 2h_{wo}\left(a_1 + b_1\right)\left(\theta - T_{amb}\right) + 2h_{wi}\left(a_2 + b_2\right)\left(\theta - T_{gas}\right) = 0$$

(2-1)

where $a_1$ and $b_1$ are the outside thickness and the width of the micro flow reactor; $a_2$ and $b_2$ are the inside thickness and the width of the channel; $\lambda$ is the thermal conductivity, $\varepsilon$ is the emissivity; $\sigma$ is the Stefan-Boltzmann constant ($5.670373 \times 10^{-8}$ Wm$^{-2}$K$^{-4}$); $h_{wo}$ and $h_{wi}$ are the heat transfer coefficient between flow reactor and ambient, flow reactor and the inside gas flow, respectively; $T_{amb}$ and $T_{gas}$ are the ambient temperature (300 K) and the temperature of inside gas flow, respectively; $\theta$ is the temperature of the flow reactor. In Equation (2-1), the four terms on the LHS stand for the heat conduction, radiation and heat transfer between the reactor and the ambient, the reactor and the inside gas flow, respectively. Figure **2-2** illustrated the calculated temperature profile with different outside thickness. With a larger outside dimensions, a milder temperature gradient will be formed in the streamwise direction, which is suitable for forming separated reaction zones. However, limited by the lamp heater power, the required wall temperature for the hot flame ignition may not be achieved for a thick channel. As such, an outside thickness of 10.5 mm and a width of 30 mm are chosen. The calculated temperature gradient at $T_w$ = 1100 K is ~ 400 K/cm, which is similar with Maruta et al.'s reactor with a circular tube [33].

Figure **2-3** [35] shows the schematic and photo of the heating system. An infrared lamp is used as the heat source, which is mainly for generating the near-infrared light. A long quartz circular rod is used to guide the collected near-infrared light. To introduce the near-infrared light from the lamp to the rod, gold spheroid mirrors are set in between. The lamp and the rod are placed at the two focus points of the mirrors respectively. Collected near-infrared rays travel straight through the rod, while the other rays reflected repeatedly over the internal surface of the rod until they reach the other end. As a result, low energy loss is possible during the light transportation from the lamp to the heat output. The maximum IR lamp power for the heater is 2 kW, which can give a maximum heating temperature of 1500 K within a 20 mm-diameter circular area on the sample. Both water- and air-cooling are installed for the IR heaters. The cooling water is driven by the magnet pump, with a flow rate over 2 L/min for each heater.

# Micro Flow Reactor for Wall Chemical Effect Study

A 0.5 mm diameter hole is opened parallel to the halfway line of the black quartz at the position 3 mm away from the channel's inner surface for both top and bottom wall. Two R-type thermocouples with a 0.3 mm diameter, which is connected to a data acquisition/switch unit (Agilent, 34970A), can be inserted into holes to monitor the temperature. The power of the IR lamp is manually adjusted to reach an identical prescribed wall temperature distribution between the two sidewalls and among all the measurements as well.

The flow rates of fuel and air are regulated via the mass flow controllers, so as the equivalence ratio.

## 2. 1. 2. Bubbling System

A bubbling system shown in Figure **2-5** is adopted to introduce *n*-heptane for *n*-heptane/air flame and to supply the reference gas for the laser intensity calibration of OH/HCHO PLIF measurements. Carrier gas with a constant flow rate is introduced into the liquid in a stainless bottle, of which temperature is kept constant with a mantle heater, and is mixed with a certain amount of the vapor at its saturated vapor pressure . The ribbon heater over the tubing is to prevent the condensation. The vapor concentration can be further adjusted by a secondary carrier gas flow.

Equation given by Willingham et al. [36], i.e.,

$$\log_{10} P_{hpt} = 6.90342 - \frac{1268.636}{T + 216.951} , \tag{2-2}$$

where $P_{hpt}$ is the partial pressure of *n*-heptane (in mmHg), and $T$ is the temperature (in °C), is used to calculated the partial pressure of *n*-heptane. As showing in Figure **2-6**, the partial pressure of *n*-heptane is 7782.62 Pa at 30 °C, corresponding to the mole fraction of *n*-heptane is 0.0768 at the atmospheric pressure. The equivalence ratio $\phi$ is varied by changing the flow rate of the additional air.

Acetone/air mixture is used as the reference flow for calibrating the OH-PLIF measurement. Acetone is stored in the bottle, while air is used as a carrier gas. The saturated acetone vapor pressure can be given as [37]

$$\log_{10} P_{actone} = 7.125267 - \frac{1214.208}{T + 230.002} , \tag{2-3}$$

where $P_{acetone}$ is the partial pressure of acetone (in mmHg), and $T$ is the temperature (in °C). The profile is shown in Figure **2-7**.

A reference flow for HCHO-PLIF can be obtained by using nitrogen flowing through formalin solution. The liquid-vapor equilibrium of HCHO solutions in water can be expressed as [38]

$$P_{HCHO}(X_{HCHO}, T) = (\frac{1.667}{X_{HCHO}} - 0.667)^{-0.905} 2.325 \times 10^{13} \exp\left(-\frac{60.3 \times 10^3}{RT}\right), \qquad (2\text{-}4)$$

where $P_{HCHO}$ is the partial pressure of HCHO expressed in Pa, $X_{HCHO}$ is the mass fraction of HCHO in liquid solution, $R$ is the gas constant, and $T$ is the temperature in K. The profile of the HCHO vapor pressure from formalin (40% HCHO in water) is shown in Figure **2-8**.

### 2. 1. 3. Setup for Flame Chemiluminescence Imaging

A high-speed ICCD camera (FASTCAM, Photron) equipped with a f = 105 mm 1:4.5 UV Nikkor lens is used to capture the OH chemiluminescence (Figure **2-9**). It can capture up to 2000 frames per seconds, so that a time-resolved flame behavior can be observed. OH chemiluminescence images are taken with an optical band-pass filter of 307 nm CWL, 10 nm FWHM, by which the ambient light is filtered out.

## 2. 2. Laser-induced Fluorescence System

The overall experimental setup for the PLIF measurement of the weak flame is shown in Figure **2-10**. The laser beam is separated to two optical paths: one for monitoring the incident laser power, the other is transferred to a thin laser sheet and introduced to the flame. Specific species in the flame is exited according to the laser wavelength, and emits fluorescent that can be captured with the ICCD camera or the spectrometer. The synchronization between the laser and the camera is ensured with a programmable logic/timing controller (LC880, LabSmith). The connection is shown in Figure **2-11**.

### 2. 2. 1. Principle of LIF

Laser-induced fluorescence (LIF) is a non-intrusive flow diagnostic tool that can measure gas-dynamic properties, such as velocity, temperature, pressure, species concentration. With optical units, laser sheet can be formed to acquire planar snapshots of flow, and realize flow visualization with 2D images.

**Micro Flow Reactor for Wall Chemical Effect Study**

As shown in Figure **2-12**, laser induced fluorescence takes place via a multi-step process. The ground state atom or molecule is pumped to the excitation state by the laser with the certain wavelength. Since it is not stable in the excitation state, the atom or molecule returns to a lower energy state, companying with a variety of energy transfer process. A part of the excess energy is released as fluorescence with longer wavelength.

The LIF yield in the linear regime [40][41] is written as

$$F = C_{exp} B_{12} I_v N f_1 \frac{A_{21}}{A_{21} + Q_{21}} , \qquad (2-5)$$

where $C_{exp}$ is an experimental constant dependent on various condition including the optical setup, $B_{12}$ is the adsorption coefficient, $N$ is the total number density of the species, $I_v$ is the incident laser energy, $f_1$ is the population fraction of the "ground state" for the particular excitation, $A_{21}$ is the spontaneous emission coefficient, and $Q_{21}$ is the collisional quenching rate.


### 2. 2. 2. OH- and Acetone-PLIF

A Nd-YAG laser-pumped pulsed dye laser (SCANmate2C, Lambda Physik) is employed in the PLIF system. For OH and acetone excitation, the pumping laser from the 2nd harmonic generator is used with Rhodamine 6G dye at a concentration of 0.1 g/L for oscillator and 0.03 g/L for pre-amplifier. The laser wavelength is calibrated with a wavelength meter (WS5/3245 wavelength meter, HighFinesse/Ångstrom) as shown in Figure **2-13**. Wavelength is chosen as 283.553 nm, and its energy is 8 mJ/pulse. The laser from the output goes to a beam splitter. 2% of the split laser beam further drops its energy to less than 300 µJ by two neutral-density filters for monitoring the pulse energy. A focusing lens is used to introduce the laser beam to an optical fiber, which guides the laser to the detector. Note that the fiber may be damaged with an input energy exceed 300 µJ when measuring ns-laser pulses and respectively less with even shorter pulses.

With an excitation wavelength of 283.553 nm, OH fluorescence (~308 nm) at the $Q_1(8)$ spectral line of the A2$\sum\Leftarrow$X2$\prod$(1,0) transition is emitted [42]. This OH fluorescence intensity is proportional to the OH mole fraction within 10% at the temperature from 1000 K to 2000 K [16].

Acetone vapor absorbs UV light over a broad band of wavelength from 225 to 320 nm, and has a continuous emission spectrum from 350 to 550 nm with its peak at 445 and 480 nm. Its fluorescence is independent of temperature and local gas composition [37].

### 2. 2. 3. HCHO-PLIF

The $A^2A_1$-$X^1A_1$ $4_0^1$ pQ ($J'' = 15$, $K'' = 5$) transition of HCHO is excited with 355 nm wavelength [43][44], which is generated directly from the 3rd harmonic generator of the Nd:YAG laser. Since 355 nm is not the optimized wavelength for HCHO excitation, a laser energy up to 60 mJ/pulse is used.

Since $A_{21} \ll Q_{21}$ for HCHO, Equation 2-5 for the fluorescence yield can be simplified as

$$F = C_{exp} B_{12} N_{HCHO} I_v f_1 \frac{A_{21}}{Q_{21}} \tag{2-6}$$

For a given HCHO concentration, the temperature dependency mainly comes from the population fraction of the "ground state" for the particular excitation, $f_1$, and the collisional quenching rate, $Q_{21}$. Kyritsis et al. [45] gave $f_1$ as a function of temperature $T$, written as

$$f_1 = (1 - e^{-1680.5/T}) \frac{40.1969 e^{-740/T}}{(1 + 0.134/T + 0.037/T^2)T^{3/2}} \tag{2-7}$$

with $T$ in K. The quenching rate $Q_{21}$, is given by [45]

$$Q_{21} = \sum_i N_i \sigma_i v_i \tag{2-8}$$

where $N_i$ is the number density of the collision partner, species $i$, scaling as $T^{-1}$; $\sigma_i$ is the collision cross-section; and $v_i$ is the relative velocity of the collision partner and excited species, scaling as $T^{0.5}$. The scaling for $\sigma_i$ has two limits of $T^{-0.5}$ and $T^0$. Thus, the scaling for $Q_{21}$ varies between $T^{-1}$ and $T^{-0.5}$. Figure **2-14** shows the temperature dependence assuming that $\sigma_i$ is proportional to $T^{-0.25}$.

### 2. 2. 4. HCHO Fluorescence Dependence

The HCHO fluorescence dependence on laser energy and HCHO concentration is examined. Figure **2-15** shows the HCHO-LIF intensity for a HCHO/$H_2O$/$N_2$ mixture

versus the laser energy. HCHO concentration is kept constant at 6730 ppm with the formalin bubbling system. The concentration is estimated based on the saturated vapor pressure at 41 ºC. Concentration drift up to 8 % is expected due to the temperature fluctuation.  A good linearity between the HCHO-LIF intensity and the laser energy is confirmed. Figure **2-16** shows the relationship between the HCHO-LIF intensity and the HCHO concentration. The laser power is kept at 40 mJ, which is the same laser power used in the following measurement. The HCHO concentration is changed from 1000 to 7500 ppm by varying the flow rate of secondary $N_2$. The result suggests a good linearrity between the HCHO-LIF intensity and the HCHO concentration at the laser power of 40 mJ.

### 2. 2. 5. Laser Sheet Optics

To realize two-dimensional measurements, a 0.3-mm-thick laser sheet is formed through the optical unit shown in Figure **2-17**. Prisms are used for changing the laser light direction, while concave lens and convex lens are employed to changing the shape of the laser. The output laser beam is first reduced to a cylindrical beam by an aperture, and then goes through a beam splitter. As explained above, 2% of the laser shots into a laser power monitor, and the rest goes to a series of cylindrical lens to form a parallel thin laser sheet. The first (concave, $f$ = -25 nm) and the second (convex, $f$ = 70 mm) lens are stretching the laser beam to a sheet with a width of ~ 15 mm; while the third lens (convex, $f$ = 400 mm) is for focus the laser onto the observation region with a fine thickness.

### 2. 2. 6. LIF Imaging System

An image-intensified CCD camera (iStar, ANDOR) with a band-pass filter is used to capture fluorescence. Theoretically, the camera is able to capture even a single photon with the structure shown in Figure **2-18** [46]. Once the photon gets into the input window, it will be transferred to electron. If the photocathode voltage is + 50 V, the electron will be stopped before it reaches the multiple channel plate (MPC). But once a negative pulse is sent by the image intensifier, the photocathode voltage will drop to − 200 V, and the electron will be accelerated and reach the MPC. High voltage up to 900 V can be applied for electron to gain its energy. This voltage can be controlled by varying the gain value on the image intensifier control. The accelerated

electron finally hits the phosphor layer in front of the fiber optics, and is transferred back to photon, which can be captured by the CCD chip and converted into digital data.

An f=105 mm UV Macro lens with a bellows for adjusting the magnification is attached in front of the ICCD camera. The minimum spatial resolution can reach 7 μm × 7 μm. According to the wavelength of fluorescence, band-pass filters 307/10 nm, 447/60 nm, and 430/40 nm are employed for OH, acetone and HCHO, respectively.

### 2. 2. 7. Emission Spectra of HCHO in Weak Flame

It has been reported that species as Polycyclic aromatic hydrocarbons (PAH) could be the interference for HCHO-PLIF [47][48][49]. An optical spectrometer (iHR320, Horiba) is adopted to verify that the HCHO fluorescence is not interfered from other species. The scheme of the spectrometer is shown in Figure **2-19** [50]. The light gather from the mirrors is guided to the grating. As a result, light with different wavelength can be spatially separated and be detected. By comparing the measured spectrum from the weak flame is compared with the one from a HCHO/H$_2$O/N$_2$ mixture, it can be confirmed that the signal is free from interferences.

As shown in Figure **2-20**, the two spectrums coincident with each other, suggesting no PAH interference is found in the weak flame. Since lean flame is used in this study, it is reasonable that no PAH species is generated.

### 2. 2. 8. Signal Calibration

According to Equation 2-5, fluorescence intensity can be considered to be proportional to the number density of the species and the incident laser energy. If the spatial laser energy distribution change for a laser sheet among each shot is neglected after average, the local fluorescence intensity is expressed as

$$F_{loc} = a \cdot f_{loc} I_{beam} \cdot N_{loc},$$ (2-9)

where

$a = C_{exp} B_{12} f_1 \dfrac{A_{21}}{A_{21} + Q_{21}}$ is a constant for a certain species when the temperature, pressure

and mixture component are the same. $f_{loc}$ is a fraction of the local laser intensity over the laser beam energy, $I_{beam}$ is the incident laser energy of the beam, and $N_{loc}$ is the

local number density of the species. If comparing a measurement of a species with an unknown concentration and a referent flow with a fixed concentration, it gives

$$N_{loc} = \frac{a_{ref}}{a} \frac{I_{beam,ref}}{I_{beam}} \frac{F_{loc}}{F_{loc,ref}} N_{loc,ref} \qquad (2\text{-}10)$$

OH-PLIF is calibrated with acetone-PLIF with a given acetone concentration, i.e.,

$$N_{loc,OH} \propto \frac{I_{beam,acetone}}{I_{beam}} \frac{F_{loc}}{F_{loc,acetone}} \qquad (2\text{-}11)$$

Based on the monitored laser beam energy and the fluorescence intensity from both OH in the flame and acetone in the reference gas, the OH concentration can be compared among all measurements. Since HCHO-PLIF in flame is calibrated from the formalin/N$_2$ reference flow, $a_{ref}$ is equal to $a$ in Equation 2-9. Thus, the absolute concentration of HCHO can be calculated.

## 2. 3. Flame Response to Flow Velocity

### 2. 3. 1. Wall Temperature Distribution in the Rectangular Channel

The wall temperature is measured with two types of thermocouple: a high-temperature K-type sheathed thermocouple with a diameter of 0.5 mm; and the R-type bare thermocouple with a wire diameter of 0.05 mm and a joint diameter of 0.2 mm. The thermocouple is fixed onto a Z-stage, and moving along the centerline of wall surface to measure the wall temperature point by point. In the meanwhile, the camera takes the position of the thermocouple. As such, the wall temperature distribution along the channel is obtained as shown in Figure **2-21**. Multiple measurements have been made for both sidewalls with two types of thermocouple to ensure the symmetric wall temperature distribution for the channel, and to check the reproducibility of the wall temperature among different measurements. As shown in Figure **2-21**, the maximum wall temperature reaches around 1200 K, with a temperature gradient approximately 380 K/cm.

An 8th degree polynomial equation

$$\begin{aligned} T(x) = &\, 249.2 + 10.073 \cdot x + 0.38242 \cdot x^2 + 0.025917 \cdot x^3 + 0.0003106 \cdot x^4 \\ &- 4.1717\text{e-}05 \cdot x^5 - 5.2075\text{e-}07 \cdot x^6 + 2.0846\text{e-}08 \cdot x^7 \end{aligned}$$

$$(2\text{-}12)$$

is used for fitting the wall temperature distribution, and employed as the wall temperature profile for the further numerical simulation, where $x$ is the streamwise position corresponding to the simulation domain.

### 2. 3. 2. *n*-heptane/air Flame Response to Mean Inlet Flow Velocity

A stoichiometry n-heptane/air flame is used to verify the flame behaviors in the rectangular channel are same as that in the circular tube. Figure **2-22** shows the flame position with different inlet mean flow velocities. Steady normal flames were observed in the high-velocity region (28-50 cm/s). FREI, flames with periodic ignition at the downstream, upstream propagation and quenching at the upstream [32], were observed in the intermediate velocity region (4-28 cm/s). The ignition and extinction positions are taken by the high-speed camera with a frequency of 2 kHz. When mean inlet flow velocity drops lower than 4 cm/s, the OH chemiluminescence is no longer captured by the high-speed ICCD camera, thus OH-PLIF is used to visulalize OH at the hot flame position of the weak flame. Note that OH concentration in the weak flame is only high enough in the hot flame zone for current OH-PLIF system to observe.

Figure **2-23** shows the flame position for different inlet flow velocities. The transition flow velocities from the normal flame to FREI and further to the weak flame are 28 cm/s and 4 cm/s, which are good agreement with 30 cm/s and 4 cm/s reported in the previous study in a circular tube [32]. The corresponding wall temperature for the normal flame positions also agree well with each other. When the mean inlet flow velocity decreased, the normal flame position shifted to a lower wall temperature region. When flame enters the FREI region, it is found that, for both flame in this study and that in the circular tube, the ignition position shifts to the upstream side with a decreasing the inlet mean flow velocity, and the extinction position curve plotted versus the inlet mean flow velocity has a C-shape. The corresponding wall temperatures for the ignition and extinction position of the FREI are 100 ~ 200 K different between the two studies. This is probably due to the differences in the channel geometry and the wall temperature distribution. Although only the hot flame of the weak flame is visualized by OH-PLIF for the *n*-heptane/air flame, it is found that the hot flame of the weak flame in the rectangular channel locates at the position with the wall temperature of 1150 - 1200 K, which is

coincident with that in previous study. The present results imply that the flame behavior in the present rectangular channel is basically the same as that in the circular tube [32].


### 2. 3. 3. Response of DME/ air Weak Flame to Flow Velocity

Since the low temperature oxidation zone cannot be captured with OH-PLIF measurements, response of the weak flame to the flow velocity is examined with both OH- and HCHO-PLIF. HCHO concentration is increased at the cool flame zone and vanished at the blue flame zone [25][51][52][53][54][55], so that it can be a good indicator for the low- and intermediate-temperature oxidation. In the present study, DME is selected as the fuel and the equivalence ratio is set as 0.85.

Figure **2-24** (a) shows the HCHO distribution in the weak flame with flow velocity varying from 1 to 3 cm/s. The HCHO profiles along the centerline are also given in Figure **2-24** (b). The HCHO peak slightly shifted downstream with increasing flow velocity, and the maximum concentration is increased by 16% when the velocity is changed from 1 to 3 cm/s. Similarly, the OH distribution and its profiles are presented in Figure **2-25**. Contrary to HCHO, the OH radical peak shifted upstream with increasing flow velocity, and the maximum concentration is doubled from 1 to 3 cm/s. The response of flame position to the flow velocity is similar as the computed result of the stoichiometry DME/air weak flame reported by H. Oshibe [31]; the cool and blue flame (indicated by HCHO in this study) are shifted downstream with increasing flow velocity, while the hot flame (indicated by OH in this study) is shifted upstream. With increasing flow velocity, the reactivity is increased due to larger amount of reactant. This is more pronounced for the hot flame than that of the cool and blue flames, because of the much higher heat release rate. Therefore, the HCHO concentration is not largely increased with the flow velocity, but a significant concentration increment is found for OH. In addition, influenced by the heat released from the hot flame, the hot flame position is moved upstream to compensate the higher gas temperature. In addition, influenced by the heat released from the hot flame, the hot flame position is moved upstream to compensate the increased gas temperature. However, the HCHO zone is located at the NTC region, where the gas-phase temperature is strict governed by the wall temperature. Therefore, no large

HCHO peak position shifting is found. But considering the longer reactant resident time with the lower flow velocity, the formation of HCHO starts earlier.

## 2. 4. Summary

A detachable rectangular quartz channel with a controlled wall temperature gradient is developed for investigation of wall chemical effect on the weak flame. OH chemiluminescence captured by the high-speed camera, OH- and HCHO-PLIF are used to examine the flame patterns of stoichiometry n-heptane/air flame in comparison with the results in the previous research [30][31][32] using the circular tube.

A normal flame is observed at the flow velocity over 28 cm/s, while it turns to FREI. when the flow velocity is between 4 to 28 cm/s. For lower velocity than 4 cm/s, stable weak flame is observed. Response of the weak flame to flow velocity is also investigated with an equivalence ratio of 0.85, which is same as that used in the following wall chemical effect investigation. It is found that the low- and intermediate-temperature oxidation zones illustrated with HCHO concentration are shifted to upstream with decreasing flow velocity, whereas OH, which is dominant radical in the high-temperature oxidation zone, has the opposite behavior. These findings in the present rectangular channel are in good agreement with the previous computed results for a stoichiometry DME/air flame [31].

# Micro Flow Reactor for Wall Chemical Effect Study
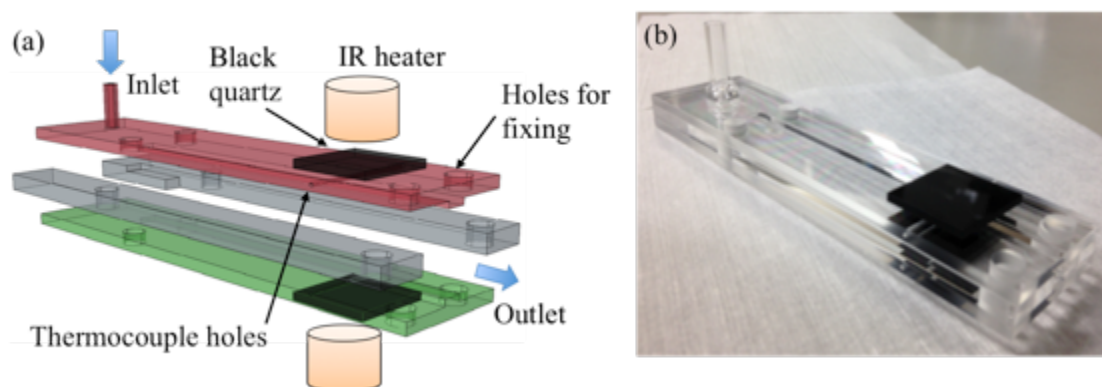


Figure 2-1 (a) The schematic diagram of the micro flow reactor. (b) Photo of the reactor.
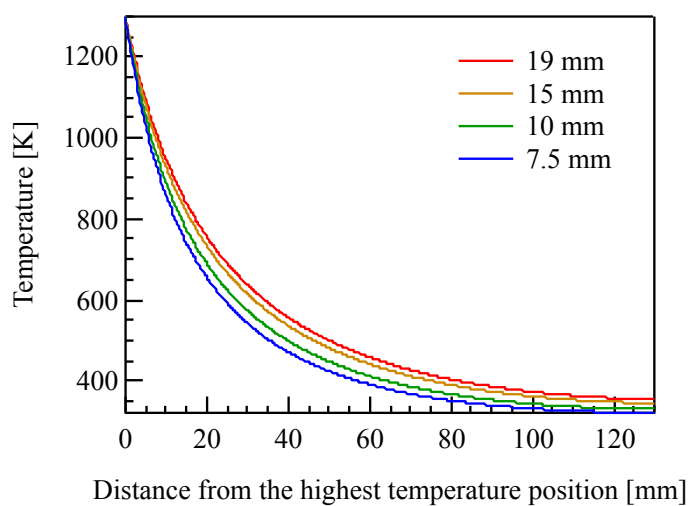


Figure 2-2 Computed temperature profiles with different outside thickness of the reactor.
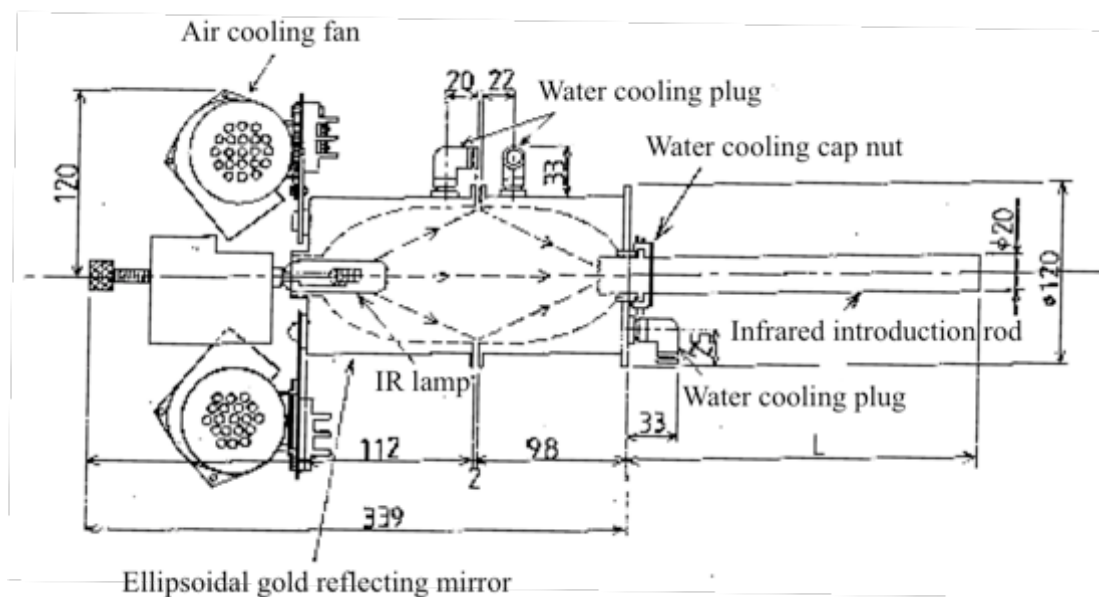
Figure 2-3 Illustration for cross section of the IR lamp heater [35].
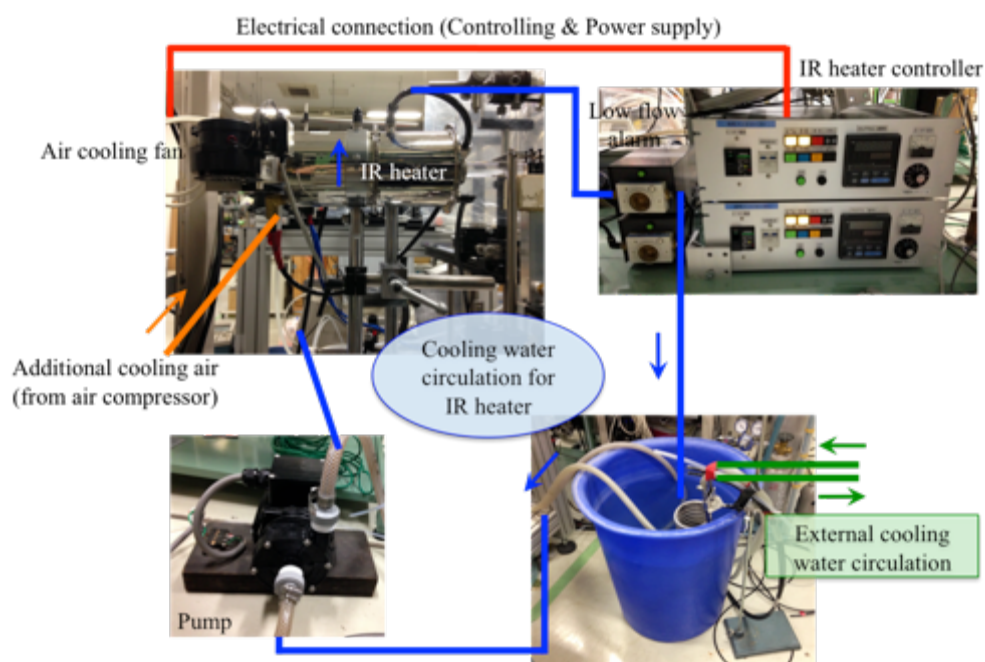


Figure 2-4 IR lamp heater and peripheral devices.
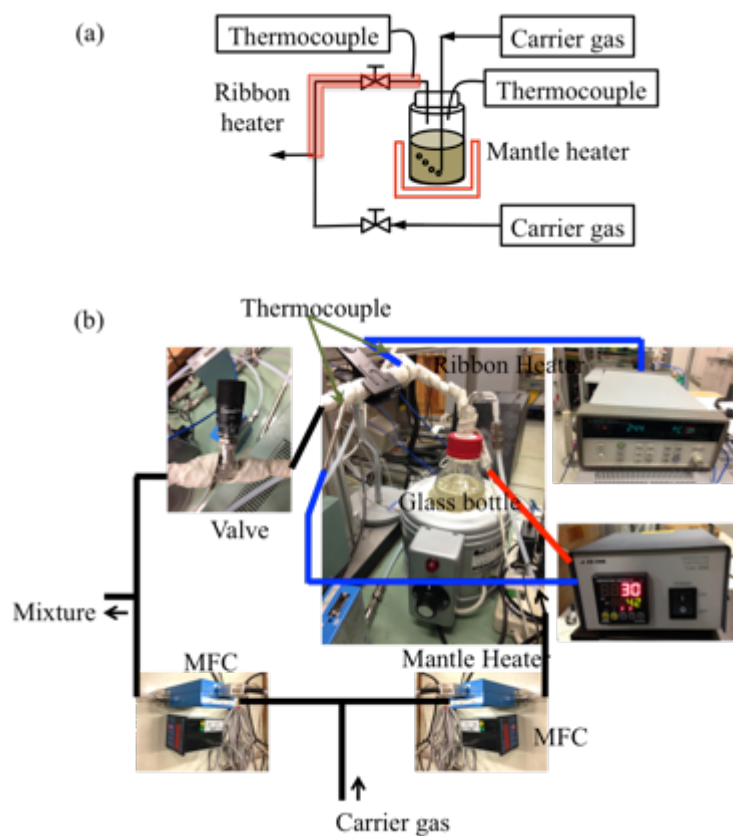
Figure 2-5 Bubbling system. (a) Schematic diagram; (b) Photo.
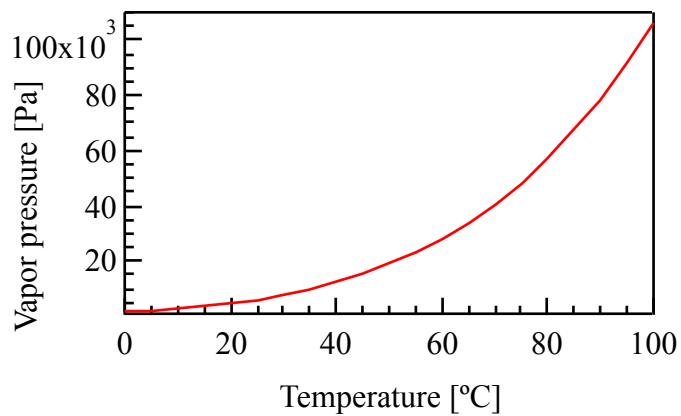


Figure 2-6 Saturated vapor pressure of *n*-heptane. Reproduced from [36].
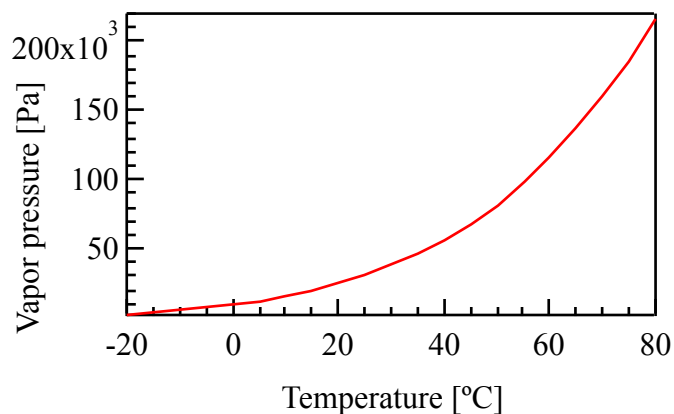
Figure 2-7 Saturated vapor pressure of acetone. Reproduced from [37].
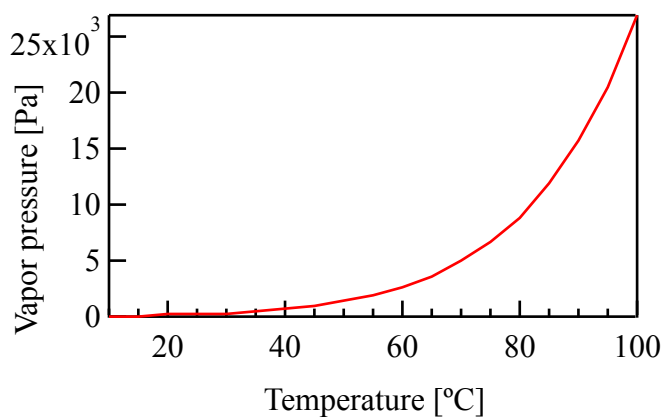


Figure 2-8 Saturated HCHO vapor pressure of formalin (40% HCHO in water). Reproduced from [38].
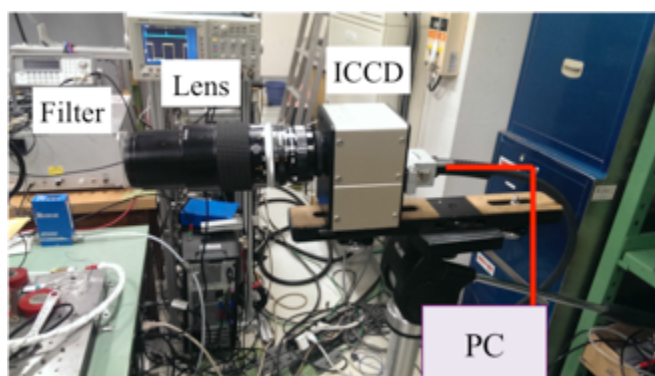


Figure 2-9 Photo of the high-speed ICCD camera.
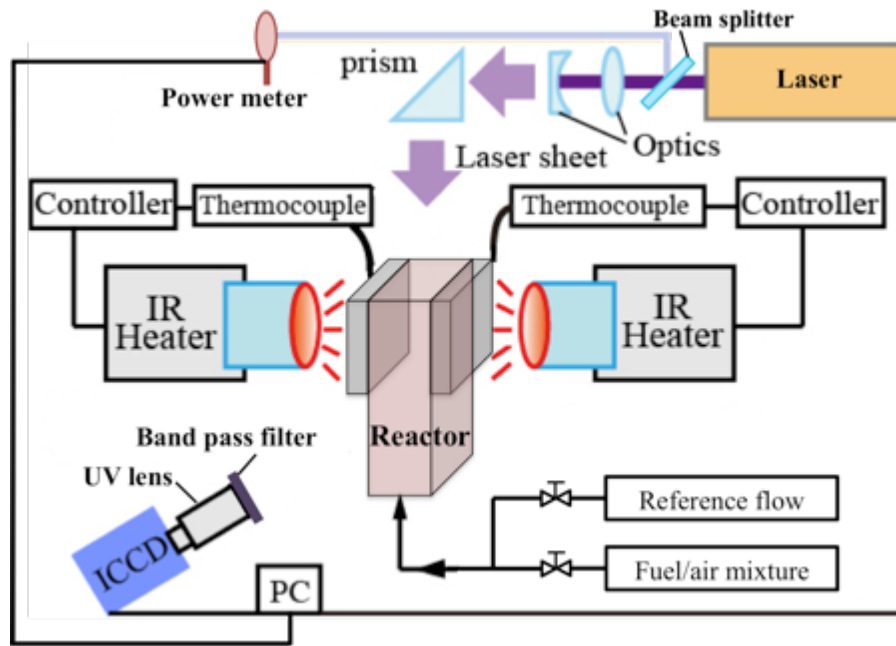
Figure 2-10 Experimental setup for PLIF measurement.
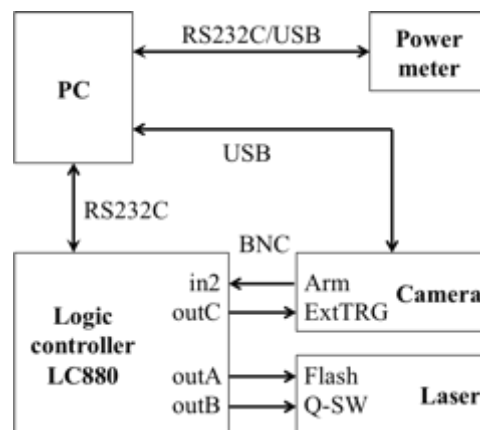


Figure 2-11 Line connection for synchronization.
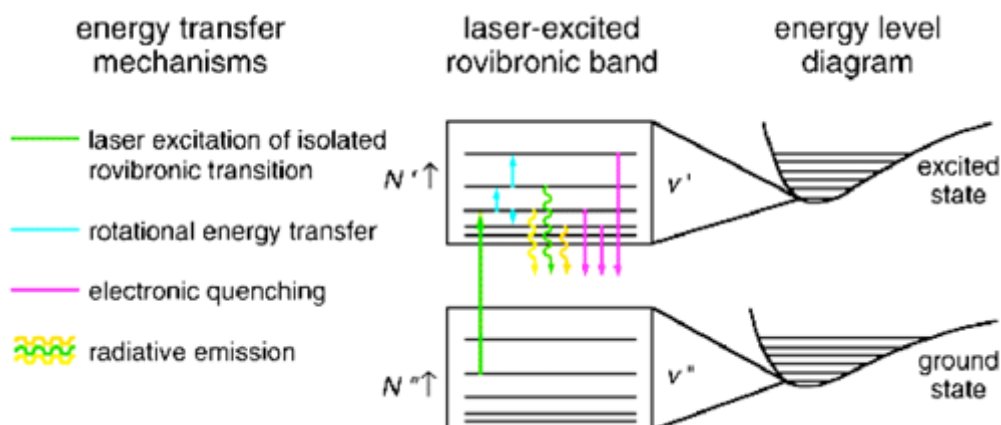
Figure 2-12 Principle of PLIF [39].
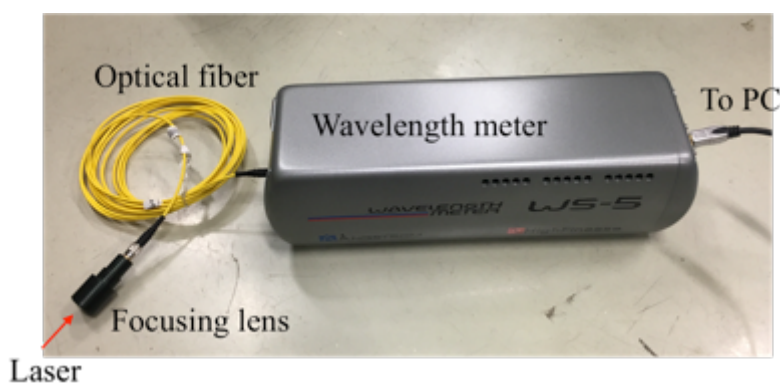


Figure 2-13 Photo of the wavelength meter.
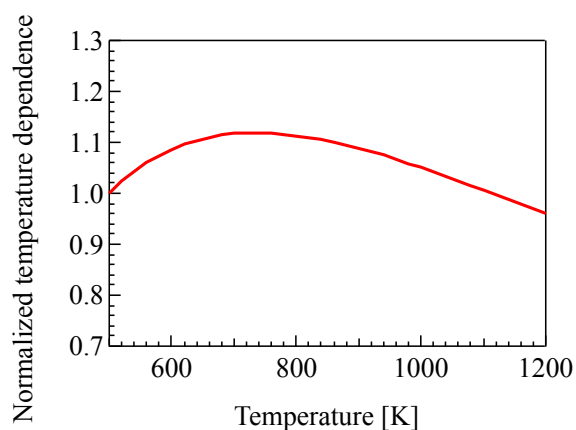


Figure 2-14 Temperature dependence of HCHO fluorescence ($\sigma_i \sim T^{-0.25}$).
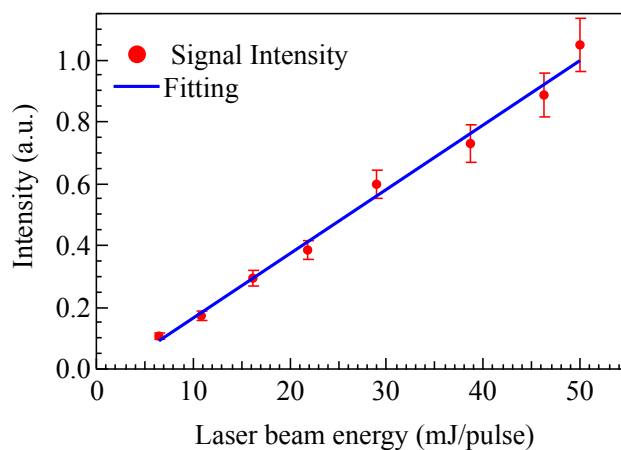
Figure 2-15 HCHO-LIF signal intensity versus laser energy for 6730 ppm HCHO concentration.
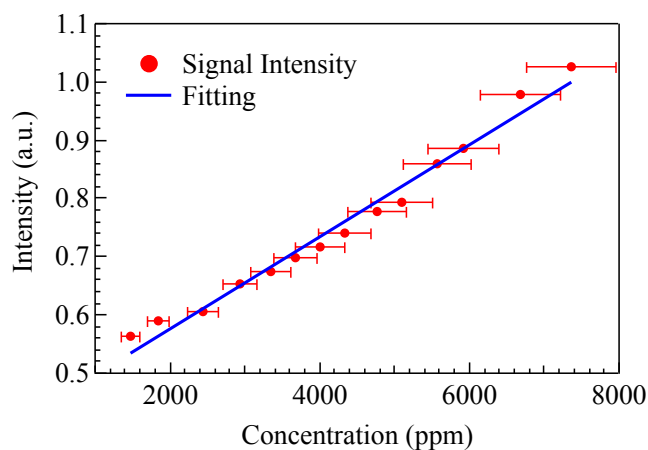


Figure 2-16 HCHO-LIF signal intensity versus HCHO concentration at 40 mJ laser energy.
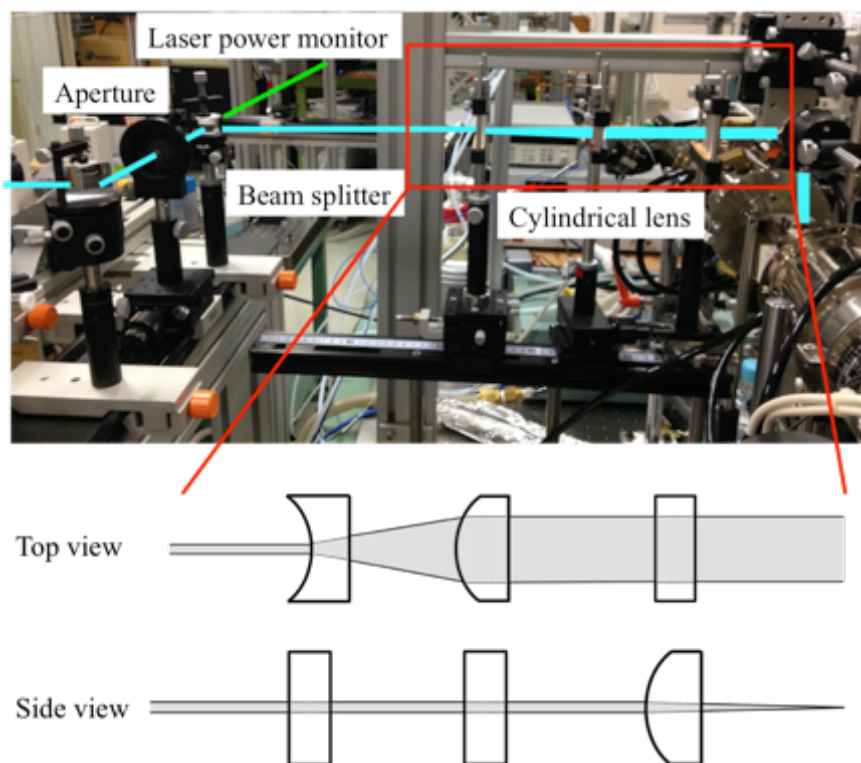
Figure 2-17 Scheme of the Optical unit.
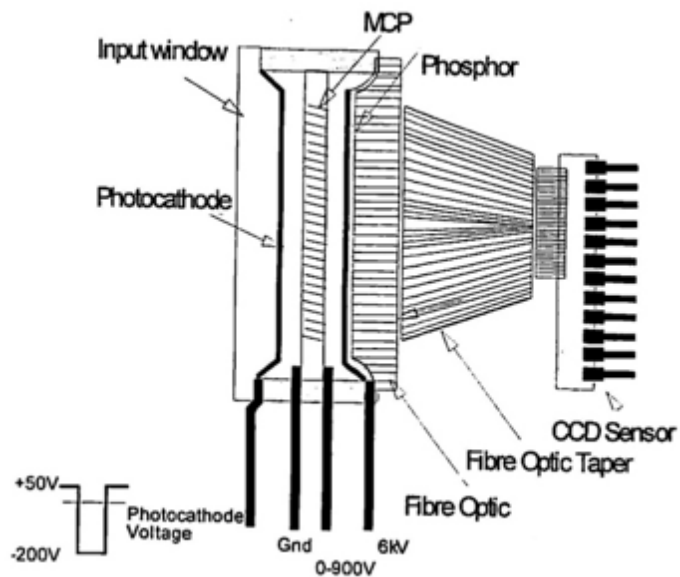


Figure 2-18 Illustration for cross section of the ICCD camera [46].
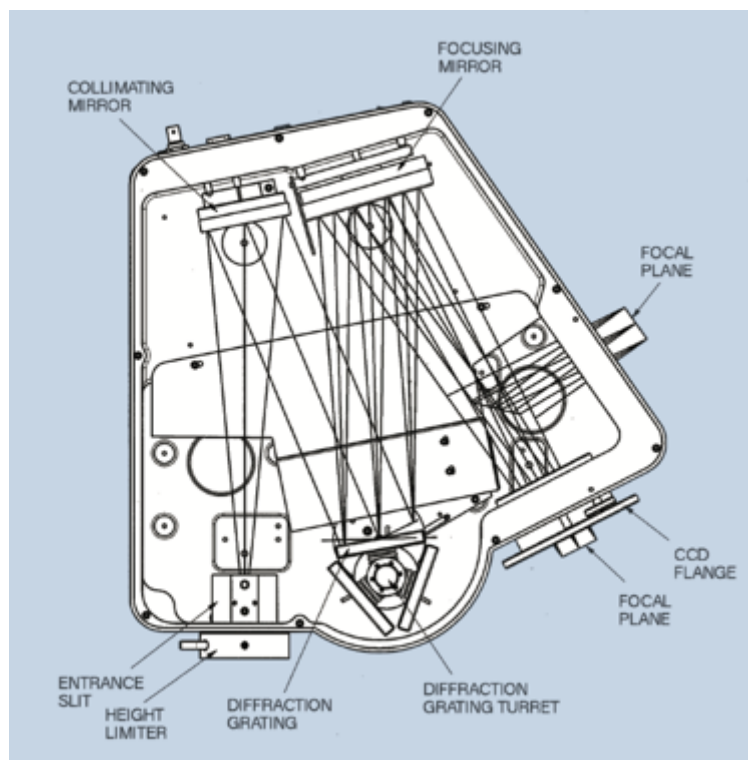
Figure 2-19 The schematic diagram of the spectrometer [50].
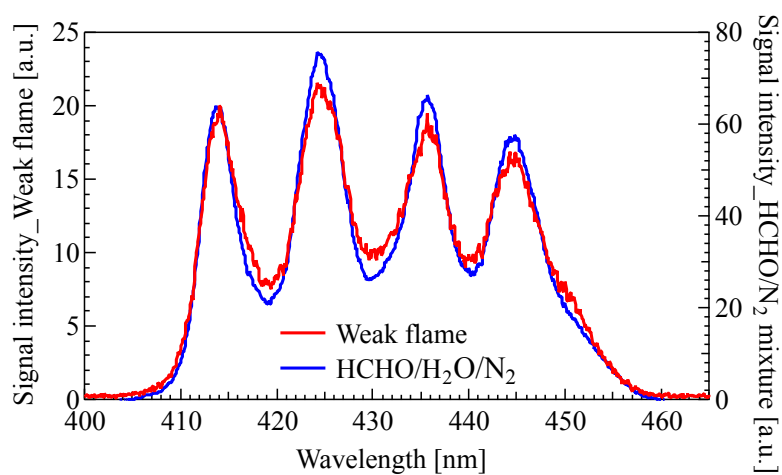


Figure 2-20 HCHO emission spectrum (430 nm band-pass filter, FWHM: 20 nm).
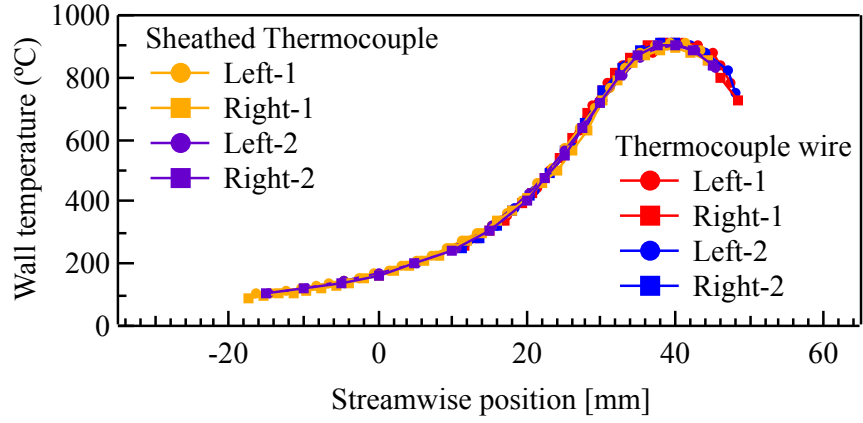
Figure 2-21 Wall temperature distribution.
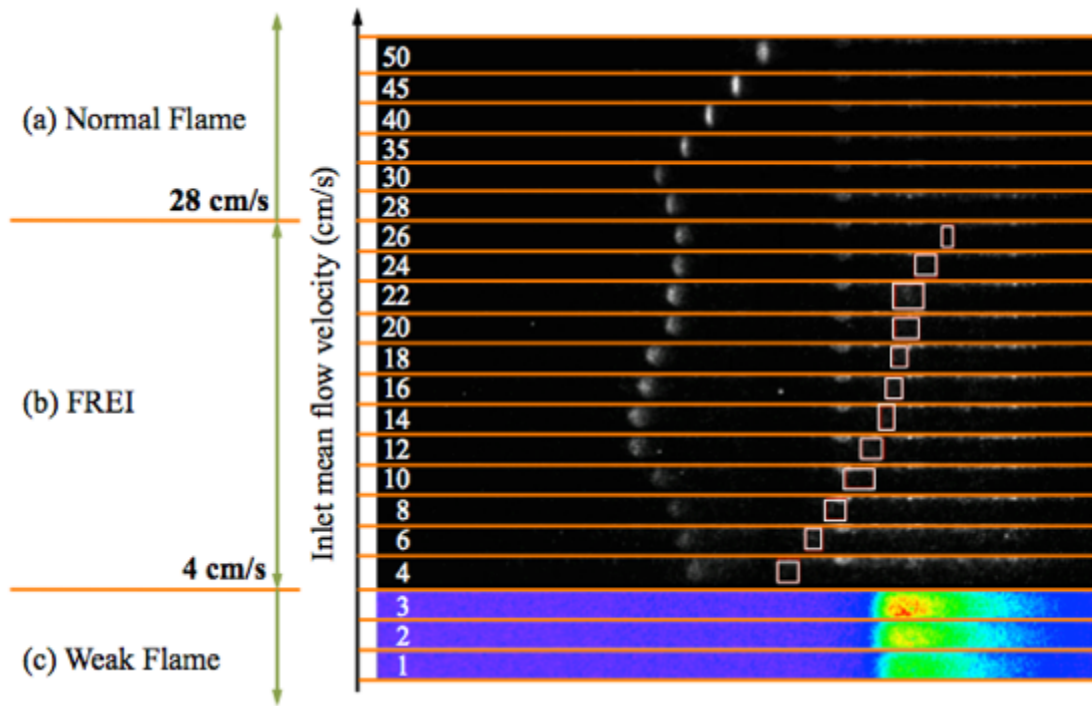


Figure 2-22 Flame (OH chemiluminescence) images in the rectangular micro flow channel under different inlet flow velocity. (a) Normal flame and (b) FREI are taken by high-speed camera, (c) weak flame is taken by OH-PLIF.
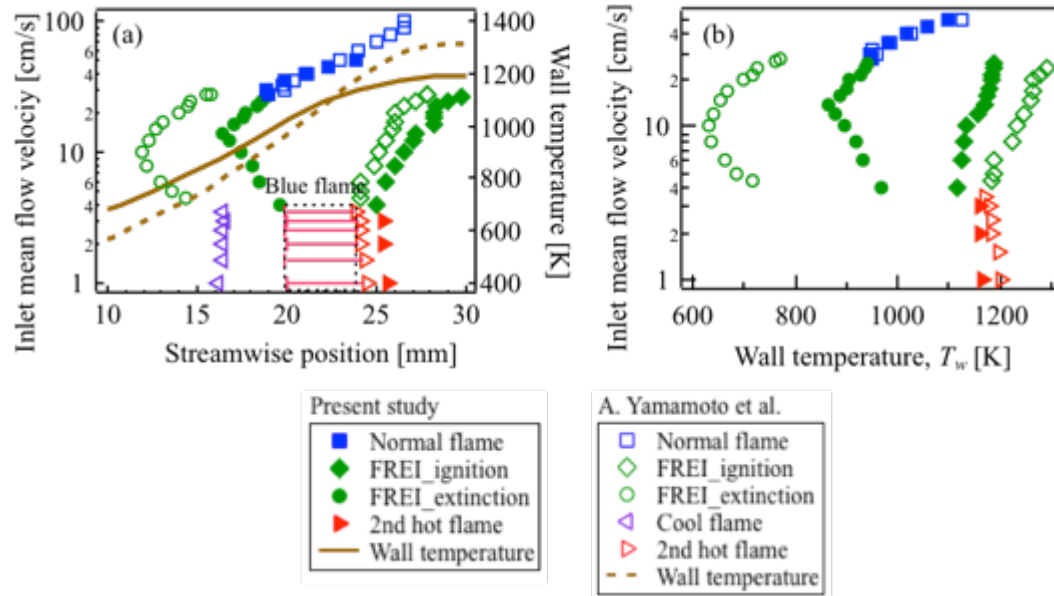
Figure 2-23 Comparison of the flame responses to the flow velocity in the rectangular channel and the previous tube [32].
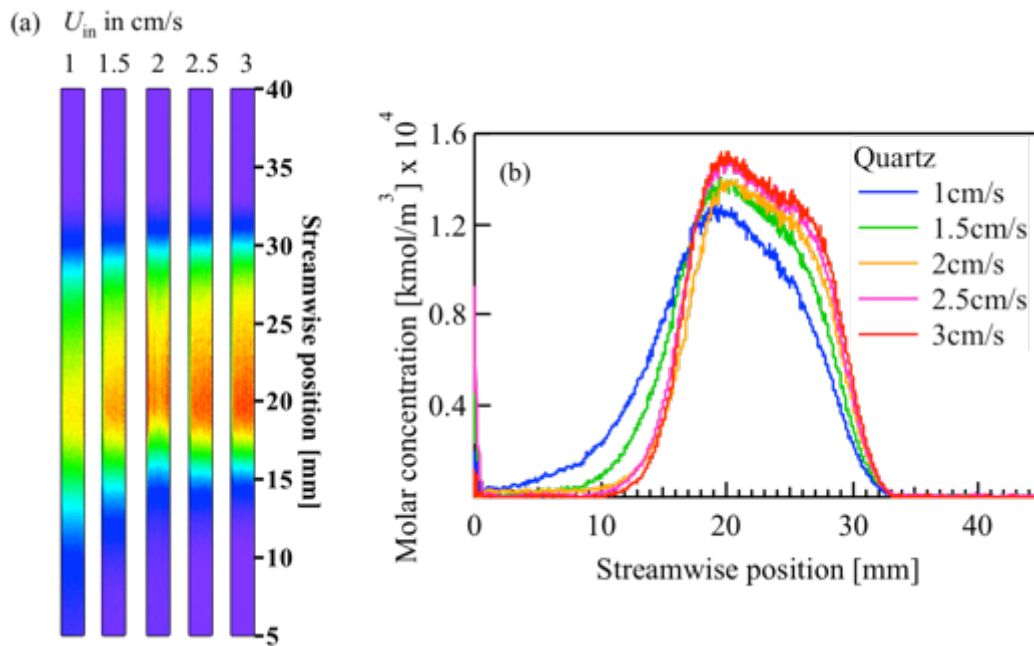


Figure 2-24 HCHO distribution in weak flame with different inlet flow velocities. (a) HCHO-PLIF images, (b) HCHO profiles along the centerline.
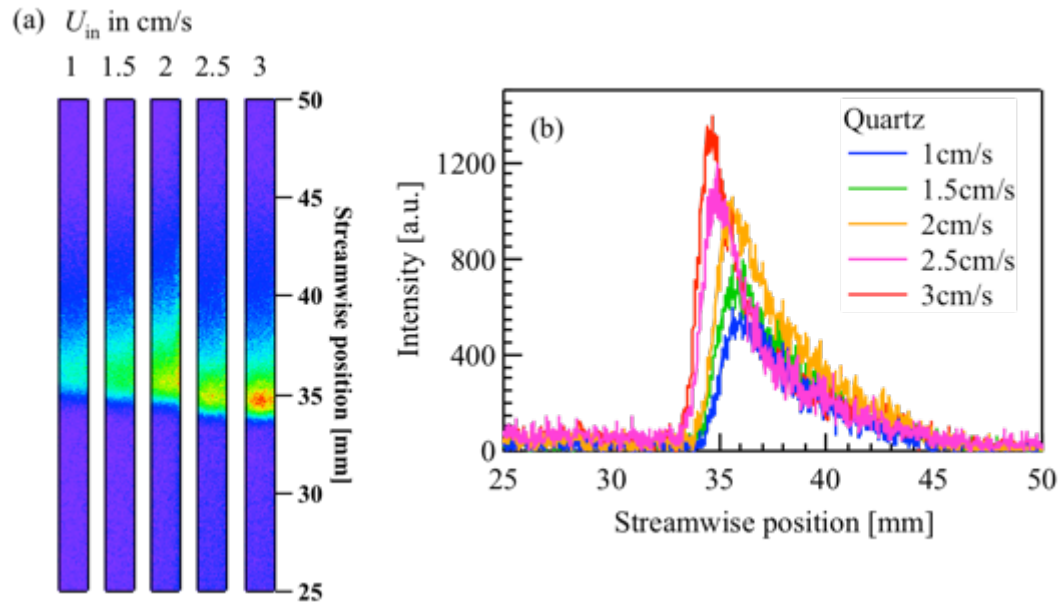
Figure 2-25 OH distribution in weak flame with different inlet flow velocities. (a) OH-PLIF images, (b) OH profiles along the centerline.

# Chapter 3 Radical Quenching Effect on High-temperature Oxidation

In previous studies [16][17][56][57], radical quenching model is used to describe the wall chemical effect on the methane/air normal flame. Active radicals as OH, H, O and $CH_3$ are quenched by the wall surface, which causes the flame quenching. In this chapter, the radical quenching model is applied to both the DME/air weak flame and DME/air normal flame. Quartz, stainless and alumina are the three wall materials used in this study. In order to rule out the influence from the different fuel (methane and DME), the radical quenching effect on the DME weak flame is compared with that on the normal flame of the same DME fuel.

## 3. 1. Preparation of Channel Inner Surface

Quartz, stainless steel type 321 (Fe-Ni(9~13%)-Cr(17~19%)-Ti(>5×C%)) and alumina ($Al_2O_3$) have been used in the wall chemical effect investigation. Quartz is the bulk material of the micro reactor, while 150-nm thin film of SUS321 and alumina are alternatively deposited on the top or the bottom walls. Therefore, the wall thermal boundary condition is kept identical while varying the wall chemical boundary.

SUS321 film is deposited by using a vacuum arc plasma deposition system (ARL-300, ULVAC). The schematic of the arc discharge gun is shown in Figure **3-1** [58]. The trigger electrode is insulated from both the target rod (cathode) and the anode electrode, while capacitors are connected between the target rod and the anode electrode. After the chamber is vacuumed, the voltage applied between the trigger and the target rod induces an arc discharge on the surface of the target rod. Highly ionized metal plasma is generated between the target rod and the anode electrode, and deposits on the substrate. With this method, smooth and dense multilayer nm-order thin film can be formed. And the film thickness can be well controlled by the arc discharge pulse cycles [59]. The deposition of SUS321 is conducted at a voltage of 100 V, a frequency of 2 Hz, and a capacitance of 1080 μF. A SUS321 film of ~150 nm is formed after 3000 cycles.

Alumina film is deposited by using the atomic layer deposition (ALD) system (Savannah S200, CambridgeNanoTech). The principle of ALD film formation is

illustrated in Figure **3-2**. ALD uses sequential, self-limiting chemical processes to precisely grow defect-free film one atomic layer by one atomic layer [60]. For the alumina deposition in this study, tri-methyl aluminum (TMA) is adopted as the precursor, while water vapor is used as the oxidizer. The exposure time for the two precursors is 4 s, and the operating temperature is 300 ºC.

As shown in Figure **3-3**, the arithmetic mean surface roughness Ra measured by atomic force microscopy (AFM) for quartz, alumina and SUS321 surface are 0.6 nm, 1 nm and 2 nm, respectively, which can be considered as smooth enough to neglect the effect of roughness.

## 3. 2. Numerical Simulation

### 3. 2. 1. Simulation Method

Two-dimensional numerical simulation for the DME/air weak flame ($\phi = 0.85$, $U_{in}$ = 2 cm/s) has been conducted in FLUENT with detailed gas-phase and surface reaction mechanisms. Governing equations are mass continuity, Navier-Stokes, species conservation, energy and state equations.

The second-order upwind difference scheme with the SIMPLE method is employed for the simulation of weak flame. The computational domain, shown in Figure **3-4**, is 45-mm-long and 1.5-mm-wide, which has the same width of the present quartz channel, but the length has been reduced to cover only the whole reaction zone for reducing the computational cost. In the case of the two sidewalls having different surface materials in the experiment, different surface reaction mechanisms are applied to the two sidewall boundaries. A computation domain of full width is used in this case. The number of grids is 225 in the streamwise direction and 15 in the wall-normal direction. Unequally-spaced grids are used in the wall-normal direction. The closest grid is 20 μm from the wall. Inlet velocity of the DME/air mixture is Uin = 2 cm/s and the inlet gas temperature is the same as the wall temperature at that position. The top and bottom walls are modeled as non-slip wall boundaries with the same wall temperature profile as measured in the experiment. DME 2000 (79 species, 351 reactions) [22] is adopted as gas-phase reaction mechanism for the DME/air.

### 3. 2. 2. Radical Quenching Mechanism

The radical quenching mechanism [56], listed in Table **3-1**, is used as the surface reaction mechanism, in which $CH_3$, H, O and OH radicals are adsorbed on the wall surface and recombined to form stable gas-phase species ($CH_4$, $C_2H_6$, $H_2$, $O_2$ and $H_2O$). The pre-exponential of the surface recombination is estimated to be $3.7\times10^{21}$ $cm^2mol^{-1}s^{-1}$ according to the transition state theory. It should be noted that the order of pre-exponential factor given in Ref. [56] is not correct. For a recombination reaction of two surface species (X and Y), the pre-exponential factor is given as

$$A = \frac{k_B T}{h_p} \frac{q_T}{q_X q_Y}$$

(3-1)

where $\dfrac{k_B T}{h_p}$ is in the order of $10^{13}$ $s^{-1}$, and the partial function $q$ for the surface species is in the order of $10^{20}$ moles/$m^2$. As a result, the order of pre-exponential factor for a surface recombination reaction should be $\sim 10^{21}$ $cm^2mol^{-1}s^{-1}$.

The adsorption rate is calculated by using the Langmuir-Hinshelwood mechanism with different initial sticking coefficients, $S_0$, for different wall materials, which can be expressed as

$$R_{ads} = S_0 \bullet \frac{1}{\Gamma_{tot}} \bullet \sqrt{\frac{RT}{2\pi W_k}} \bullet X_{surf} \bullet C_{gas}$$

(3-2)

where $\Gamma_{tot}$ is the total surface site, $X_{surf}$ is the empty surface site concentration, $C_{gas}$ is the gas-phase specie concentration, $R$ is the universal gas constant, $T$ is the temperature and $W_k$ is the molecular weight of the gas-phase species. It is found that the flame structure remains unchanged with varying the pre-exponential factors of surface recombination from $10^{19}$ to $10^{23}$ $cm^2mol^{-1}s^{-1}$ in the simulation; therefore, the chemical quenching process in the flame is considered as adsorption-limited. As such, the initial sticking coefficient $S_0$, which is crucial to determine overall surface reaction rate, is evaluated for each surface by matching the measured OH distribution profile and simulated profiles with different $S_0$.

Table 3-1 Radical quenching model [56].

| Reaction | Initial sticking coefficient ($S_0$) or |
|---|---|

|  | Pre-exponential factor ($A$, in unit: $cm^2/mol/s$) |
|---|---|
| $OH + B(s) \rightarrow OH(s)$ | $0 \sim 1$ |
| $H + B(s) \rightarrow H(s)$ | $0 \sim 1$ |
| $O + B(s) \rightarrow O(s)$ | $0 \sim 1$ |
| $CH_3 + B(s) \rightarrow CH_3(s)$ | $0 \sim 1$ |
| $CH_3(s) + H(s) \rightarrow CH_4 + B(s)$ | $3.7 \times 10^{21}$ |
| $2CH_3(s) \rightarrow C_2H_6 + 2B(s)$ | $3.7 \times 10^{21}$ |
| $2H(s) \rightarrow H_2 + 2B(s)$ | $3.7 \times 10^{21}$ |
| $2O(s) \rightarrow O_2 + 2B(s)$ | $3.7 \times 10^{21}$ |
| $H(s) + OH(s) \rightarrow H_2O + 2B(s)$ | $3.7 \times 10^{21}$ |
| $2OH(s) \rightarrow H_2O + O(s) + B(s)$ | $3.7 \times 10^{21}$ |

### 3. 2. 3. Simulated Weak Flame in an Inert Channel

In this thesis, all the simulations without applying surface reactions will be referred as an inert one. Figure **3-5** shows the computed streamwise mole fraction profiles of major species and wall/gas-phase temperature profiles along the centerline of the computational domain for the DME weak flame ($U_{in}$ = 2 cm/s, $\phi$ = 0.85). In this particular simulation, it is assumed that both the top and bottom walls are inert. Three vertical dash lines represent the positions of three heat release rate peaks in the cool flame, the blue flame (1st hot flame) and the hot flame (2nd hot flame), respectively. It was found that the species distributions qualitatively agree with one-dimensional simulation results of the weak flame in the circular tube [31]. Two-stage oxidation of DME is observed. The intermediate species play different roles at each-stage of the reaction. The mole fraction of both $CH_2O$ and $H_2O_2$ increases in the cool flame zone, reaches the peak and then gradually decreases in the 1st hot flame zone. The OH mole fraction profile has only one peak in the hot flame zone. The CO mole fraction profile has one peak at the 1st hot flame zone and a step-increase at the cool flame zone. The $HO_2$ mole fraction profile has one peak at the cool flame zone, and the other at the blue flame zone. The CHO profile has three peaks in the three flame zones.

## 3. 3. Radical Quenching effect on OH Distribution

In this chapter, only the OH wall normal distribution is discussed. Although in the later chapters, it is found that the OH streamwise distribution is also affected by the wall materials in the weak flame. But that is mainly due to the influence of surface reactions to the low-temperature oxidation which causes the delay of the hot flame. Since the change of wall temperature at the OH peak position is only 10 K after both sidewalls are coated with SUS321, and only one sidewall is coated in this chapter, the influence by changes in the streamwise direction will be omitted in this chapter. Addition to the weak flame, radical quenching effect on DME/air normal flame also will be discussed for the comparison.

### 3. 3. 1. Radical Quenching Effect on OH in Weak Flame

In order to compare the OH mole fraction obtained in the simulation and the OH-PLIF intensity measured in the experiment, a normalized OH molar concentration, $C_{OH}^*$, is introduced in the present study. Because the OH-PLIF intensity is proportional to the OH molar concentration, $C_{OH}^*$ can be expressed as

$$C_{OH}^* = \frac{C_{OH}}{C_{OH,\max}} = \frac{I}{I_{\max}} \tag{3-3}$$

where $C_{OH}$ is the OH molar concentration, $I$ is the OH-PLIF intensity, and subscript "max" denotes the maximum value.

Figure **3-6** shows $C_{OH}^*$ distributions calculated from the OH-PLIF images of the 2nd hot flame zone of the DME/air weak flame ($U_{in}$ = 2 cm/s, $\phi$ = 0.85). Figures 3-6 (a), (b) and (c) show results for the quartz-quartz channel, the SUS321-quartz channel and the alumina-quartz channel, respectively. Either SUS321 or alumina is alternatively deposited on the left-hand-side wall only. As shown in Figure **3-6** (a), $C_{OH}^*$ distribution for identical chemical boundary on both sidewalls (quartz-quartz channel case) is symmetric. On the other hand, $C_{OH}^*$ distribution in Figure **3-6** (b) of the SUS321-quartz channel case becomes obviously asymmetric. An obvious decrease in $C_{OH}^*$ can be observed near the SUS321 wall surface. Although it is not obvious in Figure **3-6** (c) of the alumina-quartz channel case, the exact value of $C_{OH}^*$

plotted in Figure **3-7** has a slightly larger value near the alumina wall than near the quartz wall, indicating that the $C^*_{OH}$ distribution is actually slightly asymmetric.

Figure **3-7** shows a comparison of $C^*_{OH}$ profiles in the wall-normal direction among the cases of quartz-quartz, SUS321-quartz and alumina-quartz channels. Profiles are plotted along the wall normal direction where $C^*_{OH}$ reaches its maxima in the streamwise direction. All the discussion below for the wall normal direction are given at the same position. It is shown that $C^*_{OH}$ near both walls are around 0.7 in the quartz-quartz channel case, and $C^*_{OH}$ near the alumina-coated wall is around 0.75 in the alumina-quartz channel case. In contrast, a sharp decrease of $C^*_{OH}$ to around 0.4 near the SUS321-coated wall was observed in the SUS321-quartz channel. Since the laser sheet, the thermal boundary condition and the flow field are kept identical in these three channels, the aforementioned difference in $C^*_{OH}$ near different walls comes from different wall chemical effects. $C^*_{OH}$ near the wall decreases in the order from alumina, quartz to SUS321, which shows that SUS321 is the most active material for radical quenching among these three materials, and alumina is the most inert one.

In current surface reaction model, $S_0$ of all species (CH$_3$, H, O and OH) in the surface adsorption reactions is given the same value. In Figure **3-7**, $C^*_{OH}$ profiles for the DME weak flames predicted with different $S_0$ are plotted together with the measured $C^*_{OH}$ profiles in quartz-quartz, SUS321-quartz and alumina-quartz channels. It is shown that the simulated $C^*_{OH}$ profile for $S_0 = 0.0015$ has the best agreement with the measured data in the quartz-quartz channel. Thus, $S_0$ for quartz surface in the weak flame is estimated as 0.0015. Since the right-hand-side wall is quartz in all the present experiments, $S_0$ for the wall is kept at 0.0015 in the simulation. Only $S_0$ for the left-hand-side wall is changed to see if it produces a best matching with the measured data in the alumina-quartz and SUS321-quartz channels. Following this procedure, $S_0$ for SUS321 and alumina is estimated as 0.006 and 0.001, respectively.

# Radical Quenching Effect on High-temperature Oxidation

### 3. 3. 2. DME/air Normal Flame in Parallel Plates

The estimated initial sticking coefficients for quartz and SUS321 from the DME/air weak flame are orders lower than that estimated from previous methane/air normal flame research [17]. In order to confirm the differences are not from the different fuel, experiments of the DME/air normal flame have also been conducted.

The DME/air normal flame is formed in the same parallel wall channel as used in Saiki et al.'s experiments of methane/air normal flame [16][17], as shown in Figure **3-8**. The gap between the two parallel plates is 3 mm. The equivalence ratio for the DME/air normal flame is set as 0.7, since the DME has a lower ignition temperature than methane. If the same equivalence ratio (0.95 for Saiki et al.'s methane/air normal flame experiment) is used, the flame ignites in the porous burner.

The DME/air normal flame is also simulated with Fluent. Same settings as used in Saiki et al. [16][17],, including the calculation domain (grid number: 128 × 32), the scheme (First-order upwind difference scheme with the SIMPLE method), the wall boundary condition (no-slip/isothermal boundary) and the outlet boundary condition are adopted. The inflow boundary condition is given an equivalence ratio of 0.7 and $T = T_w$, while the inlet flow velocity is calculated to give a constant mass flow rate for all different inlet temperatures. Same as the weak flame case, DME 2000 is adopted as the gas-phase reaction mechanism, while the radical quenching model is adopted as the surface reaction mechanism.

### 3. 3. 3. Radical Quenching Effect on OH in Normal Flame

Similarly, OH concentration is normalized in the case of the DME/air normal flame ($\phi$ = 0.7). The $C_{OH}^*$ distributions in the vicinity of the quartz and SUS321 surfaces at Tw = 873, 1073 and 1173 K are shown in Figure **3-9**. When Tw = 873 K, the wall chemical effect is suppressed due to the low gas-phase temperature in the vicinity of the surface. The OH generation rate near the wall is so low that the concentration is nearly 0 for both quartz and SUS321 surface. Therefore, no further OH concentration difference can be caused by different wall materials. However, when Tw ≥ 1073 K, wall chemical effect starts to play an important role. The $C_{OH}^*$ over the SUS321 surface is lower than that over the quartz surface.

# Radical Quenching Effect on High-temperature Oxidation

An estimation of the initial sticking coefficient for quartz and SUS321 in the DME/air normal flame is given in Figure **3-10**. Profiles are plotted along the wall normal direction where $C_{OH}^*$ reaches its maxima in the streamwise direction. When Tw = 873 K, simulated OH distributions are not altered with varying $S_0$, and fit very well with the experimental data. When Tw $\geq$ 1073 K, the simulated near-wall OH concentration is decreased with increasing $S_0$. For both Tw = 1073 and 1173 K, the simulated OH wall normal distributions of $S_0$ = 0.01 and 0.1 fit very well with the measured distributions over the quartz and SUS321, respectively. Therefore, in the DME/air normal flame, the estimated initial sticking coefficients are 0.01 for quartz and 0.1 for SUS321, which are identical to the previous estimated values in the $CH_4$/air normal flame [17], but orders higher than the estimated values in the DME/air weak flame.

## 3. 4. Sensitivity Analysis

One raised issue from the above discussion is that estimated $S_0$ for SUS321 and quartz in the weak flame are much lower than that in the normal flame. This might be caused by assuming equal $S_0$ for all four species (H, O, OH and $CH_3$). In fact, $S_0$ could have different value for different species. Therefore, it is necessary to identify which adsorption has more significant influence on the OH distribution in both normal and weak flames. The $S_0$ setting in the simulation of the SUS321-quartz channel has been adopted as the standard setting in the sensitivity analysis. In each sensitivity test, the initial sticking coefficient for only one of the 4 species over the SUS321 surface (left sidewall) is tuned from 1 to $10^{-12}$ ($10^{-12}$ has been considered as 0 in below) to examine the sensitivity of OH profile to $S_0$ of that species.

### 3. 4. 1. Influence of $S_A$ on OH Distribution

In Figure **3-11**, the absolute OH molar concentrations in weak flame with varying $S_{OH}$, $S_H$, $S_O$ and $S_{CH3}$ separately are plotted in comparison with the result from the equal $S_0$ model. In each subfigure, the red solid line is the absolute OH molar concentration for the simulation with the equal $S_0$ model; the lines with marks are the results when the initial sticking coefficient for one of the four species is tuned to different values. It is shown that the OH concentration has the largest variation when the initial sticking

coefficient for OH has been tuned from 0 to 1; while no obvious change is observed when tuning the initial sticking coefficient for $CH_3$. Noticeable OH concentration changes are observed when tuning the initial sticking coefficient for H and O atom. Figure **3-12** shows similar sensitivity analysis, but for the DME/air normal flame. The wall normal direction profiles discussed below are all plotted at the position where OH has its maximum concentration. In contrast to the weak flame case, turning the $S_0$ of H, instead of OH, gives the largest OH concentration variation in the methane normal flame. A slight variation of OH distribution is observed when turning the initial sticking coefficient for O from 0 to 1, but similarly as in the weak flame, no obvious change on OH distribution is observed when turning the initial sticking coefficient for $CH_3$.

### 3. 4. 2. Reactions Contributed to OH Concentration

The sensitivity of gas-phase OH concentration to $S_0$ of H and O depends on the H and O related OH gas-phase generation and destruction reactions. R1-5 listed in Figure **3-13** are identified as H and O related reactions that have the largest contributions to the OH generation/destruction for both weak and normal flames. Noticeable differences between reaction rates for $S_{H \text{ or } O} = 0$ and 1 are observed in Figure **3-13**, especially for the $S_H$ case. It is interesting to note that tuning the initial sticking coefficient for H on the left sidewall ($y=0$) of weak flame also changes the reaction rate over the right sidewall ($y=1.5mm$). The black dash lines in Figure **3-13** (a) and (c) show the OH net generation rate attributed to R1-4 for $S_H = 0$ and 1, and the lines in Figure **3-13** (b) and (d) show the OH net generation rate attributed to R1-2 & 5 for $S_O = 0$ and 1. It is apparent from these data that close to the wall, due to the above O and H related reactions, a larger OH generation rate (or a smaller OH destruction rate) can be obtained for the $S_{H \text{ or } O} = 0$ than that for $S_{H \text{ or } O} = 1$. An integration of OH generation/destruction rate in the wall normal direction shows that, in the weak flame, the OH net destruction rate attributed to R1-4 is 16% slower for $S_H = 0$ than that for $S_H = 1$; and this destruction rate is reduced by 10% in the normal flame. In the weak flame, the reaction that contributes to most of the OH concentration change when tuning the $S_O$ is R5. Due to the surface destruction of O, the near-wall O concentration drops, leading to a decreased OH generation rate within

$y = 0.4$ mm. Similar phenomenon is observed in the normal flame as well within $y = 0.2$ mm.

### 3. 4. 3. Normalized Sensitivity Coefficient

The normalized sensitivity coefficient of $S_0$ in the present study is defined as follow:

$$ST_{S_A=x} = f_{S_A=x} \cdot \frac{\sqrt{\frac{1}{n}\left(\sum_{i=1}^{n}(C_{OH,S_A=x,i} - C_{OH,i})^2\right)}}{\sqrt{\frac{1}{n}\left(\sum_{i=1}^{n}(C_{OH,S_{OH}=1,i} - C_{OH,i})^2\right)}} \tag{3-4}$$

where '$A$' in the $S_A$ denotes H, O, OH or $CH_3$; $x$ is the value of the initial sticking coefficient (from 1 to 0); $i$ is the index of mesh grids in the wall normal direction, while n is the total grid number; and $f_{S_A=x}$ is given as follow:

$$f_{S_A=x} = \begin{cases} 1 & if \quad C_{OH,S_A=x,1} - C_{OH,1} \leq 0 \\ -1 & if \quad C_{OH,S_A=x,1} - C_{OH,1} > 0 \end{cases} \tag{3-5}$$

Noted that $i = 1$ is corresponding to the grid on the SUS321 surface; $i = n$ indicates that the grid is on the quartz surface.

Figure **3-14** shows the normalized sensitivity coefficients of $S_0$ for all 4 species in both normal and weak flames. Since the estimated initial sticking coefficients in normal and weak flames do not agree with each other when using the equal $S_0$ model, a direct comparison of the normalized sensitivity coefficients between weak flame and normal flame is not meaningful. However, different trends of the normalized sensitivity coefficient with varying $S_0$ implies different processes governing wall chemical effects on these two types of flame.

Since the initial sticking coefficients for SUS321 has been estimated as 0.006 for the equal $S_0$ Model in the weak flame, the sensitivity coefficients for $S_{OH, H, O \text{ or } CH3} = 0.006$ should be zero. In the weak flame, normalized sensitivities are nearly the same for all 4 species. Tuning the $S_{OH, H, \text{ or } O}$ from 1 to 0.1 only decreases the sensitivity coefficient by 11.9%, 10.7% and 12.6%, respectively. When the $S_0$ equal to 1 or 0.1, the surface site coverage is in the order of $10^{-5}$, which means that the surface reaction is still under the adsorption control. Therefore, the reason for small sensitivities is the

# Radical Quenching Effect on High-temperature Oxidation

low near-wall gas-phase species concentration. On the other hand, when tuning the $S_{OH, H, or O}$ from 0.1 to 0.01 (similarly from 0.01 to 0.001), the amplitude of decrease climbs up to 74.7%, 72.8% and 75.9%, respectively. When further tuning the $S_{OH, H, or O}$ from 0.001 to 0.0001, the sensitivity coefficient is decreased by 30.8% and 32.2% and 28.8%, respectively, even though their plots in Figure **3-11** are already very close to each other. Tuning the $S_{OH, H, or O}$ from 0.0001 to $10^{-12}$ only leads to a decrease of less than 3% in each sensitivity coefficient, which indicates that, when the $S_0$ is lower than 0.0001, the adsorption of the certain species is too slow to exert any significant impact on its gas-phase concentration.

Since the initial sticking coefficients for SUS321 has been estimated as 0.1 for the equal $S_0$ Model in the normal flame, the sensitivity coefficients for $S_{OH, H, O or CH3} = 0.1$ are all zero. Similar as in the weak flame, normalized sensitivities are almost the same for $S_0$ equal to 0.0001 and 0. The sensitivity increments for tuning the $S_{OH, O or CH3}$ from 0.0001 to 0.001 are less than 6%, and 9% for the $S_H$. Therefore, when $S_0$ is lower than 0.001, the adsorption of the certain species is not likely to have large impact on the normal flame. The limit value of $S_0$ is one order higher than that in the weak flame, which could be due to the faster gas-phase reaction rate in the normal flame. The surface reactions need to be fast enough to compete with the gas-phase reaction in order to cause the impact.

The most striking result from these data is that, as mentioned before, the adsorption of species, which the OH concentration is more sensitive to, are not the same for the weak flame and normal flame. In the weak flame, OH concentration is most sensitive to the adsorption of OH. The normalized sensitivity coefficient of $S_H$ are only half of that of $S_{OH}$, but approximately double of that of $S_O$, while the normalized sensitivity coefficients of $S_{CH3}$ are always less than 0.1. It indicates that, the surface destructions of H and O do have unneglectable impact on the OH concentration, because both H and O atom are the reactants for the OH formation; but the direct adsorption of OH exerts the largest influence. However, in the normal flame, OH concentration is much more sensitive to the adsorption of H than that of OH. The absolute value of normalized sensitivity coefficient of $S_H$ is 1.5 times higher than that of $S_{OH}$, when the initial sticking coefficient is set as 0. Unlike that in the weak flame, the OH concentration is not very sensitive to the adsorption of O; the sensitivity coefficient is only around 25% of that of $S_{OH}$. The sensitivity coefficient of $S_{CH3}$ remains an extremely low value in the normal flame.

### 3. 4. 4. Radical Diffusion

The fact that the OH distribution is most sensitive to $S_{OH}$ in the weak flame, but in the normal flame most sensitive to the $S_H$ is attribute to the difference in mass diffusion in the wall normal direction. Figure **3-15** shows the molar flux of OH, H and O in the wall normal direction for both weak and normal flames with the equal $S_0$ model. Generally speaking, the mass diffusion in wall normal direction is much faster in the normal flame than that in the weak flame. In the weak flame, OH and H have similar molar flux, e.g. at $y = 0.1$ mm the molar flux of OH and H towards wall surface are $4.1 \times 10^{-4}$ and $4.6 \times 10^{-4}$ mol/(m$^3$s). However, in the normal flame, the molar flux of H becomes much larger than that of OH, e.g. at $y = 0.1$ mm the H molar flux to wall is 0.06 mol/(m$^3$s), over 2 times of that of OH. It has to be noted that the gas-phase reactions happen in the whole channel, on the other hand, the surface reactions only happen on the wall, which means that the change of gas-phase species distribution with different wall surfaces are the result of both the reaction kinetic and mass diffusion. When the mass diffusions of OH and H are in the same level, such as in the weak flame, the direct adsorption of OH has greater impact on the wall normal OH distribution. However, in the normal flame, since the mass diffusion of H is much faster than OH, varying the H adsorption rate leads to a greater H concentration change than the OH adsorption does to OH. Moreover, the subsequent OH concentration change caused by the H concentration change is still larger than that of the direct OH adsorption on surface. Therefore, OH concentration is more sensitive to the adsorption of H than OH.

This study was limited by the absence of experimental data for species as H and O. Obtaining different $S_0$ for OH, H and O cannot be achieved from only the OH measurement data. Notwithstanding these limitations, this study suggests that the adsorption of OH, H and O all have contributions to the OH distribution in the gas-phase, and the species that has the greatest impact can be different for different flames. This could be the reason for the different estimated $S_0$ in the weak flame and normal flame when using the equal $S_0$ model. Further experimental data for the H and O distribution is needed to estimate the $S_0$ for each species separately.

## 3. 5. Summary

The radical quenching effect of alumina, quartz and SUS321 wall surfaces on the DME/air weak flame in a rectangular micro channel with a streamwise temperature gradient has been investigated through OH-PLIF measurements and numerical simulations.

It is found that the normalized OH molar concentration increases in the order of SUS321 surface, quartz surface, alumina surface, which indicates that surface activity for radical quenching decreases in the order of SUS321, quartz and alumina. This result is same as that found in the normal flame. The initial sticking coefficient, $S_0$, in the radical quenching model is estimated for alumina, quartz and SUS321 as 0.001, 0.0015 and 0.006, respectively, by matching the experimental data and the simulated results. The estimated $S_0$ for quartz and SUS321 in the weak flame are much lower than the value of 0.01 for quartz and 0.1 for SUS321 in previous methane/air normal flame studies.

Concerning the cause of different $S_0$ in the DME weak flame and methane normal flame, the influence of fuel has been ruled out after finding out that $S_0$ estimated in the DME normal flame and methane normal flame are the same. This indicates that the different $S_0$ in the DME weak flame and methane (or DME) normal flame is caused by the difference in two types of flames. A sensitivity analysis has been conducted for both the weak flame and the normal flame, by varying the initial sticking coefficient of one of the H, O, OH and $CH_3$ radicals from 0 to 1. It is shown that the OH concentration is most sensitive to the adsorption of OH in the weak flame, and has noticeable sensitivity to the adsorption of H and O. On the other hand, in the normal flame, the OH concentration is more sensitive to the adsorption of H than the adsorption of OH. The adsorption of H causes the decrease of the OH concentration through reducing the OH generation rate from the gas-phase. A comparison of the diffusion rate in wall normal direction shows that the diffusion of H is much faster than that of OH in the normal flame, but they are the same level in the weak flame. Since the radical diffusion in wall normal direction limits the destruction rate over the surface, the near-wall OH concentration in the normal flame is more sensitive to H adsorption.

The initial sticking coefficients for all radicals have been assumed equal for a certain surface material in the current radical quenching model, which is not

necessarily true. The different $S_0$ estimated in the weak and normal flame might be a result of this assumption. Direct measurement of other species such as H and O is necessary in order to improve the radical quenching model by introducing different $S_0$ for each species.
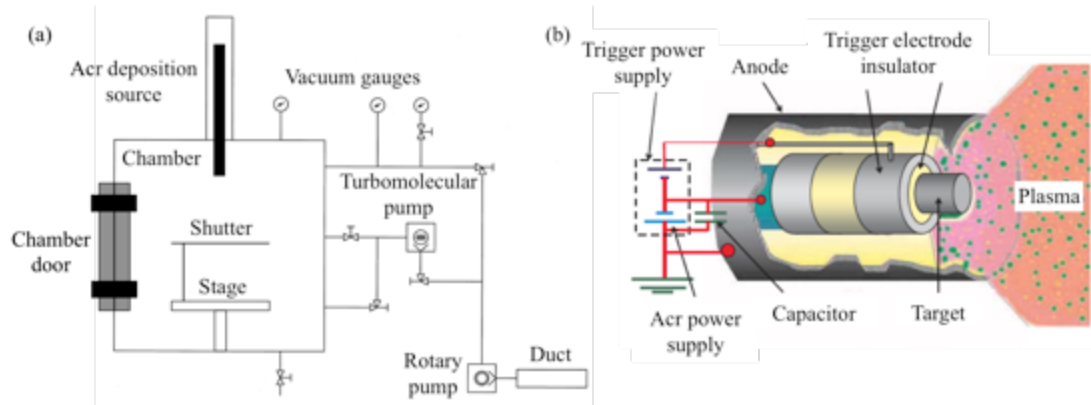
Figure 3-1 (a) Schematic diagram of arc plasma deposition system. (b) Conceptual diagram of the arc deposition source [58].
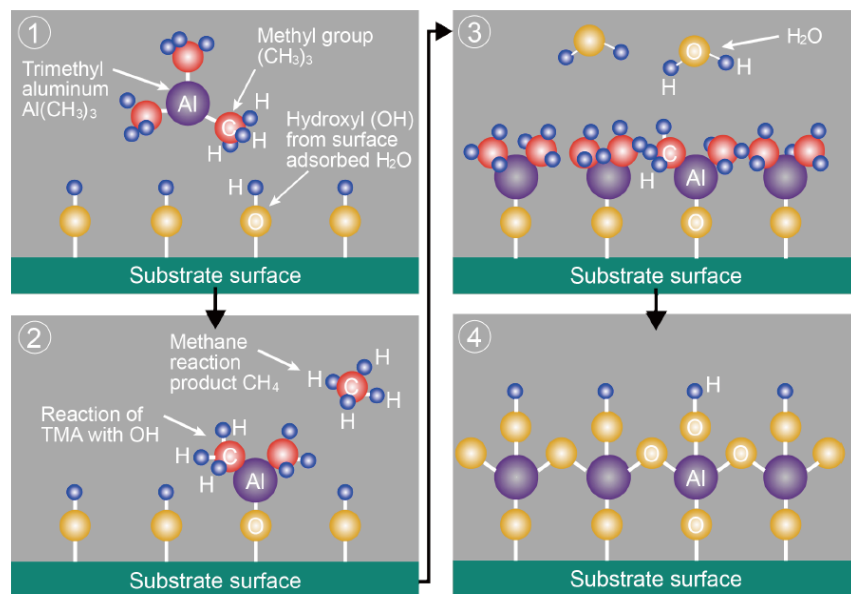


Figure 3-2 Principle of atomic layer deposition using self-limiting surface chemistry and binary reaction sequence.
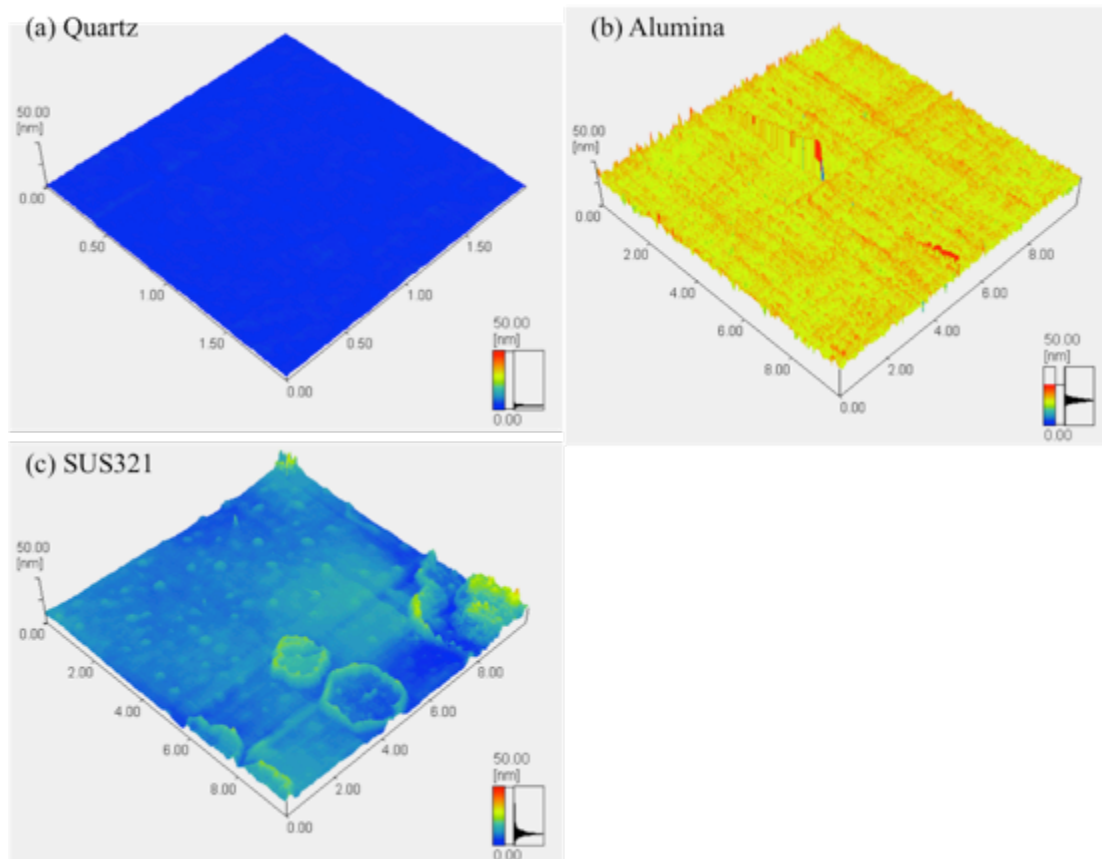
Figure 3-3 Surface roughness distributions taken by atomic force microscopy (AFM).

(a) Bulk material - quartz, (b) ALD - alumina, (c) APD – SUS321.
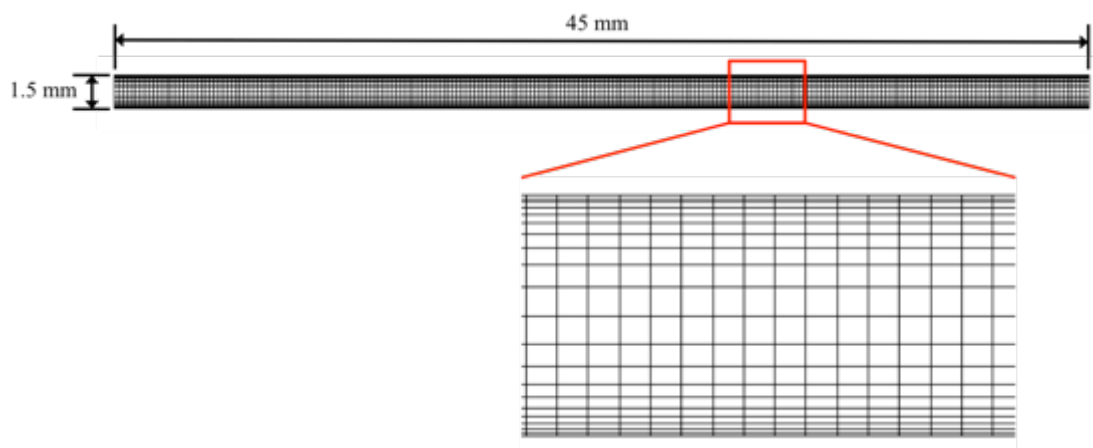


Figure 3-4 Mesh in 2D simulation of the weak flame.

# Radical Quenching Effect on High-temperature Oxidation
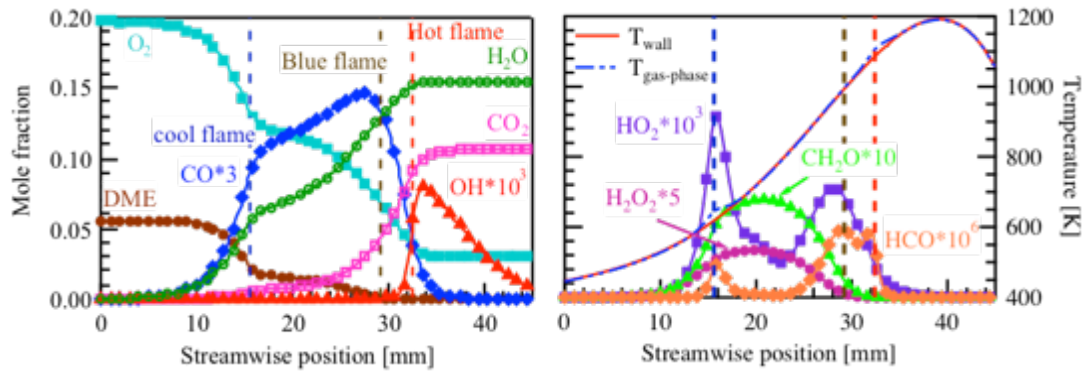


Figure 3-5 Computed streamwise mole fraction profiles of major species and wall/gas-phase temperature profiles for a DME/air weak flame ($U_{in}$ = 2 cm/s, $\phi$ = 0.85). Vertical dash lines are drawn at heat released rate peaks.
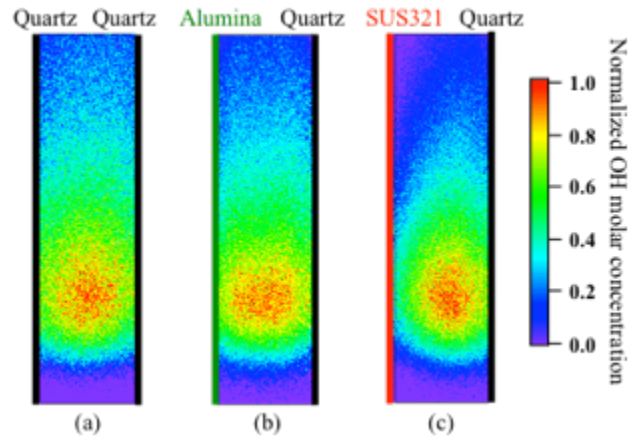


Figure 3-6 Normalized OH molar concentration distributions for DME/air weak flames. (a) Quartz-quartz channel, (b) alumina-quartz channel and (c) SUS321-quartz channel. Alumina and SUS321 are on the left sidewall.
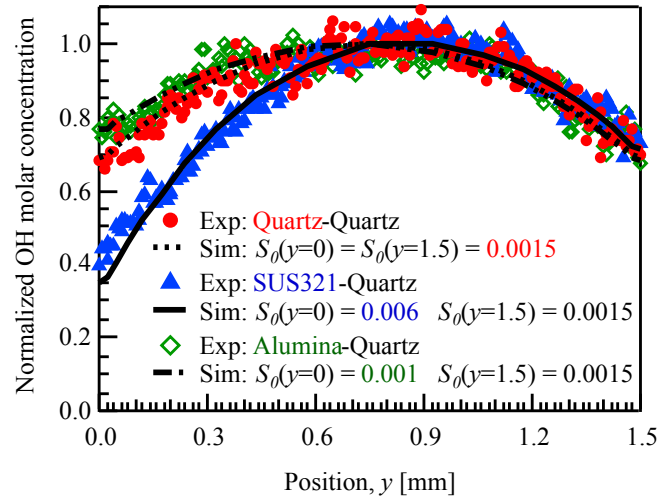
Figure 3-7 Wall-normal distribution profiles of normalized OH molar concentration for DME/air weak flames in quartz-quartz, SUS321-quartz and alumina-quartz channels. Simulated distributions with different initial sticking coefficient $S_0$ are also shown here.
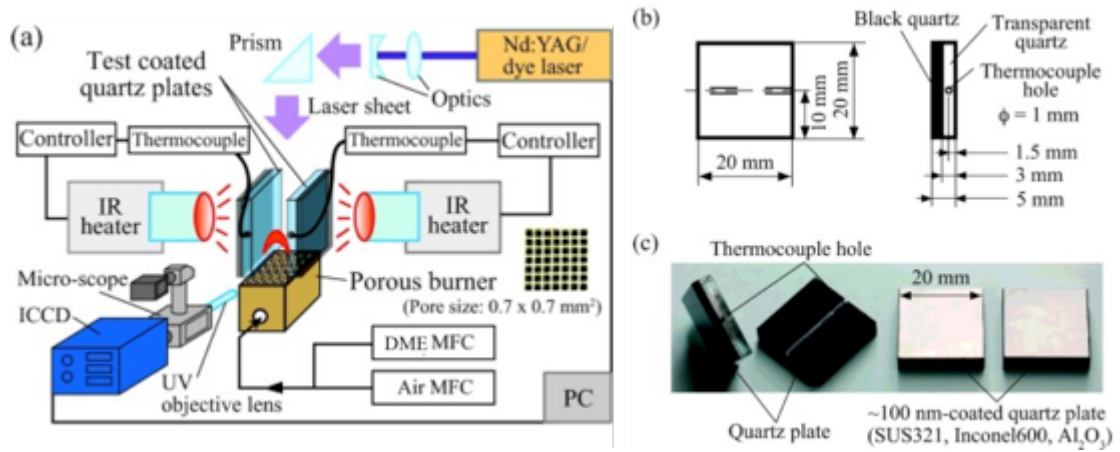


Figure 3-8 Experimental setup for a normal flame in 3 mm channels: (a) microscopic OH-PLIF setup, (b) dimension of quartz plate, and (c) photos of test quartz plates with/without surface coatings. [17]
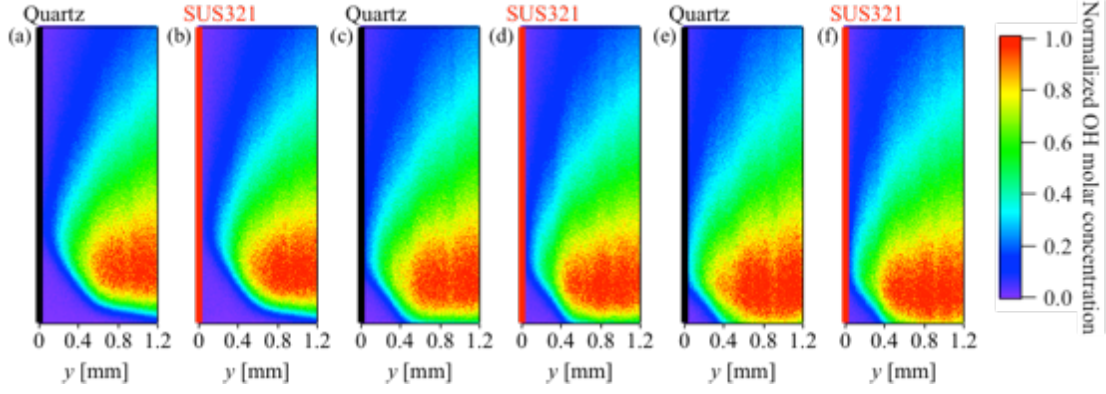
Figure 3-9 Normalized OH molar concentration distributions for DME/air normal flames ($\phi = 0.7$) in the 3 mm channel. (a) quartz at $T_w = 873$ K, (b) SUS321 at $T_w = 873$ K, (c) quartz at $T_w = 1073$ K, (d) SUS321 at $T_w = 1073$ K, (e) quartz at $T_w = 1173$ K, (f) SUS321 at $T_w = 1173$ K.
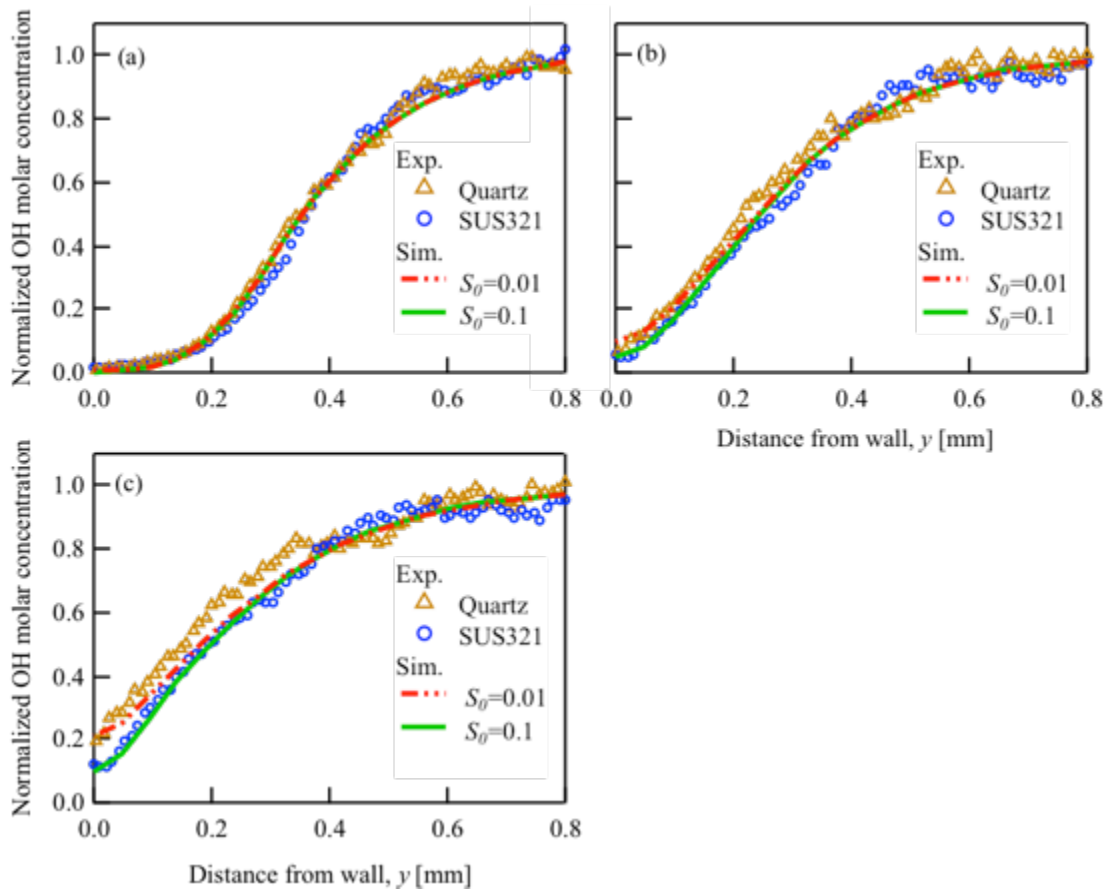


Figure 3-10 Wall-normal distribution profiles of normalized OH molar concentration in DME/air normal flames over quartz and SUS321 surfaces at (a) $T_w = 873$K, (b) $T_w = 1073$K and (c) $T_w = 1173$K. Simulated distributions with different initial sticking coefficient $S_0$ are also shown here.
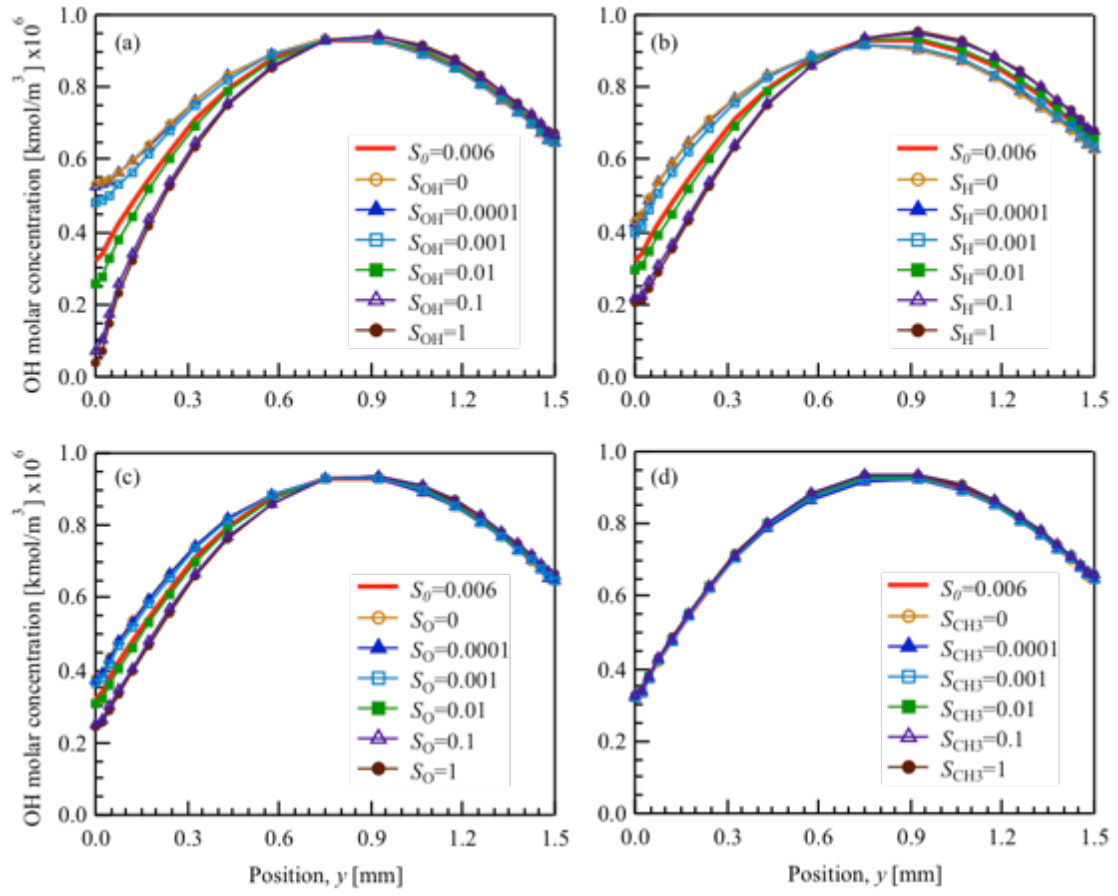
Figure 3-11 Simulated wall-normal distribution profiles of absolute OH molar concentration in the weak flame with the equal $S_0$ model and the $S_A$-tuned model. (a) $S_{OH}$, (b) $S_H$, (c) $S_O$, (d) $S_{CH3}$ at $y=0$ are tuned from 0 to 1.
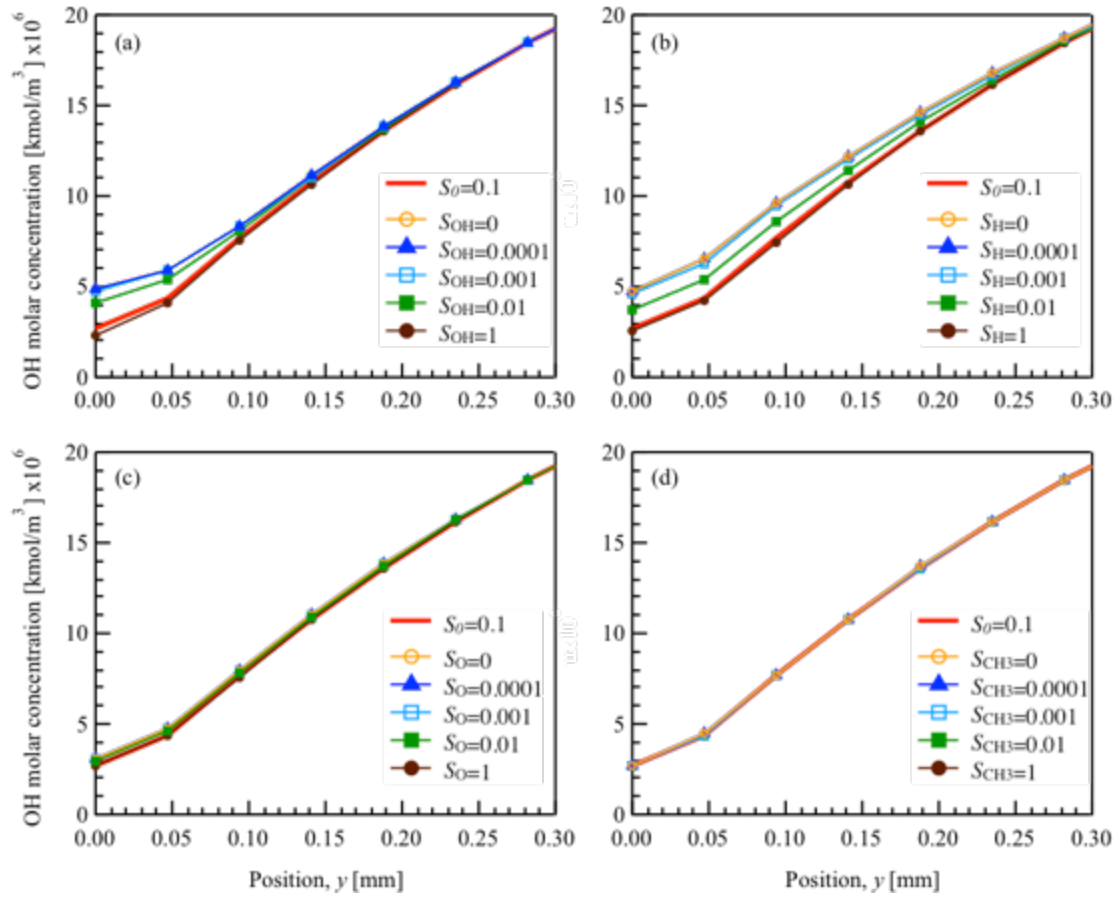
Figure 3-12 Simulated wall-normal distribution profiles of absolute OH molar concentration in the normal flame with the equal $S_0$ model and the $S_A$-tuned model. (a) $S_{OH}$, (b) $S_H$, (c) $S_O$, (d) $S_{CH3}$ at $y=0$ are tuned from 0 to 1.
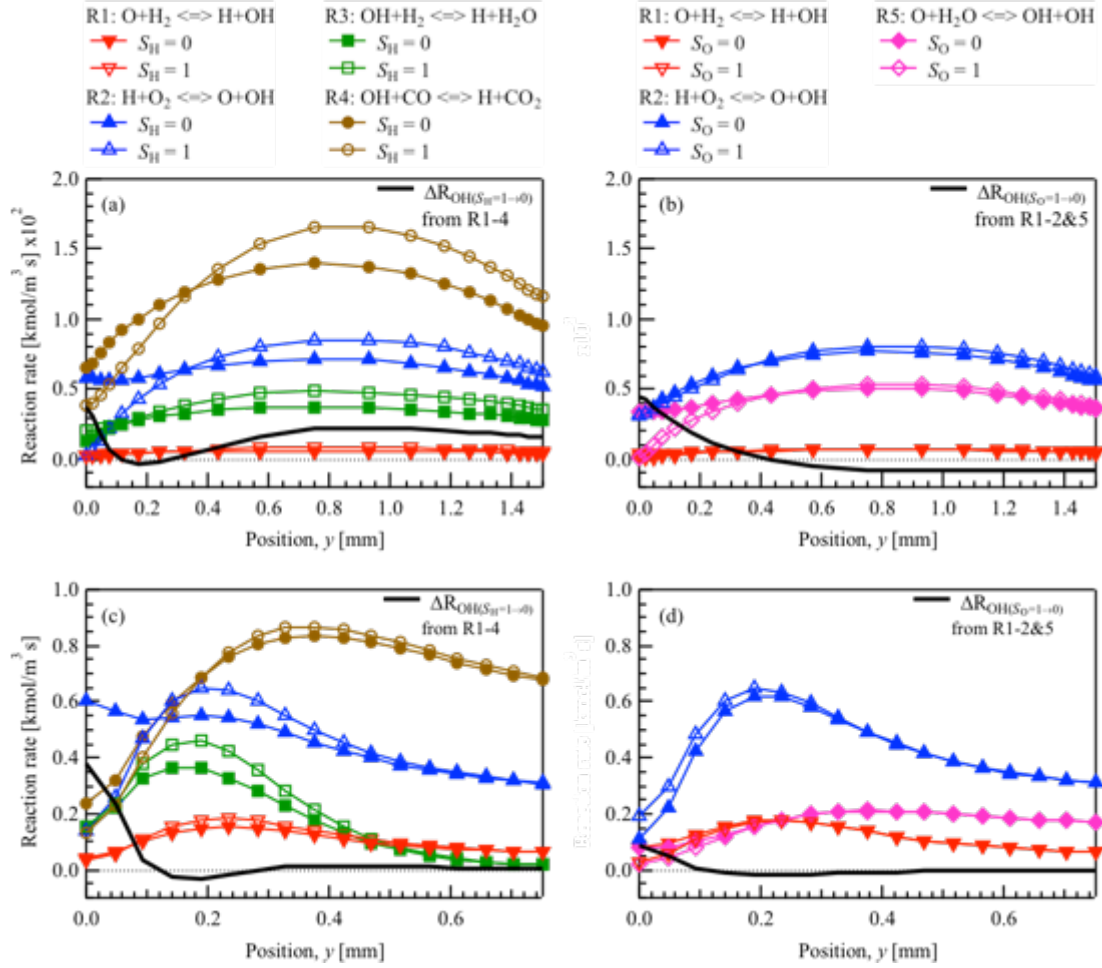
Figure 3-13 Reaction rates of major contributing reactions to OH. $S_{H \text{ or } O}$ are tuned from 0 to 1. (a, b) Weak flame; (c, d) Normal flame.
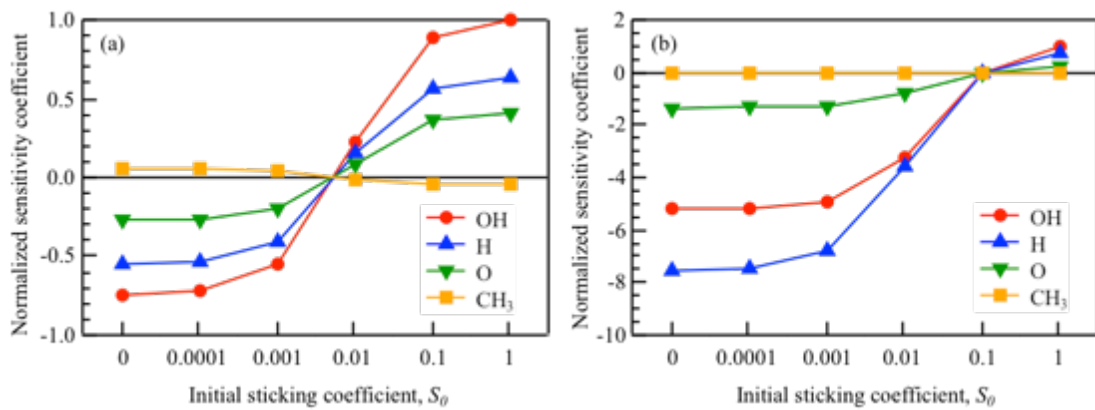


Figure 3-14 Sensitivity of absolute OH molar concentration to initial sticking coefficient of OH, H, O and $CH_3$. (a) Weak flame; (b) Normal flame.
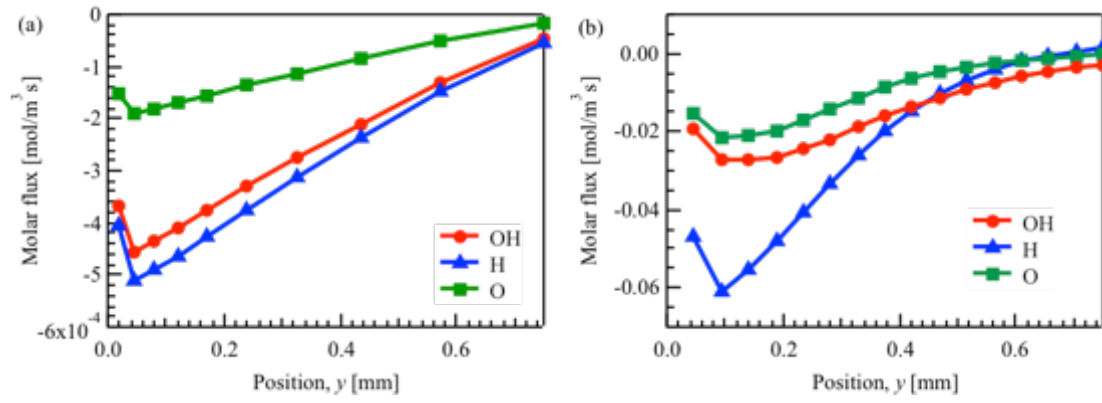
Figure 3-15 Chemical molar flux towards the wall surface. (a) Weak flame; (b) Normal flame.

# Chapter 4 Wall Chemical Effect on Cool Flame

In this chapter, the effect of wall surface material on streamwise distribution of species in the DME/air weak flame ($\phi$ = 0.85, $U_{in}$ = 1.5 cm/s) has been investigated. DME, CO and $CO_2$ concentrations were measured with gas chromatography, while OH and HCHO concentrations were measured with the PLIF system.

It was shown in Chap. 3 that the near-wall OH concentration over quartz is only slightly lower than that over alumina (considered as inert material for radical quenching), resulting in an estimated $S_0$ for quartz in the weak flame as low as 0.0015. Since the streamwise distribution of species is unlikely to be affected by such low $S_0$, quartz was treated as an inert material in this chapter. In previous studies of the methane/air normal flame [17][18], it was found that besides SUS321 and Inconel600, SiC has a relatively large radical quenching effect. As such, SUS321, Inconel600 and SiC are chosen for the study of wall chemical effect on weak flame in this chapter. To further understand individual roles of the composition in these alloys on the species distribution in the weak flame. The three main metal elements in SUS321 and Inconel600, i.e. pure metals of iron, nickel and chromium, are also studied.

## 4. 1. Gas Chromatography Analysis

Figure **4-1** shows an overall schematic for the gas chromatography analysis. Syringes are used to sample the gas out from the flame. The gas sample is analyzed in the gas chromatography system with either the mass spectrometry (MS) or the thermal conductivity detector (TCD). Since this is not an in-situ measurement, only the stable molecules in room temperature and atmosphere were measured in this study.

### 4. 1. 1. Gas Sampling

The reactor is made disassemblable, and a replaceable sidewall with gas sampling holes is designed for the GC measurement, as shown in Figure **4-2**. Seven $\phi$0.6 mm holes are opened along the centerline of the sidewall. The space between two adjacent holes is 5 mm, and the last hole at the downstream side is located at the position

corresponding to the highest wall temperature point. The holes are sealed with quartz plugs to prevent leakage when not in use.

A syringe pump (YSP-201, YMC) with a gastight syringe is used for sampling the gas from the flame, as shown in Figure **4-3**. A quartz needle with inner diameter of 0.2 mm, outer diameter of 0.55 mm and length of 70 mm is insert into the sampling hole. With the syringe pump, a constant sampling rate as low as 20 μL/min is controlled. 60 μL gas is sampled in 3 minutes using a 100-μL-volume micro syringe (HAMILTON 1710) for the GC-MS measurement; 120 μL gas is sampled in 6 minutes using a 250-μL-volume micro syringe (HAMILTON 1725) for the GC-TCD measurement. A syringe valve is placed between the syringe and the needle, which is closed immediately after sampling to prevent ambient air coming inside. The quartz needle is then replaced by a stainless needle (inner diameter: 0.18 mm, outer diameter: 0.52 mm, length: 50 mm) for the injection of the gas sample to the GC machine. Before the injection, the first 20 ~ 30 μL of gas sample is thrown away to push out the air in the stainless needle. Therefore, the injected volume of the gas sample are ~ 20 μL for GC-MS and ~ 100 μL for GC-TCD. After each measurement, the syringe and the needle are vacuum cleaned by a vacuum pump.

## 4. 1. 2. Gas Chromatography

Chromatography is a technique to separate the components in a mixture according to their sorption characteristics between two different phases: a liquid or solid stationary with a large surface and the carrier gas as the moving phase. There are three typical chromatographic development techniques: frontal analysis, displacement development and elution development. In the gas chromatography, elution development is employed. The rates of different components traveling through the column are determined by their retention on the solid packing. When the sorption rate of each component is largely different, or the column is sufficiently long, all the components can be fully separated from others. As a result, in the chromatogram, each peak marks a certain component, and the peak area stands for its amount. Moreover, when the moving phase flow rate and the column temperature program stay same among different trials, the position of the peak maximum on the abscissa also remains same for a certain component.

A 30 m-long Rtx-624Sil MS (fused silica) column is used for separating DME and Kr in this study. The inner diameter of the capillary column is 0.25 mm, and a 1.4 μm-thick mid-polarity Crossbond$^{TM}$ silarylene phase film is coated over the inner surface. The maximum operating temperature can reach 300-320 ℃. CO, $CO_2$ and Kr are separated with a Micropacked ST column. It is a molecular sieve packed column with ShinCarbon-ST as a packing material. The mesh size is 80-100, and the column is 2 m long with a 1 mm-inner diameter.

### 4. 1. 3. Mass Spectrometry

The schematic diagram of a mass spectrometry is illustrated in Figure **4-4** [61]. The gas sample traveled through the GC column is introduced to the electron ionization (EI) source via a transfer line, and then ionized to producing molecular and/or fragment ions. The ion beam will be focused by lenses and then introduced to the quadrupole mass analyzer. The mass analyzer can separate the ions according to their mass-to-charge (m/z) ratio. With a repeatedly scan from the mass analyzer, the ion detector can record the mass spectrum of the analytes.

The quadrupole mass analyzer consists four parallel cylinder rods oriented in a square arrangement as shown in Figure **4-4**. Each pair of opposite rods is connected to each other. An electrical voltage consist DC voltage *U* and AC voltage *Vcos(ωt)* is applied between the two pairs. Therefore, the motions of an ion with mass m and charge q can be described by the following equations in a Cartesian coordinate [62]:

$$\frac{\partial^2 x}{\partial t^2} = -\left(\frac{q}{m}\right)\frac{U + V\cos(\omega t)}{r_0^2}x \tag{4-1}$$

$$\frac{\partial^2 y}{\partial t^2} = \left(\frac{q}{m}\right)\frac{U + V\cos(\omega t)}{r_0^2}y \tag{4-2}$$

$$\frac{\partial^2 z}{\partial t^2} = 0 \tag{4-3}$$

where $r_0$ is half of the minimum distance between the two opposite electrodes. As such, with certain radiofrequency (RF) of the AC portion and direct-current (DC) potential, only ion with a specific m/z can have the stable trajectory and transmit through to the detector, while other ions will strike to the electrodes and be neutralized.

The ions traveled through the mass analyzer go to an electron multiplier detector to be fast converted to recordable signals. In the detector, the ion collided with the dynode generates multiple secondary electrons. After a series of collision, an avalanche of electrons produces from a single ion. As a result, a multiplication of the primary ion beam for a currant gain of about $10^5$ can be reached.

Two scan modes can be performed with the mass spectrometry: full-mass-range scanning, in which the all m/z value in the setting range is scanned to get the total-ion current (TIC) chromatogram; and selected-ion monitoring (SIM), in which the mass analyzer is set to sample the selected m/z values. The full scanning is used to identify the species; while the SIM mode is used for quantitative measurement since the sensitivity is enhanced due to the less sampling time on the undesired masses. Figure **4-5** (a) shows signal profile gathered from the weak flame with the full-mass-range scanning (m/z = 10 ~ 90), 2 peaks can be observed. The mass spectrum of each peak is given in Figure **4-5** (b-c). The similarity of each detected mass spectrum comparing to the data base is 96% for DME and 97% for Kr. When the SIM mode is used, spectrum 15, 29, 45 and 46 are selected for DME, and 82, 83, 84 and 86 are selected for Kr in this study.

### 4. 1. 4. Thermal Conductivity Detector

The operating principle of the thermal conductivity detector (TCD) is illustrated in Figure **4-6**. It is a bridge circuit with four TCD cells. When the sample flow through the detector, the voltage difference caused by the thermal conductivity changes is detected after amplification. [61]

The heat flow $Q$ from the wire filament to the TCD cell surface can be given as:

$$Q = G(T_1 - T_2)k \tag{4-4}$$

where $G$ is a geometry factor, $k$ is the thermal conductivity, $T_1$ and $T_2$ are the temperature for the filament and the cell surface respectively. In the meanwhile, the heat flow is provided by the applied electrical current on the wire filament, therefore, it can be also given by

$$Q = \frac{I^2 R_f}{J} \tag{4-5}$$

where $J$ is Joule's constant, $I$ is the applied electrical current on the filament, and $R_f$ is the resistance of the filament. The wire filament should have a resistance that is temperature-dependent

$$R_f = R_f^0(1 + aT_1) \tag{4-6}$$

where $a$ is the temperature coefficient, and $R_f^0$ is the resistance at a standard temperature.

Considering the heat balance in the TCD cells with the sample contained gas mixture (SR) and reference flow (R) respectively, it yields

$$T_{1,SR} - T_2 = \frac{I^2}{GJ}\frac{R_{f,SR}}{k_{SR}} \tag{4-7}$$

$$T_{1,R} - T_2 = \frac{I^2}{GJ}\frac{R_{f,R}}{k_R} \tag{4-8}$$

Subtracting Equation 4-8 from Equation 4-7 eliminates $T_2$:

$$T_{1,SR} - T_{1,R} = \frac{I^2}{GJ}\left(\frac{R_{f,SR}}{k_{SR}} - \frac{R_{f,R}}{k_R}\right) \tag{4-9}$$

Subtracting Equation 4-6 into Equation 4-9 to replace $T_{1,SR}$ and $T_{1,R}$ gives the relation as follow:

$$\Delta R = aR_f^0 \frac{I^2}{GJ}\left(\frac{\Delta R}{k_{SR}} + \frac{R_{f,R}}{k_{SR}} - \frac{R_{f,R}}{k_R}\right) \tag{4-10}$$

where $\Delta R$ equals to $R_{f,SR} - R_{f,R}$.

The thermal conductivity of the sample contained gas mixtures can be calculated from the thermal conductivity of the sample gas (S) and the reference gas (R) [63]

$$k_{SR} = \frac{k_S}{1 + C_1\dfrac{n_R}{n_S}} + \frac{k_R}{1 + C_2\dfrac{n_S}{n_R}} \tag{4-11}$$

where $C_1$ and $C_2$ are constants depending on the specific collision dynamics of sample and reference gas molecules, and $n_S$ and $n_R$ are the molecule number of the sample gas and reference gas in the TCD cells respectively. Since $n_S \ll n_R$ and $\Delta R \ll R_{f,R}$, the linear approximation for $\Delta R$ vs. $k_{SR}$ can be given as:

$$\Delta R = aR_f^0 \frac{I^2}{GJ}\frac{R_{f,R}}{k_R^2}\left(k_R - k_{SR}\right) \tag{4-12}$$

Therefore, the voltage difference obtained before the amplifier in this bridge circuit is

$$V_{diff} = \frac{\Delta R}{2R_{f,R} + \Delta R} U \tag{4-13}$$

where $U$ is the applied voltage on the circuit.

In this study, the filament current is set to be 90 mA, the cell temperature is 80 °C, and He acts as both reference flow and the carrier gas.

### 4. 1. 5. Concentration Calibration

A precise control of the injection volume is difficult with the manual sampling method. Also the entrainment of ambient air into the syringe cannot be fully eliminated. Therefore, the internal standard method is adopted for calibrating the species concentration. Another inert gas with a known concentration is added into the gas sample as the internal standard. The relation between concentrations of the internal standard and the target species can be expressed as

$$\frac{A_{IS}}{C_{IS}} = F \frac{A_X}{C_X}, \tag{4-14}$$

where $A$ is the peak area of the MS/TCD signal, $C$ is the concentration and $F$ is the response factor. Subscript "$IS$" and "$X$" stand for the internal standard and the target species, respectively. Prior to the above procedure, a standard gas (st) of the target species with a known concentration is mixed with the same internal standard gas in the same ratio, and their GC-MS/TCD signals are measured. Similarly, the relation between concentrations of the internal standard and the standard gas can be expressed as

$$\frac{A_{IS,st}}{C_{IS}} = F \frac{A_{X,st}}{C_{X,st}}. \tag{4-15}$$

Subtracting Equation 4-14 into Equation 4-15, the concentration of target species in the gas sample can be obtained as

$$C_X = C_{X,st} \frac{A_{IS,st}}{A_{X,st}} \frac{A_X}{A_{IS}}. \tag{4-16}$$

3.2 % of Kr is introduced into the gas sample as the internal standard in this study. The concentration is controlled by manipulating the flow rates of Kr and gases to be mixed via the mass flow controllers.

Figure **4-8** compares the measurement results with/without using the internal standard. A 4% DME standard gas was measured 7 times. The red dots show the peak

area of the DME for each measurement. Without the internal standard, the uncertainty in these 7 measurements is 4.49%. The black triangles show the peak area ratio between the DME and the Kr. It is shown that the uncertainty of these 7 measurements has been reduced to 0.685% by using the internal standard.

To obtain the absolute concentration, a standard gas of 4% CO in He is used for the calibration of the CO measurement, while DME is calibrated using the DME/air mixture with a controlled concentration.

### 4. 1. 6. Influence of Sampling Speed

As described before, a sampling speed of 20 µL/min is used in this study, which is less than 0.3% of the main flow. To confirm that the weak flame is not disturbed by such a low sampling speed, species distributions in the quartz channel at different sampling speeds are measured and compared. Sampling speeds of 5 and 20 µL/min are tested in the GC-MS measurement. For the TCD measurement, limited by the measurement time, a sampling speed of 10 µL/min is compared with 20 µL/min. As shown in Figure **4-9**, no obvious difference is observed in the species distribution when the sampling speed is changed. These results suggest that a sampling speed of 20 µL/min is low enough to prevent any disturbance to the weak flame.

## 4. 2. Surface Preparation

Quartz, SiC, SUS321, Inconel600, iron, nickel, chromium are chosen as wall surface materials in the investigation of the wall chemical effect on the streamwise species distributions in the weak flame. Quartz is the bulk wall material of the reactor. Thin films of alloys and metals are alternatively coated using the APD machine, as described in Section 3. 1. SiC is deposited using a sputtering system (Canon-Anelva, E-200S).

Sputtering is one of the physical vapor deposition (PVD) methods, which uses the plasma to erode the target and then neutral particles are ejected from the target to the substrate [64]. Unlike the arc plasma deposition (APD) that accepts metal target only, with a radio-frequency (RF) energy source, the target used in sputtering can be electrical insulating or semi-insulating materials such as the SiC [65]. A schematic diagram of the RF magnetron sputtering system is illustrated in Figure **4-10** [66]. The

magnets behind the cathode are used to trap the free electrons. When the argon atom enters the magnetic field and approach to the free electron, the outer shell electron of Ar is driven off, generating an $Ar^+$. The positively charged $Ar^+$ is accelerated by the electrical field to the cathode, which is the target material, and blasts the target surface to produce neutral particles ejecting to the substrate. In the meanwhile, free electron goes back to the argon, making it neutral again.

The deposition of SiC is operated at a chamber pressure of 1 Pa, and the power is set as 250 W. Thin film of ~ 150 nm is deposited in 30 min. As shown in Figure **4-11**, the arithmetic mean surface roughness, Ra, measured by AFM is 1.7 nm, which is considered as a surface smooth enough to neglect the effect of roughness on the reaction..


## 4. 3. Influence of Wall Materials on DME, CO and CO$_2$ distributions

### 4. 3. 1. Quartz, SiC, SUS321 and Inconel600

DME, CO and CO$_2$ mole fractions measured by the GC are shown in Figure **4-12**. The DME and CO mole fractions are calibrated, but not for the CO$_2$ mole fraction, thus the ratio between the peak area of CO$_2$ and Kr is directly used as a measure of the CO$_2$ mole fraction. At each position, three times of measurements are conducted, as shown by the marks in Figure **4-12**. The lines are the average values. Due to the characteristics of the separation column, the required measurement time of CO and CO$_2$ are much longer than that of DME. Due to the high concentration of Ni, the Inconel600 film coating cannot survive at the high temperature as the SUS321 one does. Therefore, the CO and CO$_2$ mole fractions in experiments of the Inconel600-coated channel are only available till $x = 30$ mm (1020 K).

It is shown that the consumption of DME starts at $x = 15$ mm (625 K) for all the quartz, SiC- and alloy-coated channels, and the DME concentration decreases to ~ 4% at $x = 20$ mm (720 K). The decreasing rate slows down in the quartz and the SiC-coated channels in between $x = 20$ and 25 mm (720 ~ 860 K), since the reaction enter into the NTC region. Instead of the decreasing in quartz and SiC-coated channels, the DME mole fraction at $x = 25$ mm (860 K) in alloy-coated channels remains the same level as that at $x = 20$ mm. The difference in the average value of measured DME between $x = 20$ mm and $x = 25$ mm are within 0.17% in both SUS321- and

Inconel600-coated channels. At $x = 30$ mm (1020 K), the DME mole fraction is almost zero in the quartz and the SiC-coated channels, but still remains a relatively high mole fraction of ~1.5% in the Inconel600-coated channel and ~2.2 % in the SUS321-coated channel. For all wall surface materials, DME vanishes after $x = 35$ mm (1150 K).

The CO mole fraction in the quartz and SiC-coated channels starts to increase at $x = 15$ mm (625 K), has the largest concentration at $x = 30$ mm (1030 K), and vanishes before $x = 40$ mm (1190 K). On the other hand, in the SUS321-coated channel, the increase of CO from $x = 15$ mm to $x = 20$ mm (720 K) is less than that in the quartz and SiC-coated channels. CO has the largest concentration at $x = 35$ mm (1150 K), and still remains a relatively high concentration at x = 40 mm (1179 K). Although the data for the Inconel600-coated channel is only available till $x = 30$ mm (1020 K), both the peak value and position of the CO mole fraction are in between these over the nonmetallic surfaces and the SUS321 surface.

As for the $CO_2$, the $CO_2$ mole fraction starts to increase after $x = 20$ mm (720 K) in both quartz and SiC-coated channel, but not until $x = 25$ mm (860 K) in the SUS321-coated channel. The $CO_2$ mole fraction distribution in the Inconel600-coated channel before $x = 30$ mm (1020 K) is almost the same as that of SUS321.

### 4. 3. 2. Iron, Nickel and Chromium

Iron and nickel film coatings are easier to be removed by the high temperature of the flame, if compared with SUS321 and Inconel. The film is quickly removed beyond $x = 30$ mm (1020 K). Since CO and $CO_2$ have relatively high concentration only after $x = 30$ mm (1020 K) and the required measurement time for CO and $CO_2$ is 5 times longer than that for DME, measurements of CO and $CO_2$ are omitted, and only DME mole fraction is measured in pure metal-coated channels.

Figure **4-13** (a) shows the measured DME mole fraction in the pure metal-coated channels. Three times of measurements are conducted at each position, as shown by the marks. The lines are the average values of the three times of measurements. For all channels, DME mole fraction at $x = 10$ mm (530 K) remains the same as that at the inlet. But earlier consumption of DME is observed in the Ni-coated channel than others. The consumption of DME at $x = 15$ mm (625 K) in the Fe- and Cr-coated channel is less than 7%. On the other hand, in the Ni-coated channel, 19% of DME is

already consumed till $x = 15$ mm (625 K). An obvious increase in DME mole fraction is observed in the Ni- and Fe-coated channels from $x = 20$ mm (720 K) to $x = 25$ mm (860 K). In order to clarify that this increase is not due to the uncertainty in these measurements, three additional measurements are conducted at each position. All measured results for $x = 20$ mm and 25 mm in the Ni- and Fe-coated channel are listed in Table **4-1**. The mole fraction measured at $x = 25$ mm is always higher than that at $x = 20$ mm for both channels, and the increments are one order higher than the uncertainties, which implies that DME is regenerated from $x = 20$ mm to 25 mm.

Table 4-1 DME mole fraction.

| | Fe, $x = 20$ mm | Fe, $x = 25$ mm | Ni, $x = 20$ mm | Ni, $x = 25$ mm |
|---|---|---|---|---|
| 1 | 0.03575 | 0.04193 | 0.03593 | 0.04257 |
| 2 | 0.03567 | 0.04134 | 0.03736 | 0.04138 |
| 3 | 0.03553 | 0.04258 | 0.03764 | 0.04315 |
| 4 | 0.03570 | 0.04291 | 0.03821 | 0.04123 |
| 5 | 0.03530 | 0.04214 | 0.03750 | 0.04173 |
| 6 | 0.03498 | 0.04196 | 0.03722 | 0.04134 |
| Avg. | 0.03549±0.00030 | 0.04214±0.00055 | 0.03731±0.00076 | 0.04190±0.00078 |

Figure **4-13** (b) compares measured DME mole fractions in the quartz, alloy- and pure metal-coated channels. Note that SUS321consists of 9~13% Ni, 17~19% Cr and ~ 70% Fe, while Inconel600 consists of 6~10% Fe, 14~17% Cr and over 72% Ni. Comparing with SUS321-coated channel, the DME mole fraction at $x = 15$ mm (625 K) in the Inconel-coated channel is slightly lower, which could be attributed to the high concentration of Ni. Among Fe, Ni and Cr, an obvious DME consumption at $x = 15$ mm is only observed in the Ni-coated channel. The DME regeneration in the alloy-coated channels from $x = 20$ mm (720 K) to $x = 25$ mm (860 K) is not as obvious as that in the Fe- and Ni-coated channels, which is probably caused by the Cr in the alloys. For the three pure metal-coated channels, only the Cr-coated channel has a decrease in the DME mole fraction from $x = 20$ mm (720 K) to $x = 25$ mm (860 K). At $x = 30$ mm (1020 K), among the three pure metal-coated channels, the Fe-coated channel has the highest DME mole fraction, which is also same as that found in the SUS321-coated channel. This could explain the higher DME mole fraction in the

SUS321-coated channel than the Inconel600-coated channel, because the iron concentration in SUS321 is higher than Inconel600. It should be noted that part of the metal films are probably oxidized already when wall temperature is raised. Without detailed examination of the surface before/after the combustion test, it is hard to tell whether Ni and Cr are oxidized or not because both nickel oxide and chromium oxide have no obvious color difference from the pure metal, but it is confirmed that Fe is oxidized partially at least. The color of the coated Fe film turns to red quickly when the wall temperate is high, as shown in Figure **4-14** (a), which indicates that the iron is oxidized into iron(III) oxide. Figure **4-14** (b) shows the coated Fe film after the test. After $x = 17$ mm, the iron film has already been oxidized. Therefore, the regeneration of DME could be the effect of either the metal or the metal oxide, or both. According to these data, it is conjectured that the roles of Fe, Ni and Cr in the alloys are as follows: Nickel is likely to cause an early consumption of DME below 625 K. Both Fe and Ni coatings contribute to the regeneration of DME, but the Fe coating is more active in generating DME, especially at high temperature. Although the surface compositions are not examined yet, it seems that metal oxides are formed. Thus, the influence of metal or alloy coatings on the weak flame could be caused by not only metals but also their metal oxides.

## 4. 4. Influence of Wall Materials on HCHO and OH distribution

Despite the fact that, as found in the methane/air normal flame experiments, SiC has a radical quenching effect that is larger than quartz and alumina, but smaller than SUS321 and Inconel600, streamwise species distributions in the quartz channel are only changed by SUS321 and Inconel600 coatings, but not the SiC coating. The change is more obvious in the SUS321-coated channel than the Inconel600-coated channel. Thus, the quartz and SUS321-coated channels are chosen for further investigation through HCHO-PLIF and OH-PLIF measurements. Measured 2-D OH and HCHO molar concentration of the DME/air weak flame ($U_{in}$ = 1.5 cm/s, $\phi$ = 0.85) in the quartz and SUS321-coated channels are shown in Figure **4-15**.

HCHO molar concentration along the centerline is plotted in Figure **4-16**. In the quartz channel, HCHO has a maximum concentration of $\sim 1.45 \times 10^{-4}$ kmol/m$^3$ at $x =$ 20 mm (730 K), then decreases rapidly, and vanishes completely before $x = 34$ mm (1130 K). On the other hand, in the SUS321-coated channel, although the HCHO

concentration peak value is less than 60% of that in the quartz channel, the HCHO extends to the higher temperature region, and remains in a relatively high concentration till $x = 33$ mm (1110 K). Even at $x = 38$ mm (1170 K), somehow HCHO still remains. To confirm the fluorescence signal beyond $x = 33$ mm is from HCHO but not other species such as the PAH, the emission spectrum of the weak flame at $x = 35$ mm in the SUS321-coated channel is compared with that of the HCHO/$H_2O$/$N_2$ mixture. As shown in Figure **4-17**, the two spectrums agree very well, indicating that the signal does come from the HCHO. This extended HCHO zone is probably caused by the remained DME beyond $x = 30$ mm.

Figure **4-18** shows the OH distribution along the channel centerline. The OH peak position is located at $x = 36$ mm (1160 K) in the quartz channel, but at $x = 40$ mm (1170 K) in the SUS321-coated channel. The OH peak shifts more downstream in the SUS321-coated channel than the quartz channel, which indicates that the hot flame ignition is delayed. The maximum OH intensity is higher in the SUS321-coatd channel, but the decreasing rate after the peak is larger than that in the quartz channel.

## 4. 5. Summary

Streamwise distributions of DME, CO and $CO_2$ in the weak flame are measured for the quartz, SiC-, SUS321- and Inconel600-coated channels by GC-MS and GC-TCD. Despite the relatively strong radical quenching effect of SiC in the normal flame, no significant change in the streamwise species distribution is observed over the SiC surface from that over quartz. But very unique distributions are observed in the alloy-coated channels. To understand the roles of each metal composition in the alloys, DME distributions in the Fe-, Ni- and Cr-coated channels are also measured. In addition, 2-D distributions of HCHO and OH are measured by PLIF system in the quartz and SUS321-coated channels.

In the SUS321-coated channel, higher concentration of DME and lower concentration of HCHO and CO are observed in the region of 870~1030 K than the concentrations in the quartz channel. The concentration of DME only decreases to its half at 1030 K in the SUS321-coated channel, but it is almost fully consumed in the quartz and SiC-coated channels. As a consequence, although the maximum concentrations are lower, the HCHO and CO zones extend to the higher temperature region in the SUS321-coated channel. The hot flame is affected by the remained low-

temperature oxidation products, resulting in its shifting downstream. The downstream shift of hot flame is also shown as a downstream-shifted OH peak and the late rising of CO in the SUS321-coated channel. Similar tendency is found in the Inconel600-coated channel. It is conjectured that, based on measured DME distribution in the pure metal-coated channels, Fe and Ni are the main causes of the DME regeneration in the alloys-coated channels.

These results are the first evidence showing that the wall chemical effect affects the low-temperature oxidation, resulting in the hot flame being changed. Unlike previous studies of the normal flame that the wall chemical effect affects only the species distribution in the near-wall region, species distributions in the streamwise direction are also changed by the wall chemical effect in the case of weak flame. Since the weak flame with separated flame zones in the streamwise distribution mimics the ignition process with temporal species evolution, these results suggest that the wall chemical effect may cause a thermal ignition delay through changing the low-temperature chemistry.
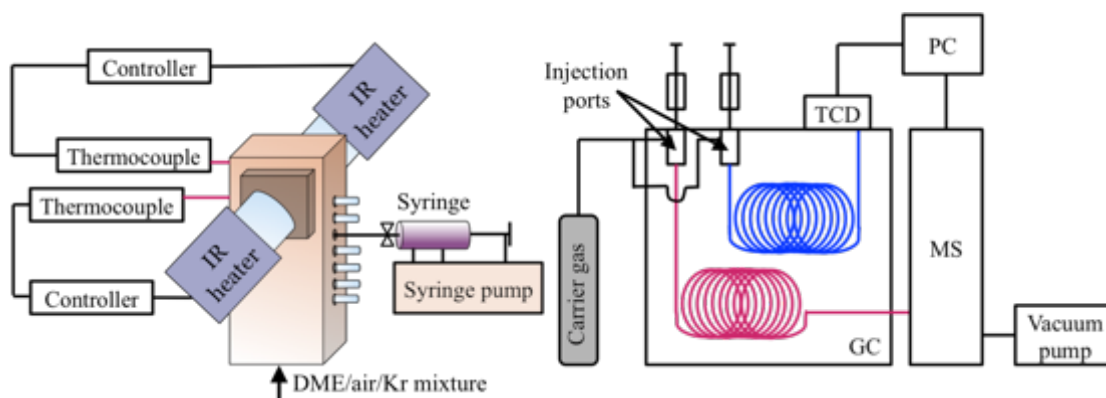
Figure 4-1 Schematic diagram of the GC analysis for the weak flame.
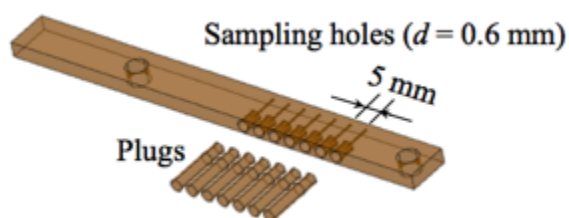


Figure 4-2 Sidewall with gas sampling holes.
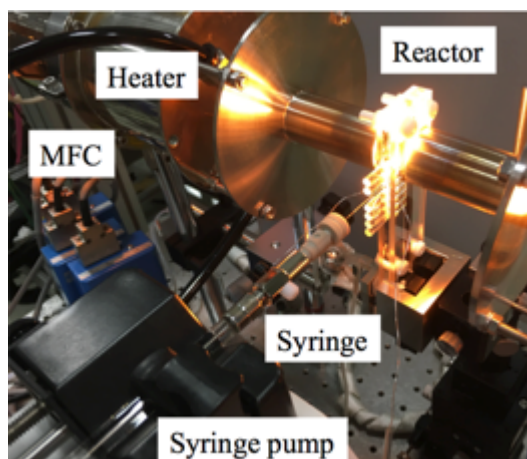


Figure 4-3 Photo of the gas sampling for weak flame.
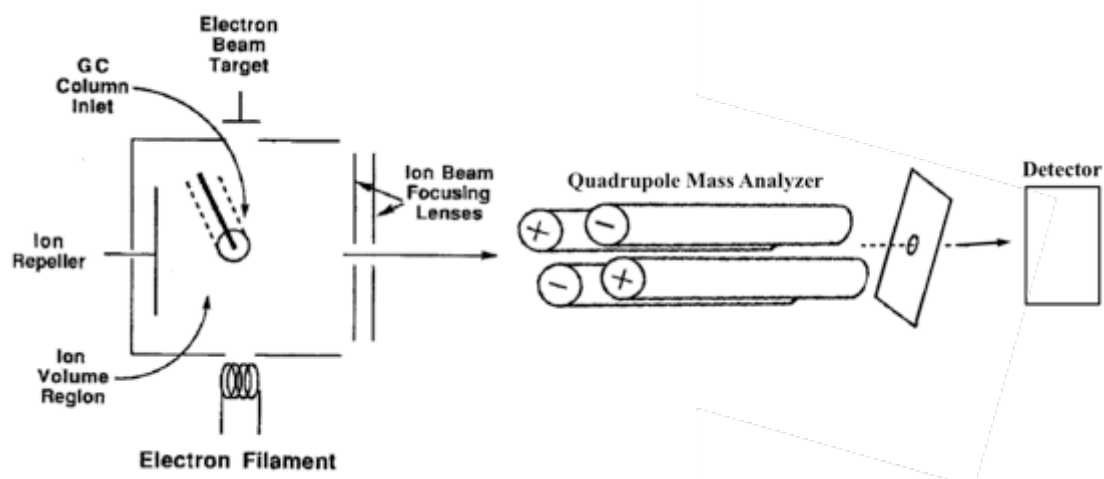
Figure 4-4 Schematic diagram of a mass spectrum system [61].
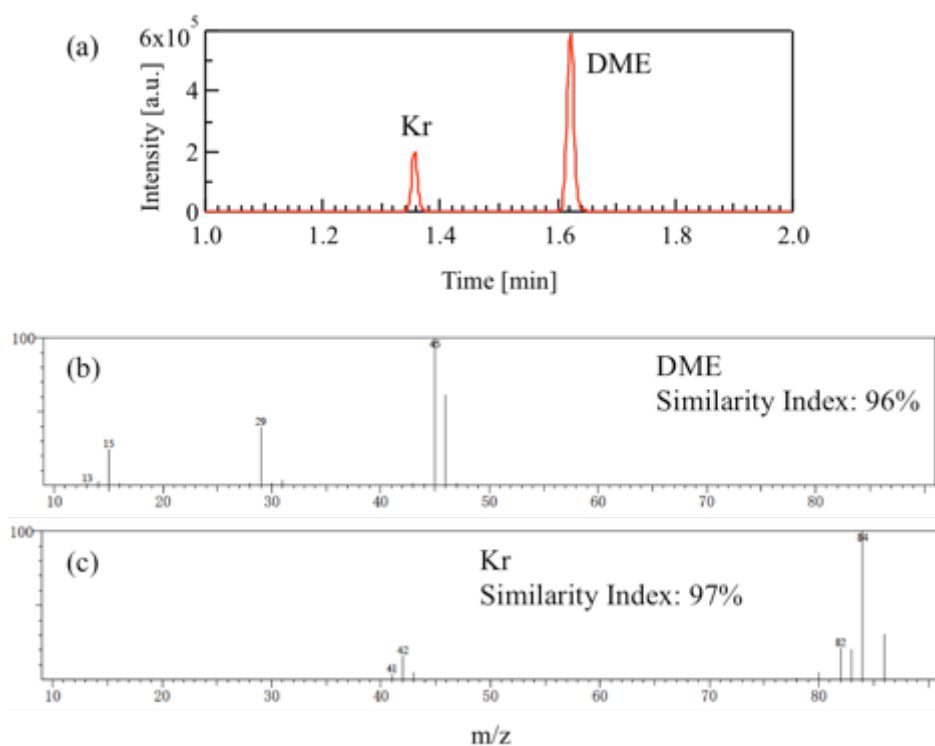


Figure 4-5 (a) GC-MS signal profile for a weak flame. And the mass spectrum for the detected (b) DME and (c) Kr.
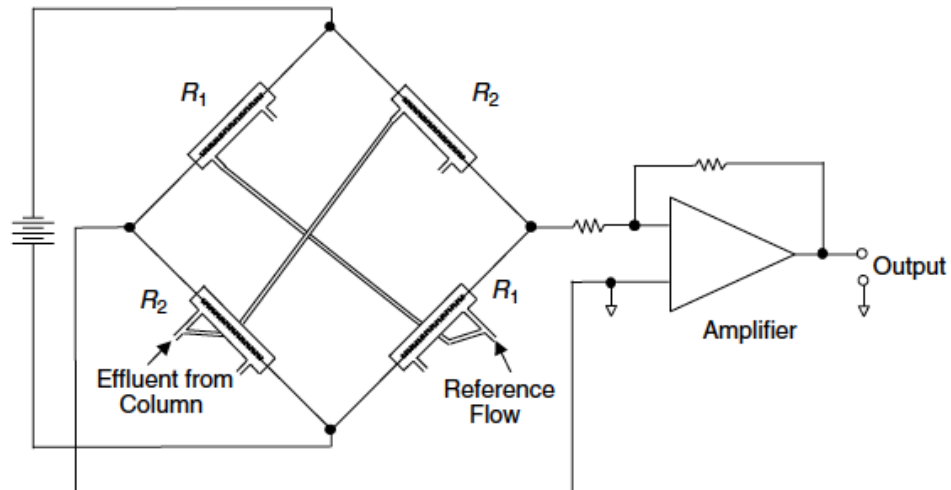
Figure 4-6 Schematic diagram of TCD [61].
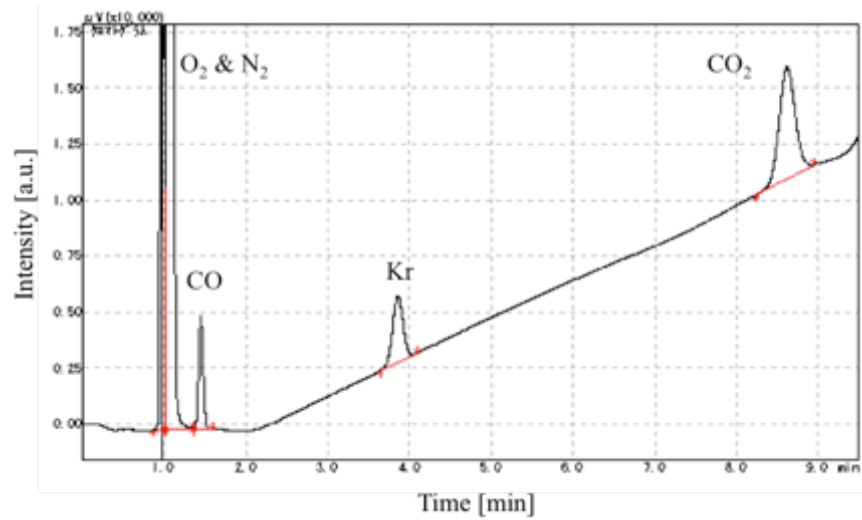


Figure 4-7 GC-TCD signal profile for a weak flame.
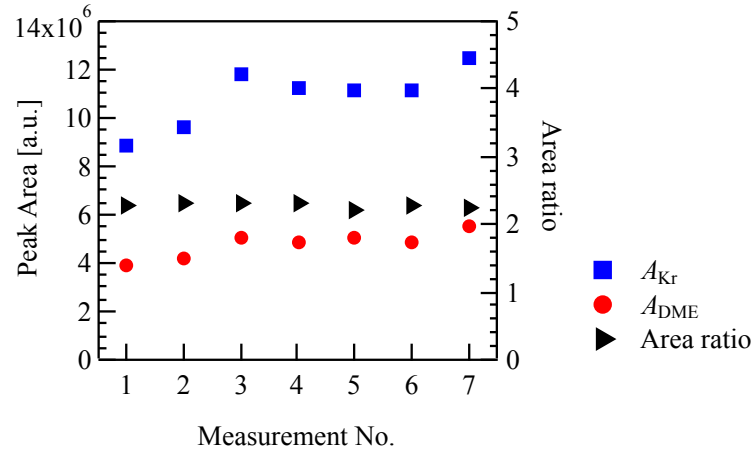
Figure 4-8 GC-MS measurement for a 4% DME standard gas.
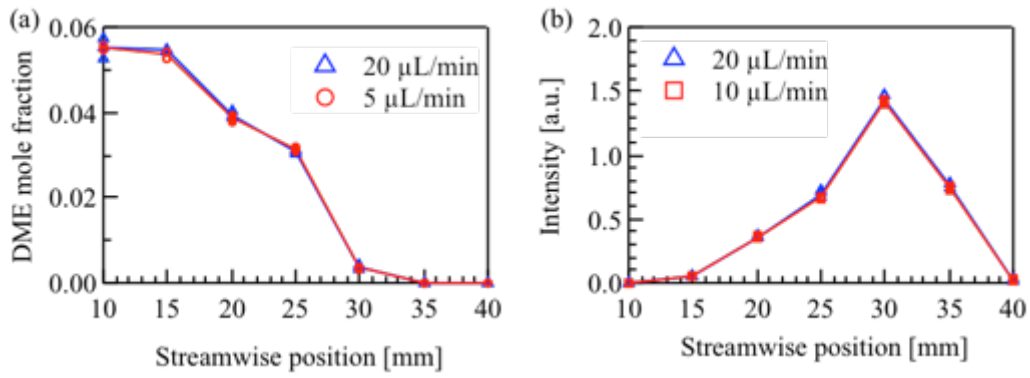


Figure 4-9 Measured species distributions with different gas sampling speeds. (a) DME, (b) CO in the quartz channel.
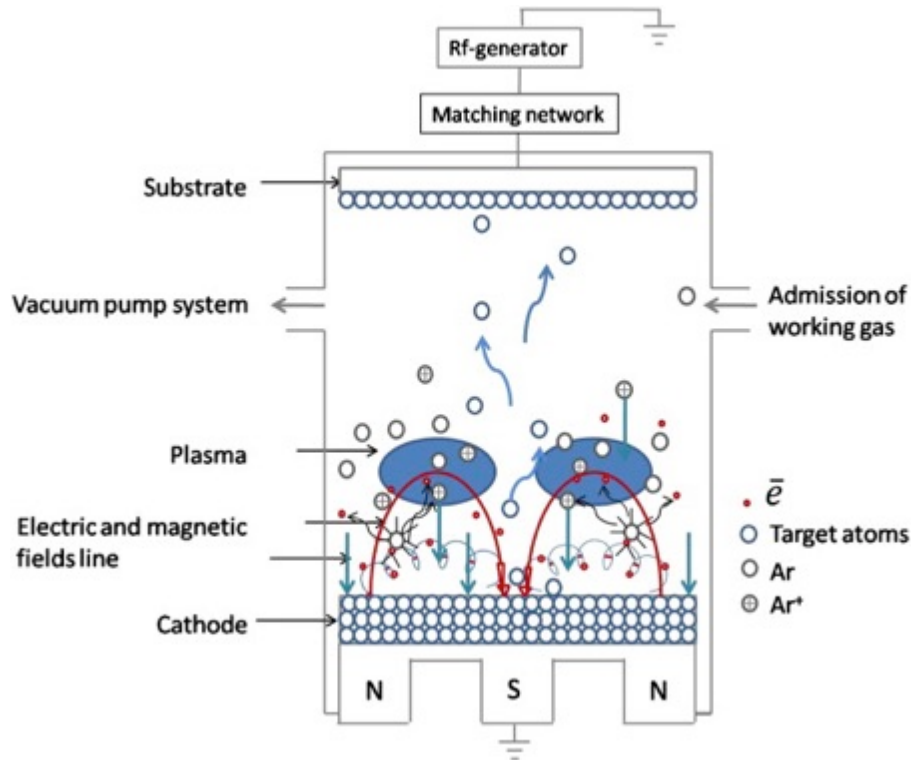
Figure 4-10 Schematic diagram of a RF magnetron sputtering system [66].
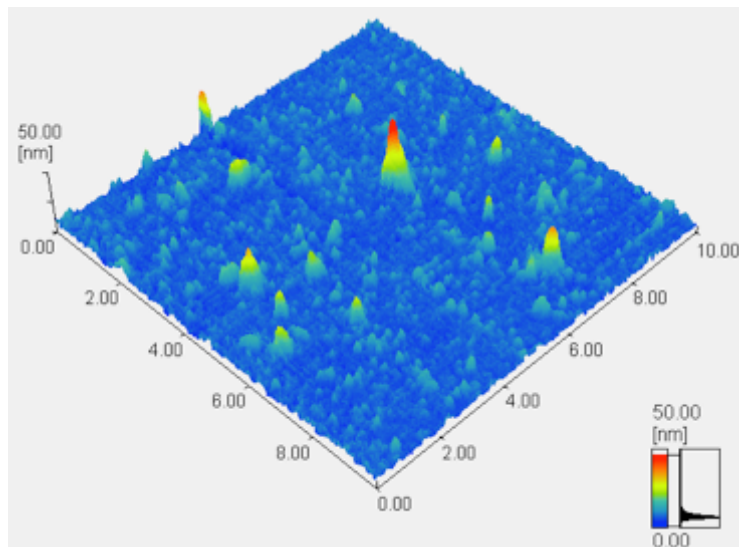


Figure 4-11 Surface roughness distribution of sputtered-SiC taken by AFM.
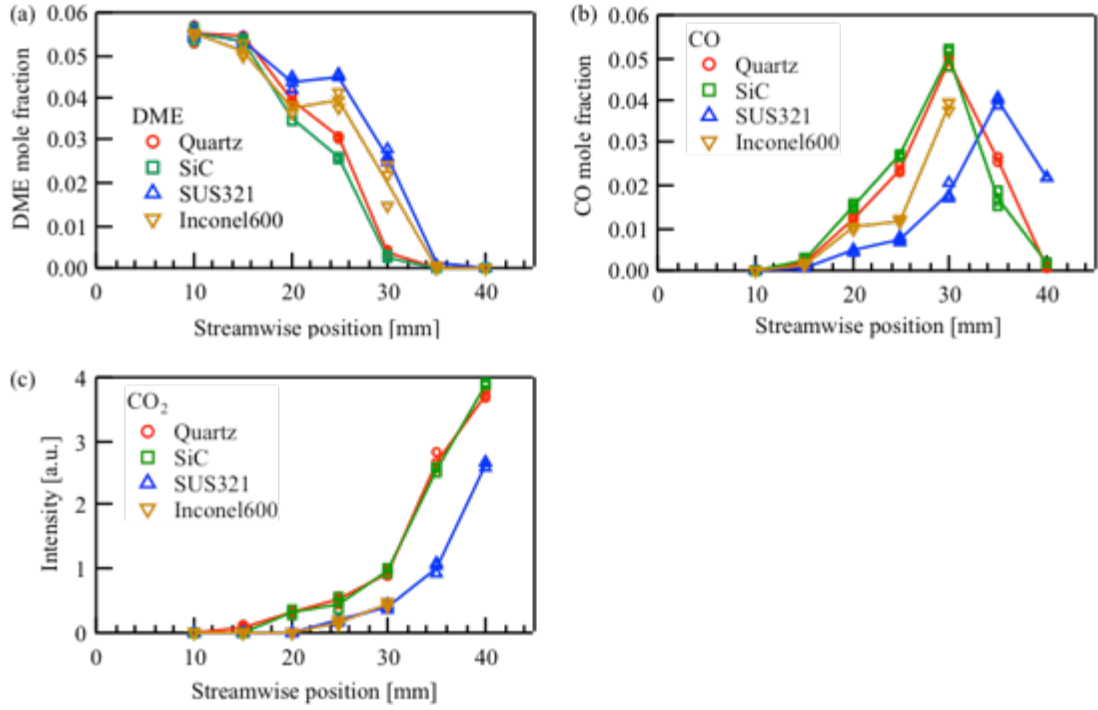
Figure 4-12 Streamwise distribution profiles of (a) DME, (b) CO and (c) CO2 for DME/air weak flames in quartz, SiC-, SUS321- and Inconel600-coated channel.
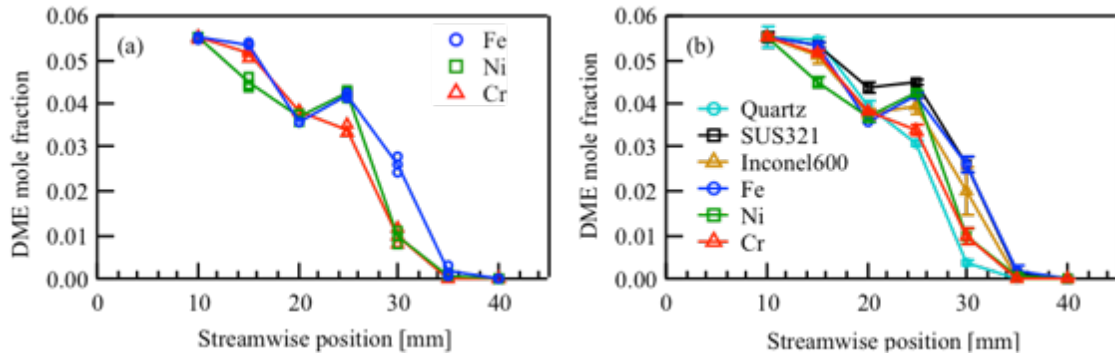


Figure 4-13 DME streamwise distribution in quartz, alloy- and metal-coated channel.
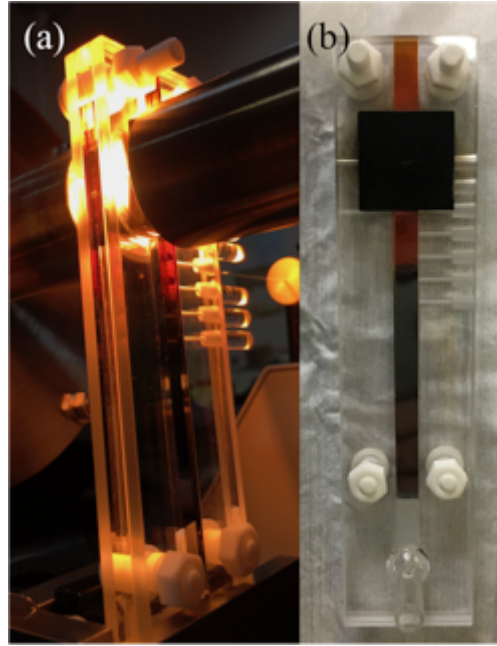
Figure 4-14 Fe-coated channel. (a) In experiment; (b) After experiment.
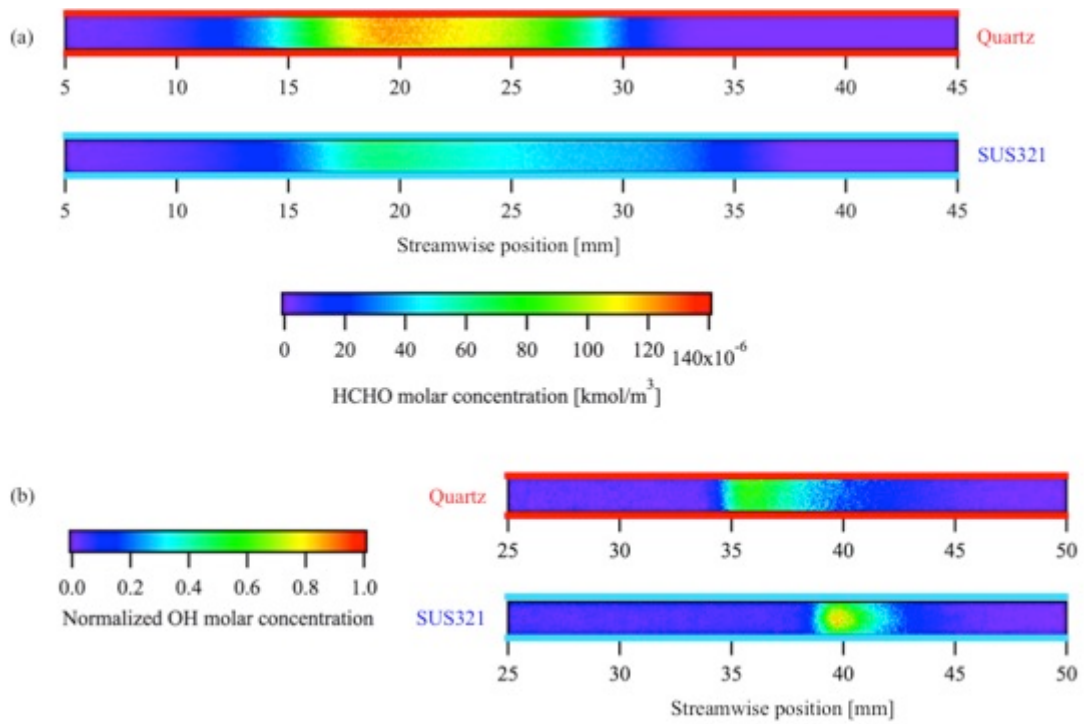


Figure 4-15 (a) HCHO and (b) OH distribution for DME/air weak flames (Uin = 1.5 cm/s, $\phi$ = 0.85) in quartz and SUS321-coated channel.
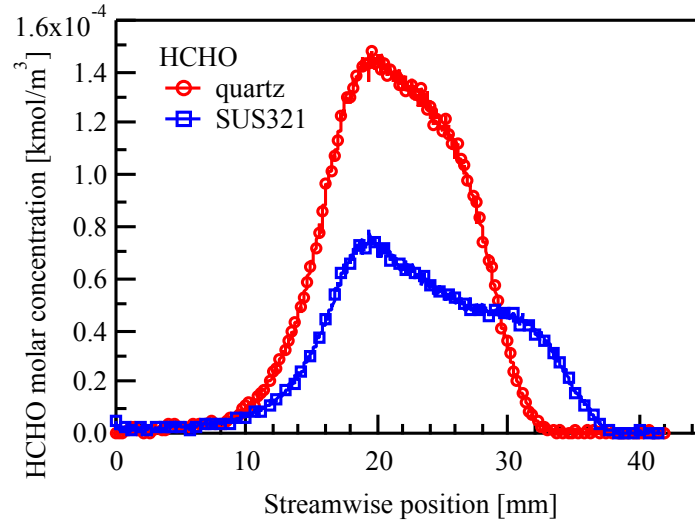
Figure 4-16 Streamwise distribution of HCHO along the centerline of the quartz and the SUS321-coated channel in a DME/air weak flame (Uin = 1.5 cm/s, $\phi$ = 0.85).
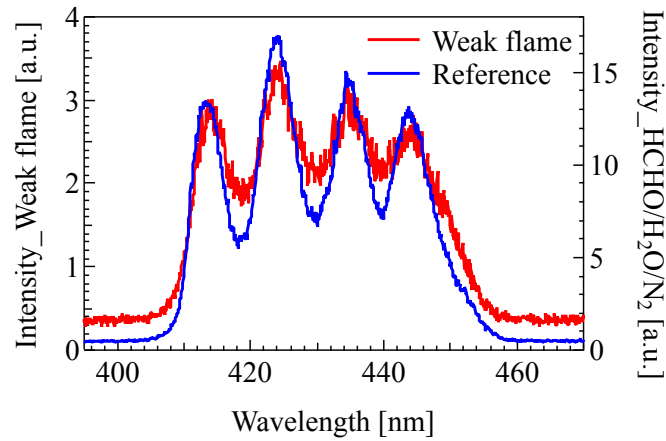


Figure 4-17 HCHO emission spectrum at x = 35 mm in the SUS321-coated channel. (430 nm band-pass filter, FWHM: 20 nm).
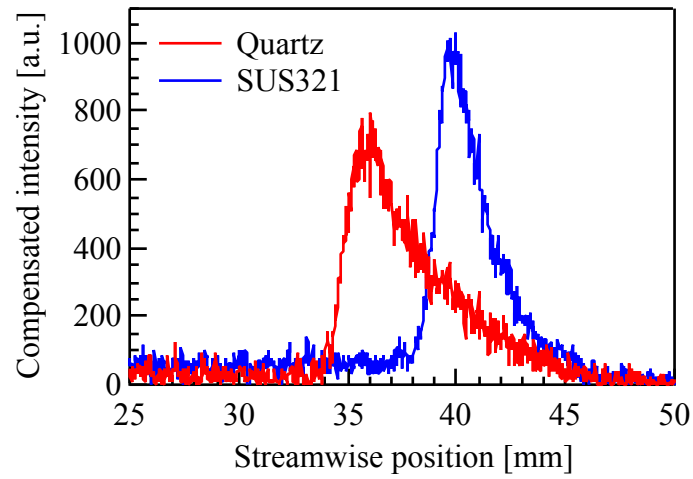
Figure 4-18 Streamwise distribution of OH along the centerline of the quartz and the SUS321-coated channel in a DME/air weak flame ($U_{in}$ = 1.5 cm/s, $\phi$ = 0.85).

# Chapter 5 Surface Reaction Model for Cool Flame

In Chap. 4, it was found that alloys and metals exert unique influence on the weak flame, comparing with quartz and SiC-coated channel. This chapter starts from the comparison between the experimental data in the quartz channel and the numerical simulation results of the inert channel. Then, in order to understand the surface reaction mechanism of SUS321, both the radical quenching model and catalytic model are examined. Hypotheses are proposed based on the experimental data and verified in numerical simulations. Finally, the proposed surface reaction model is applied in the wall-stabilized cool flame configuration, demonstrating that the wall chemical effect is important not only to the weak flame, but also to other combustion fields where the low-temperature oxidation matters.

## 5. 1. Two-dimensional Simulation

### 5. 1. 1. Simulation Method

Two-dimensional numerical simulation for DME/air weak flame ($\phi = 0.85$, $U_{in} = $ 1.5 cm/s) has been conducted in FLUENT 18.0 with detailed gas-phase and surface reactions. Same strategies used in Chap. 3 are adopted. However, since both sidewall chemical boundaries are same in this chapter, the computation domain is reduced to half of the channel due to the symmetry, as shown in Figure **5-1**. The number of grids is 300 in the streamwise direction and 12 in the wall-normal direction. Unequally-spaced grids are used in the wall-normal direction. The closest grid is at 12 μm from the wall.

### 5. 1. 2. Dependence on Gas-phase Reaction Mechanism

Measured species distributions in the quartz channel are compared with simulated results of the inert channel, as shown in Figure **5-2**. DME 2000 (79 species, 351 reactions) [21][22], CH₄/DME 2014 (113 species, 710 reactions) [26], Zhao et al.'s DME mechanism (55 species, 290 reactions) [68] and Kurimoto et al.'s DME mechanism (55 species, 290 reactions) [69] are employed to examine the mechanism dependence in the simulation of the weak flame. The CH₄/DME 2014 mechanism is a modified version of the DME 2000 mechanism, while the Kurimoto mechanism is

modified based on the Zhao mechanism. Generally speaking, the low-temperature oxidation in the $CH_4$/DME 2014 and Kurimoto mechanisms is weaker compared with that in the DME 2000 and Zhao mechanisms.

Compared with the DME 2000 and Zhao mechanisms, DME consumption in the low-temperature oxidation zone is much slower when either the $CH_4$/DME 2014 or the Kurimoto mechanism is used, yet the simulated DME consumption is still faster than that obtained in the experiment. As a result of the slow DME consumption, the CO concentration at $x = 15 \sim 25$ mm is also lower when either the $CH_4$/DME 2014 or the Kurimoto mechanism is used, which has better agreement with the experimental result than the other two mechanisms. No large difference in the $CO_2$ distribution is observed for these four mechanisms. The simulated $CO_2$ distribution agrees well with the measured one in the experiment. The absolute molar concentration of HCHO measured with HCHO-PLIF has a maximum of $\sim 1.5 \times 10^{-4}$ kmol/m$^3$ in the quartz channel. The simulated maximum value in the inert channel is $9.5 \times 10^{-5}$ kmol/m$^3$, $1.3 \times 10^{-4}$ kmol/m$^3$, $1.7 \times 10^{-4}$ kmol/m$^3$ and $2.4 \times 10^{-4}$ kmol/m$^3$ when the Zhao mechanism, DME 2000, Kurimoto mechanism and $CH_4$/DME 2014 are used, respectively. The HCHO concentration predicted by the $CH_4$/DME 2014 and Kurimoto mechanism is higher than the measured one, which indicates a weakened low-temperature oxidation. Simulated OH distributions by the DME 2000 and Zhao mechanism are in coincident with each other. With $CH_4$/DME 2014, the OH peak shifts to downstream and has a higher peak value. Simulated OH distribution by the Kurimoto mechanism lays in between. Since the absolute concentration of OH is not measured in this study, only the peak position is compared. With $CH_4$/DME 2014, the OH peak position is closer to the measured one, but still 2 mm upstream.

On the whole, the streamwise species distribution measured in the quartz channel is well predicted, especially when either $CH_4$/DME 2014 or Kurimoto mechanism is used. Due to the uncertainty coming from the gas-phase reaction mechanism, it is difficult to conclude that quartz is completely inert or not for the weak flame, but it is still reasonable to consider that surface reactions over quartz have only very limited chemical effect on the weak flame. As a simplification, quartz is treated as an inert material in the following discussion.

Note that DME2000 is used as the gas-phase reaction mechanism for examining the radical quenching model, while $CH_4$/DME 2014 is used in the 2-D simulation for

examining the newly-proposed surface reaction model with the DME synthesis hypothesis.

### 5. 1. 3. Influence of Additional Inert Gas

In the PLIF measurement, DME/air gas mixture with an equivalence ratio of 0.85 is employed. On the other hand, in the GC measurement, since internal standard method is used, additional inert gas, Kr, is added into the gas mixture. Mass flow rates of DME and air are adjusted to keep the same equivalence ratio ($\phi = 0.85$) and the same mean inlet flow velocity ($U_{in} = 1.5$ cm/s). The mole fraction and mass flow rate for each composition in PLIF and GC measurements are listed in Table **5-1**.

Table 5-1 Mole fraction and mass flow rate for each composition.

|  | DME | Air | Kr |
|---|---|---|---|
| PLIF | 5.60%, 0.378sccm | 94.40%, 6.372 sccm | - |
| GC | 5.42%, 0.366 sccm | 91.39%, 6.169 sccm | 3.19%, 0.215 sccm |

The influence of the additional Kr is examined with the numerical simulation. $CH_4$/DME 2014 is used as the gas-phase reaction mechanism. Since the Kr is not included in the mechanism, the data of Ar is used actually. Figure **5-3** compares the simulated results with and without Kr, and the GC results in the quartz channel are also plotted. Generally speaking, no obvious difference is observed in DME, CO and $CO_2$ distributions with or without Kr. A slightly higher CO concentration is observed when Kr is included. To simplify the comparison, in the following discussion, the influence of the additional inert gas is omitted. All simulations are conducted without considering the additional Kr.

## 5. 2. Reaction Pathway Analysis

To search possible reaction paths accounting for the high DME concentration observed in alloy- and metal-coated channels, a reaction pathway analysis of the gas-phase reaction in the weak flame is conducted with DETCHEM.

### 5. 2. 1. Simulation Method

DETCHEM [67] is a software package developed by O. Deutschmann et al. for the modeling of gaseous reactive flows including reactions on solid surfaces using elementary-step like reaction mechanisms as well as global reaction mechanisms. DETCHEM consists of several basic models that can be used for different applications. In this study, DETCHEM Batch is adopted. It is a tool that simulates the temporal variations of temperature and concentrations of species in an ideal batch reactor where both homogeneous gas-phase and heterogeneous surface chemical reactions occur [67]. For a batch reactor with a known temperature, the governing equations only contains [67]:

$$\frac{dn_k}{dt} = V\dot{\omega}_k + A\dot{s}_k \qquad \text{gas-phase species} \qquad (5\text{-}1)$$

$$\frac{dn_k}{dt} = \alpha A\dot{s}_k \qquad \text{surface species} \qquad (5\text{-}2)$$

$$pV = nRT \qquad \text{ideal gas equation} \qquad (5\text{-}3)$$

where $n_k$, $\dot{\omega}_k$, $\dot{s}_k$, $V$, $A$, $\alpha$ represent the species concentration in unit of mole numbers, the gas-phase reaction rate, surface reaction rate, reactor volume, catalytic surface area and surface relaxation factor respectively.

As illustrated in Figure **5-4**, the steady-state simulation in the 1-D channel can be transformed to a transient simulation of a constant reactive flow in the batch reactor with a given temporal temperature development. According to FLUENT 2-D simulation results, the pressure drop along the channel is less than 0.4 Pa, thus, a constant pressure condition is employed in the batch reactor. Figure **5-5** (a) shows the temperature and velocity profiles in the FLUENT 2-D channel simulation. A temporal temperature development shown in Figure **5-5** (b) is applied. The data required by the DETCHEM Batch input files are listed in Table **5-2**. Since no species transport, energy balance or any flow field need to be calculated in DETCHEM Batch, the simulation can be done within a few minutes, whereas the 2-D simulation with FLUENT needs several days with same reaction mechanisms. DETCHEM can list the species consumption or generation rate for all reactions, thus a reaction pathway analysis can be conducted for any certain moment during the temperature development.

Table 5-2 Input data for DETCHEM Batch.

| | |
|---|---|
| Mechanism files | Gas-phase & Surface |
| Catalytic surface area | 1.3E-5 m$^2$ |
| Initial volume | 7.5E-9 m$^3$ |
| Pressure | 1.013E5 Pa |
| Initial mole fractions | $CH_3OCH_3$: 0.05601215 |
| | $O_2$: 0.19769 |
| | $CO_2$: 0.00378 |
| | $N_2$: 0.74251785 |
| Initial surface coverage | B(s): 1 |
| Integration time | 0.93 s |
| Temperature profile | $T$(t) |
| Initial step size | 1E-10 |
| Absolute tolerance | 1E-16 |
| Relative tolerance | 1E-6 |

**5. 2. 2. Verification of the Zero-dimensional Simulation**

Figure **5-6** plotted the species profiles in an inert channel simulated by DETCHEM Batch and FLUENT. For the comparison, temperature is used for the abscissa. Very sharp increase and decrease in concentration are observed from the results of DETCHEM. This is because the streamwise species diffusion in the channel is not considered in the batch reactor. Nevertheless, the main features of the weak flame are well captured by DETCHEM, and the concentrations of intermediate species are also in similar level. The two-stage oxidation of DME is captured in both simulations. The DME consumption slows down at 650 K, and vanishes before 1000 K. CO and HCHO mostly exist in the temperature range of 650~1000 K in both simulations, while the OH peak locates at ~1100 K. The generation of $CO_2$ starts after the low-temperature oxidation of DME, and increases rapidly in the hot flame zone. This comparison suggests that the 0-D DETCHEM Batch model is appropriate for the reaction pathway analysis of the weak flame.

### 5. 2. 3. Reaction Pathway Analysis for Gas-phase Reaction

Table **5-3** listed all the reactions consumes DME in the CH$_4$/DME 2014 and DME 2000 mechanisms. The consumption of DME is through either the H abstraction or the $\beta$-scission.

Table 5-3 DME consumption reactions.

| No. in CH$_4$/DME2014 | No. in DME2000 | Reaction |
|---|---|---|
| R432 | R273 | CH$_3$OCH$_3$ (+M) <=> CH$_3$ + CH$_3$O (+M) |
| R433 | R274 | CH$_3$OCH$_3$ + OH <=> CH$_3$OCH$_2$ + H$_2$O |
| R434 | R275 | CH$_3$OCH$_3$ + H <=> CH$_3$OCH$_2$ + H$_2$ |
| R435 | R276 | CH$_3$OCH$_3$ + O <=> CH$_3$OCH$_2$ + OH |
| R436 | R277 | CH$_3$OCH$_3$ + HO$_2$ <=> CH$_3$OCH$_2$ + H$_2$O$_2$ |
| R437 | R278 | CH$_3$OCH$_3$ + CH$_3$O$_2$ <=> CH$_3$OCH$_2$ + CH$_3$O$_2$H |
| R438 | R280 | CH$_3$OCH$_3$ + O$_2$ <=> CH$_3$OCH$_2$ + HO$_2$ |
| R439 | R279 | CH$_3$OCH$_3$ + CH$_3$ <=> CH$_3$OCH$_2$ + CH$_4$ |
| R440 | R281 | CH$_3$OCH$_3$ + CH3O <=> CH$_3$OCH$_2$ + CH$_3$OH |
| R441 | R288 | CH$_3$OCH$_3$ + CH$_3$OCH$_2$O$_2$ <=> CH$_3$OCH$_2$ + CH$_3$OCH$_2$O$_2$H |
| R442 | R302 | CH$_3$OCH$_3$ + O$_2$CHO <=> CH$_3$OCH$_2$ + HO$_2$CHO |
| R443 | R328 | CH$_3$OCH$_3$ + OCHO <=> CH$_3$OCH$_2$ + HOCHO |
| R454 | R283 | CH$_3$OCH$_2$ + CH$_3$O <=> CH$_3$OCH$_3$ + CH$_2$O |
| R455 | R284 | CH$_3$OCH$_2$ + CH$_2$O <=> CH$_3$OCH$_3$ + HCO |
| R456 | R285 | CH$_3$OCH$_2$ + CH$_3$CHO <=> CH$_3$OCH$_3$ + CH$_3$CO |

A reaction pathway analysis is conducted with DETCHEM at t = 0.6 s (770 K) for the gas-phase reactions. As shown in Figure **5-7**, in the low temperature region, DME cannot directly go to the $\beta$-scission, but goes through the H abstraction to form the methoxymethyl radical (CH$_3$OCH$_2$) instead. CH$_3$OCH$_2$ can directly go to the $\beta$-scission, releasing HCHO and CH$_3$, or produce methoxymethyl-peroxy radical, CH$_3$OCH$_2$O$_2$ with adding O$_2$. The formed CH$_3$OCH$_2$O$_2$ goes through the isomerization and then have the $\beta$-scission to form HCHO. HCHO dehydrogenates to HCO and further goes through the path HCO $\rightarrow$ CO $\rightarrow$ CO$_2$. It should be noted that

78.3% of H atom abstraction of DME occurs through the reaction with OH and H, and in the meanwhile 59.9% of the HCHO dehydrogenation also occurs through the reaction with OH and H. In other words, DME and HCHO is competing for OH and H. As such, when HCHO is formed, the reaction enters the negative temperature coefficient (NTC) region of the DME oxidation.

If the high DME concentration in the alloy- and metal-coated channel is caused by changes in the gas-phase reactions, possibilities are: (1) H and OH destruction over the surface and (2) high HCHO concentration. According to the experimental results, HCHO concentration observed in the SUS321-coated channel is lower than that in the quartz channel. Therefore, the possibility left is the destruction of H and OH.

## 5. 3. Weak Flame in SUS321-coated Channel

In the experiment, an increase of DME concentration is observed in the SUS321-coated channel. There are two possibilities accounting for such a DME increase: a slowing down of the DME consumption in the gas-phase or a DME synthesis over the surface. As discussed in the reaction pathway analysis, DME is consumed through the H atom abstraction at the low temperature. 79.4% of the DME consumption occurs with OH, H, O and $CH_3$. Theoretically, if these four radicals are destructed by the surface, the consumption of DME will be slowed down. No other reaction can significantly change the DME consumption rate. The synthesis of DME is also a possible explanation. DME synthesis through CO, $CO_2$ and $H_2$ adsorption has been widely studies in catalytic reactions. The two possibilities for the increase in DME concentration will be further discussed later.

### 5. 3. 1. Radical Quenching Model

Radical quenching model listed in Table **3-1** was used in previous studies of the wall chemical effect on the methane normal flame [16][17][56][57]. In Chap. 3, the initial sticking coefficients for quartz and SUS321 in the weak flame are estimated as 0.0015 and 0.006, respectively.

Fluent 2-D simulation results with the initial sticking coefficient of unity are compared with results in the inert channel, as shown in Figure **5-8**. The profiles are the species distribution along the centerline of the channel. It is shown that, except

OH, the streamwise distributions of DME, CO, $CO_2$ and HCHO have no obvious change even though the initial sticking coefficient is tuned from 0 to 1. The downstream shift in the OH peak position is less than 1 mm. Apparently, the radical quenching model is failed to describe the wall chemical effect on the weak flame.

This is because that, in the cool flame, OH, H, O and $CH_3$ are consumed as soon as they are generated, which leads to extremely low concentrations of them. OH, H, O and $CH_3$ generated in the gas-phase do not have any chance to diffuse to the surface to be destructed. As such, no obvious change in DME concentration can be observed when the radical quenching model is applied. Since the DME consumption rate is not likely to be influenced by the surface reactions, the possibility left is the DME synthesis through surface reactions.

### 5. 3. 2. DME Synthesis

DME synthesis from $CO/CO_2$ and $H_2$ over some bifunctional catalysts has been widely studied [70][71][72][73][74][75]. Two consecutive reactions shown in Figure **5-9** are included: (1) the methanol synthesis in which CO, $CO_2$ and $H_2$ are adsorbed onto the surface to form methanol, (2) the methanol dehydration in which methanol adsorbed on the surface acid site forms DME. Besides Fe, SUS321 contains 9~13% Ni and 17~19% Cr. Ni has been reported as the catalyst for methanol synthesis [76][77][78], while great promoting effect of Cr in the methanol synthesis has been reported [79][80]. Fe has been reported to be a very active catalysis for the Fischer-Tropsch synthesis (hydrocarbons and alcohols are from CO/CO2 and $H_2$), in which methanol is one of the side products [81][82][83][84][85]. On the other hand, oxidized metal surfaces can provide surface acid sites. Therefore, it is reasonable to include the DME synthesis reaction pathway into the SUS321 surface reaction model.

To date, no surface reaction mechanism for the stainless steel has been published. Since SUS321 contains 9~13% Ni whose surface reaction mechanism has been intensely studied [76][86][87][88][89], the surface reaction model for SUS321 is built based on the reaction rate data for Ni. The reaction mechanism proposed in this study is listed in Table **5-4**. To simplify the reaction mechanism, the $CO_2$ hydrogenation path is not included, because major $CO_2$ is formed after the consumption of DME in the weak flame. In the current mechanism, the metallic site and the acid site are not marked as two different types of empty site. Because it is necessary to distinguish the

CH$_3$O on the two different sites, CH$_3$O on the metallic site is marked as CH$_3$O(s) while CH$_3$O on the acid site is marked as CH$_3$O(a). For the interaction of H$_2$, O$_2$ and CO with SUS321, the reaction rate data from the CH$_4$ reforming and oxidation over Ni [86] is adopted with weakening the adsorption of H$_2$ in this study, because it was found that a strong H$_2$ adsorption changes the gas-phase reactivity significantly and leads to a hot flame ignition over the surface, which was not observed in the experiment. Therefore, the initial sticking coefficient of H$_2$ is reduced to 0.0001. The sticking coefficient of CO was obtained by matching the simulated result with the measured one. The activation energy for the HCO hydrogenation reactions to CH$_3$OH are taken from I.N. Remediakis's DFT study on Ni(111) [76]. For the reactions of DME synthesis from CH$_3$OH, the activation energy is simplified to 0, which means that these reactions are not considered as the rate-limiting steps. The values of pre-exponential factor are estimated with the transition state theory as described in Chap. 3. A value of $3.7 \times 10^{21}$ cm$^2$mol$^{-1}$s$^{-1}$ is used for the bimolecular reactions and a value of $1 \times 10^{13}$ s$^{-1}$ is used for molecular desorption. The adsorption rate of CH$_3$OH is obtained through the data fitting. The channel simulated with the surface reaction mechanism described above is referred as the active_1 channel.

Table 5-4 DME synthesis mechanism over SUS321 for weak flame.

| Reaction | A (cm, mol, s) or $S_0$ | Ea (kJ/mol) | Source |
|---|---|---|---|
| 1. H$_2$ + 2B(s) => 2H(s) | 1.000E-04 | - | est, this work |
| 2. 2H(s) => 2B(s) + H$_2$ | 5.593E+07 | 88.12 | Ref. [86] A*10$^{-12}$ |
| 3. O$_2$ + 2B(s) => 2O(s) | 1.000E-02 | - | Ref. [86] |
| 4. 2O(s) => 2B(s) + O$_2$ | 2.500E+23 | 470.39 | Ref. [86] |
| 5. H$_2$O + B(s) => H$_2$O(s) | 1.000E-01 | - | Ref. [86] |
| 6. H$_2$O(s) => B(s) + H$_2$O | 4.579E+12 | 62.60 | Ref. [86] |
| 7. CO$_2$ + B(s) => CO$_2$(s) | 1.000E-05 | - | Ref. [86] |
| 8. CO$_2$(s) => B(s) + CO$_2$ | 9.334E+07 | 28.80 | Ref. [86] |
| 9. CO + B(s) => CO(s) | 0 ~ 1 | - | fit, this work |
| 10. CO(s) => B(s) + CO | 4.041E+11 $\varepsilon_{CO(s)}$ | 112.85 -50 | Ref. [86] |

| | | | |
|---|---|---|---|
| 11. $O(s) + H(s) => OH(s) + B(s)$ | 5.000E+22 | 97.90 | Ref. [86] |
| 12. $OH(s) + B(s) => O(s) + H(s)$ | 2.005E+21 | 37.19 | Ref. [86] |
| 13. $OH(s) + H(s) => H_2O(s) + B(s)$ | 3.000E+20 | 42.70 | Ref. [86] |
| 14. $H_2O(s) + B(s) => OH(s) + H(s)$ | 2.175E+21 | 91.36 | Ref. [86] |
| 15. $2OH(s) => H_2O(s) + O(s)$ | 3.000E+21 | 100.00 | Ref. [86] |
| 16. $H_2O(s) + O(s) => 2OH(s)$ | 5.423E+23 | 209.37 | Ref. [86] |
| 17. $CO(s) + B(s) => C(s) + O(s)$ | 5.200E+23 | 148.10 | Ref. [86] |
| 18. $C(s) + O(s) => CO(s) + B(s)$ | 1.418E+22 | 115.97 | Ref. [86] |
| | $\varepsilon_{CO(s)}$ | -50 | |
| | $n$ | -3 | |
| 19. $CO(s) + O(s) => CO_2(s) + B(s)$ | 2.000E+19 | 123.60 | Ref. [86] |
| | $\varepsilon_{CO(s)}$ | -50 | |
| 20. $CO_2(s) + B(s) => CO(s) + O(s)$ | 3.214E+23 | 86.50 | Ref. [86] |
| | $n$ | -1 | |
| 21. $CO(s) + H(s) => HCO(s) + B(s)$ | 2.338E+20 | 127.98 | Ref. [86] |
| | $n$ | -1 | |
| 22. $HCO(s) + H(s) => CH_2O(s) + B(s)$ | 3.700E+21 | 77.88 | Ref. [76] |
| 23. $CH_2O(s) + H(s) => CH_3O(s) + B(s)$ | 3.700E+21 | 40.38 | Ref. [76] |
| 24. $CH_3O(s) + H(s) => CH_3OH + 2B(s)$ | 3.700E+21 | 58.65 | Ref. [76] |
| 25. $CH_3O(s) => B(s) + CH_3O$ | 1.000E+07 | 178.85 | Ref. [76] |
| 26. $CH_3OH + B(s) => CH_3OH(a)$ | $0 \sim 1$ | - | fit, this work |
| 27. $CH_3OH(a) => B(s) + CH_3OH$ | 1.000E+07 | 0.00 | est, this work |
| 28. $CH_3OH(a) + O(s) => CH_3O(a) + OH(s)$ | 3.700E+21 | 0.00 | est, this work |
| 29. $CH_3OH(a) + CH_3O(a) => CH_3OCH_3 + OH(s) + B(s)$ | 3.700E+21 | 0.00 | est, this work |
| 30. $2CH_3O(a) => CH_3OCH_3 + O(s) + B(s)$ | 3.700E+21 | 0.00 | est, this work |

Figure **5-10** compares computed species distribution along the centerline with and without applying the DME synthesis mechanism. The experimental data is also plotted. The sticking coefficients of CO and $CH_3OH$ in this case are set as 0.3 and 0.05, respectively. Comparing with the simulation results in the inert channel, higher DME concentration in the NTC zone and the delay of the hot flame is observed in the active_1 channel. It is shown that all the DME, CO, $CO_2$ and OH distributions are similar as those measured in the experiment of SUS321-coated channel. However,

instead of a decrease in HCHO concentration, which is observed in the experiment, an increase in HCHO concentration is obtained using the DME synthesis mechanism. Therefore, additional modification is necessary for this surface reaction model.

### 5. 3. 3. HCHO adsorption

In order to predict the same lowered HCHO concentration observed in the SUS321-coated channel, adsorption of HCHO is added into the DME synthesis mechanism. The two additional reactions and their kinetic data are listed in Table **5-5**. The sticking coefficient of HCHO is obtained through fitting the simulated HCHO profile to the measured one, which is described later.

Table 5-5 Additional reactions for HCHO adsorption

| Reaction | A (cm, mol, s) or $S_0$ | Ea (kJ/mol) | Source |
|---|---|---|---|
| 31. $CH_2O + B(s) => CH_2O(s)$ | $0 \sim 1$ | - | fit, this work |
| 32. $CH_2O(s) => B(s) + CH_2O$ | 1.000+07 | 13.46 | Ref. [76] |

After adding the two additional reactions, the simulation of the weak flame over SUS321 is conducted again. The case with the modified surface reaction mechanism is referred as the active_2 channel in the following discussion. Same sticking coefficients of CO and $CH_3OH$ are used and the sticking coefficient of HCHO is set as 0.0005 in this case. Simulated species profiles along the centerline in the active_2 channel are plotted in Figure **5-11** in comparison with that in the inert channel and the experimental data. Similarly as in the active_1 channel, both an increase in DME concentration and the delay of the hot flame are well reproduced in the active_2 channel. Unlike the case of active_1 channel that failed to reproduce the HCHO distribution, a HCHO concentration lower than that in the inert channel is obtained in the active_2 channel, which agrees with the experimental observation. It is worth noting that, in the DME synthesis mechanism [70], the adsorption of HCHO is also a carbon source for the DME synthesis. Therefore, DME and HCHO zones extend to further downstream position in the active_2 channel compared with the active_1 channel. Clearly, the DME synthesis mechanism after including the additional HCHO

adsorption can predict the species distribution of the weak flame in the SUS321-coated channel successfully. More detailed discussion is given in next section.

### 5. 3. 4. SUS321 Wall Chemical Effect on Weak Flame

Generally speaking, the simulation results of the inert channel fit well with the experimental data of the quartz channel and the simulated species profiles in the active_2 channel agrees well with that measured in the SUS321-coated channel. Since the absolute concentration has certain extent of dependence on the gas-phase mechanism, the discussion in the present study is mainly focused on the distribution change with including surface reactions. In the simulation, DME starts to have a higher concentration in the active channel than that in the inert channel from $x = 19$ mm, and slightly increases until $x = 23$ mm in the active_2 channel instead of the continuous decrease in the inert channel. In between $x = 23$ to 30 mm, the DME mole fraction in the active_2 channel is $\sim 0.015$ higher than that in the inert channel, and the DME isn't fully consumed until $x = 38$ mm. In the experiment, the DME mole fraction starts to be higher from $x = 20$ mm in the SUS321-coated than that in the quartz channel. At $x = 25$ and 30 mm, compared with that in the quartz channel, the DME mole fraction in SUS321-coated channel is 0.015 and 0.02 higher, respectively. DME is fully consumed at $x = 35$ mm. Simulated CO mole fraction in the active_2 channel has a lower value compared with that in the inert channel till $x = 32.5$ mm, while the CO mole fraction measured in the SUS321-coated channel is also lower than that measured in the quartz channel till $x = 30$ mm. Simulated maximum CO mole faction is 0.042 at $x = 28.8$ mm in the inert channel and 0.026 at $x = 35.7$ mm in the active channel, while the largest measured CO mole fraction is 0.049 at $x = 30$ mm in the quartz channel and 0. 039 at $x = 35$ mm in the SUS321-coated channel. For the $CO_2$ distribution, the rising in the inert channel is $\sim 6$ mm upstream than that in the active_2 channel, while the rising in the quartz channel is $\sim 4$mm ahead of that in the SUS321-coated channel. The maximum HCHO concentration measured in the SUS321-coated channel is half of that in the quartz channel, but the HCHO zone extends to $x = 37$ mm. These differences between the quartz and SUS321-coated channels are well reproduced in the simulations of the inert and the active_2 channels. Simulated OH peak in the active_2 channel shifts 5.8 mm downstream with its

maximum concentration doubled compared with that in the inert channel, while the OH peak in the experiment also shifts 4 mm downstream after coating the SUS321.

Figure **5-12** compares the net reaction rate of DME in the inert and active channels. To note, in order to compare the DME consumption rate in the gas-phase with the generation rate over the surface, the net reaction rate of HCHO in gas-phase reactions is integrated in the wall normal direction to obtain the same unit as that in the surface reaction. The red solid line is for the inert channel and the blue solid line is the DME net reaction rate including both the gas-phase and surface reactions. The two dash lines are the net reaction rates of separately the gas-phase and surface reactions in the active channel. It is found that although the DME gas-phase consumption in the active channel is always larger than that in the inert channel, due to the DME re-forming from the active surface, the total DME consumption becomes smaller from $x = 17.5$ mm, and an increase of the DME concentration is observed at $x = 19 \sim 26$ mm. As a result, DME concentration is higher in the SUS321-coated channel compared with the quartz channel. It should be noted that $x = 19 \sim 26$ mm is the NTC region of DME reaction, while a large amount of HCHO, CO and $H_2$ do exist here in the meanwhile. In other words, the gas-phase reaction is weak while a relatively strong surface reaction occurs in this region. Therefore, it is not supervising to have a re-forming of DME in such a region.


### 5. 3. 5. Sensitivity to Initial Sticking Coefficient

In current surface reaction model, 3 reaction kinetic parameters, the initial sticking coefficients of CO, HCHO and $CH_3OH$, are given by fitting the simulated profiles with the experimental data. It should be noted that the given initial sticking coefficient is not optimized due to the difficulty of setting the fitting criterion. As discussed in section 5.1.2, all the gas-phase reaction mechanism cannot perfectly predict the species distribution in the quartz channel. Not only the absolute concentrations show differences, but also the shifting of flame position exists. As such, the absolute concentration profiles in the SUS321 coated-channel cannot be directly used for fitting the parameters in the surface reaction mechanism. Instead, the fitting results can only be judged by the distribution change tendencies. In this section, the sensitivity of species distributions to the initial sticking coefficients is demonstrated.

# Surface Reaction Model for Cool Flame

The initial sticking coefficient of $CH_3OH$, $S_{CH3OH}$, in the proposed surface reaction mechanism is set as 0.05. The simulated DME, CO and HCHO distributions with $S_{CH3OH}$ varying from 0.0001 to 1 are plotted in Figure **5-13**. It shows that the species distributions are not affected by $S_{CH3OH}$ when it is over 0.01. When $S_{CH3OH}$ is lower than 0.01, with a smaller $S_{CH3OH}$, less DME can extend to higher temperature region. Therefore, a value of 0.05 is proposed for $S_{CH3OH}$ in current model. More accurate value should be examined by future $CH_3OH$ measurement.

The initial sticking coefficient of CO, $S_{CO}$, in the proposed surface reaction mechanism is given as 0.3. Figure **5-14** compares the DME, CO and HCHO profiles, when $S_{CO}$ is changed to 1 and 0.1. Apparently, CO distribution is most sensitive to $S_{CO}$; obvious differences in DME distribution are also shown when $S_{CO}$ decreased from 0.3 to 0.1; no large concentration changes is found for HCHO when varying $S_{CO}$. Therefore, the fitting value of $S_{CO}$ is mainly judged by the CO distribution. With an increased $S_{CO}$, the CO concentration in the low-temperature oxidation zone is decreased, and the CO peak position in the high-temperature region is shifted to downstream, indicating a delayed hot flame ignition. In the experiments with the quartz and SUS321-coated channel, the maximum measured CO mole fraction locates at $x = 30$ mm and 35 mm respectively. The maximum mole fraction decreased from 0.049 to 0.040 after the SUS321 coating. It should be noted that the experimental profiles are measured with an interval of 5 mm in streamwise direction. In the simulated inert channel, the CO peak locates at $x = 28.5$ mm with a mole fraction of 0.042. With $S_{CO}$ equals to 1, the CO peak largely shifted 10.5 mm to downstream with a mole fraction of 0.041, indicating an over estimation of CO adsorption. With $S_{CO}$ equals to 0.1, the CO peak shifted 2.5 mm to downstream with a mole fraction of 0.035, 83.5% of the maximum value in the inert channel. The CO distribution changes are reasonable in the hot flame region with $S_{CO} = 0.1$, however, a higher instead of lower CO concentration is found in the low-temperature region. With the proposed $S_{CO} = 0.3$, the CO peak locates at 34.8 mm with a mole fraction of 0.027, and a slightly lower CO concentration in the low-temperature region is also predicted. The results suggest that the initial sticking coefficient of CO should be a value in between 0.1 and 1 for current model, 0.3 could be a proper value for it.

The initial sticking coefficient of HCHO, $S_{HCHO}$, in the proposed surface reaction mechanism is set as 0.0005. Figure **5-15** compares the DME, CO and HCHO profiles, when $S_{HCHO}$ is changed to 0.001 and 0.0001. Besides HCHO, DME and CO

distributions are also sensitive to $S_{HCHO}$. With a higher $S_{HCHO}$, a lower HCHO concentration is founded. As a consequence, the consumption of DME in the low-temperature region is faster. The CO concentration in the high-temperature region is also largely influenced by $S_{HCHO}$, since HCHO is the main source for CO formation in high temperature oxidation. When $S_{HCHO} = 0.001$ is applied, the CO peak in high-temperature region vanished due to the strong HCHO adsorption. And the HCHO concentration at $x = 25$ mm is already decreased to 10% of the peak value, which is much too low comparing with the experimental data. Thus, $S_{HCHO} = 0.001$ is over estimated for HCHO adsorption in current model. With $S_{HCHO} = 0.0001$, the maximum HCHO concentration is 70% of that in the simulated inert channel, which is higher than the 50% comparing the SUS321-coated with the quartz channel. With the proposed $S_{HCHO} = 0.0005$, the maximum HCHO concentration is 49% of that in the simulated inert channel, fitting very well with the experimental data. As such, $S_{HCHO} = 0.0005$ seems to be a reasonable value, and the initial sticking coefficient of HCHO should be in the range of 0.0001 to 0.001 for current model.

## 5. 4. SUS321 Wall Chemical Effect on Wall-stabilized Cool Flame

### 5. 4. 1. Wall-stabilized Cool Flame

Lee et al. [90] proposed a wall-stabilized cool flame shown in Figure **5-16**. A heated wall is located 15 mm away from the nozzle. Premixed DME/$O_2$ is injected towards the wall. With certain wall temperature, equivalence ratio and flow rate, a cool flame can be stabilized near the wall. Compared with the weak flame in the micro channel, the wall-stabilized cool flame has much larger flow rate. The surface reaction model developed for the weak flame in SUS321-coated micro channel is also applied in the case of wall-stabilized cool flame to examine the wall chemical effect on such a more practical combustion field that mimics the head-on quenching in the engine.

Same computation domain, numerical scheme and boundary conditions as adopted by Lee et al. [90] are adopted. Figure **5-17** shows the computation domain. Equivalence ratio of 0.2, temperature of 300 K and inlet flow velocity of 4.08 cm/s are set at the nozzle inlet boundary. After flowing through the nozzle, the flow velocity at the nozzle outlet is increased to 65.8 cm/s, as shown in Figure **5-19**. Zero

heat flux is set at the wall boundary of the nozzle. The heated wall has a constant wall temperature of 700 K. The outlet is set as the pressure outlet. CH$_4$/DME 2014 is adopted as the gas-phase reaction mechanism.

### 5. 4. 2. Influence of Surface Reaction on Wall-stabilized Cool Flame

Figure **5-19** shows simulated DME, CO, CO$_2$ and HCHO distributions in the wall-stabilized cool flame over either an inert or an active wall surface. Compared with that in the inert wall case, the HCHO concentration in the active wall case is much lower. In the inert wall case, the maximum concentration of HCHO over the wall surface is $2.2 \times 10^{-4}$ koml/m$^3$, and the maximum drops to $1.6 \times 10^{-4}$ koml/m$^3$ in the active wall case. The maximum concentration position is slightly away from the wall surface, because HCHO is destructed on the wall surface. Much higher CO and CO$_2$ concentrations is observed in the active wall case despite of the surface adsorption. M. Mann et al. mentioned in their CO-LIF measurement for the head-on quenching study [13] that measured CO concentrations are higher compared to the simulation for both lean and stoichiometric flames in the near wall region. Considering that their wall is made of stainless steel, a possible explanation to this discrepancy is that the wall surface reaction has not been taken into consideration.

Comparing the weak flame and the wall-stabilized cool flame, after including the surface reaction, it is observed that the CO concentration is decreased by the SUS321 surface in the weak flame, but increased by the SUS321 surface in the wall-stabilized cool flame. The decrease of CO concentration in the weak flame is easy to understand, because the adsorption of CO is included in the mechanism. The cause of an increase of CO concentration in the wall-stabilized cool flame can be explained by the reaction rate plotted in Figure **5-20**. All plots are simulation results along the wall surface. Figure **5-20** (a) and (b) shows the rate diffidence of the CO adsorption and desorption, in other words, the net value of the CO consumption via the surface reaction. It is shown that the net CO consumption rate on the surface has the same order of $10^{-6}$ kmol/m$^2$s in both the weak flame and the wall-stabilized cool flame. In the gas-phase reaction, R31: HCO + O$_2$ <=> CO + HO$_2$, R468: HOCH$_2$OCO <=> HOCH$_2$O + CO, and R493: CH$_3$OCO <=> CH$_3$O + CO are identified as the three reactions having the major contribution to the CO generation. As shown in Figure **5-20** (c) and (d), the gas-phase CO generation is significantly promoted after

including the surface reactions in both the weak flame and the wall-stabilized cool flame. However, the order of the CO gas-phase generation rate in the wall-stabilized cool flame is $10^{-2}$ kmol/m$^3$s, while the rate in the weak flame has the order of $10^{-3}$ kmol/m$^3$s, which is more than one order lower.. Although the promoting effects of the surface reaction on gas-phase generation of CO are similar in both the weak flame and the wall-stabilized cool flame, the gas-phase generation rate has one order difference. The absolute value of increase in CO gas-phase generation after applying the surface reaction mechanism is much larger in the wall-stabilized cool flame than that in the weak flame. On the other hand, the CO consumptions via the surface reaction are in the same level for both types of flame. Thus, higher CO concentration over the active wall compared with the inert wall is observed in the wall-stabilized cool flame.

The large CO generation rate in the wall-stabilized cool flame is due to the high $O_2$ concentration. It should be noted that the wall-stabilized cool flame is a DME/$O_2$ flame with an equivalence ratio of 0.2. The concentration of $O_2$ is one order higher than that in the DME/air weak flame. A high $O_2$ concentration directly promoted the reaction of R31. In the meanwhile, $HOCH_2OCO$ and $CH_3OCO$ are the intermediate species in the low temperature oxidation pathway, which is initialized by the H abstraction of DME and then the addition of $O_2$ to $CH_3OCH_2$. Therefore, high $O_2$ concentration also leads to large reaction rates of R468 and R493.

The promoting effect of the SUS321 surface on CO gas-phase generation is attributed to the adsorption of HCHO. As mentioned before, the low temperature oxidation pathway starts from the H abstraction of DME with H and OH. HCHO is the largest competitor to DME for H and OH. When HCHO is consumed by the wall, the H abstraction of DME is promoted. As shown in Figure **5-21**, ~50% more $CH_3OCH_2$ is observed over the active wall compared with that over the inert wall. One possible path to form $HOCH_2OCO$ is through $CH_3OCH_2 \rightarrow CH_3OCH_2O_2 \rightarrow CH_2OCH_2O_2H \rightarrow O_2CH_2OCH_2O_2H \rightarrow HO_2CH_2OCHO \rightarrow OCH_2OCHO \rightarrow HOCH_2OCO$. Thus, a higher $CH_3OCH_2$ concentration leads to a faster $CH_3OCH_2$ generation and then a faster CO generation. As a result, the gas-phase CO generation is promoted by the surface reaction.

Further experiment and numerical simulation are necessary to fully examine the wall chemical effect on the wall-stabilized cool flame. Nevertheless, it is demonstrated by the current simulation result that the wall chemical effect influences

not only the weak flame, but also more practical flames with faster gas-phase reaction and flow such as the wall-stabilized cool flame.

## 5. 5. Summary

In order to obtain a surface reaction model that successfully describes the wall chemical effect of SUS321 on the DME weak flame, different surface reaction mechanisms are examined. The radical quenching model, which was used to describe the wall chemical effect on the methane normal flame, is found to be inadequate describe the weak flame over the SUS321 surface. Therefore, a new surface reaction model with two hypotheses, i.e. the DME synthesis and the HCHO adsorption, are proposed for the weak flame over the SUS321 surface. It is shown that simulated species distributions using this model agree well with those measured in the weak flame over the SUS321 surface.

As elucidated by simulation results using the proposed model, DME is synthesized from adsorbed CO, $CO_2$, HCHO and $H_2$ at the SUS321 surface, which is the cause of high DME concentration in the downstream high temperature region of the SUS321-coated channel. The HCHO zone extending to the high temperature region is also attributed to the high DME concentration over there. As the result of high DME and HCHO concentrations, the hot flame zone with the OH, CO and $CO_2$ peaks also shifts to the downstream high temperature region.

The newly-proposed surface reaction model is employed in the simulation of a wall-stabilized cool flame over the SUS321 surface. It was demonstrated that the wall chemical effect described by this surface reaction model influences not only the weak flame in small channels, but also other combustion fields such as the wall-stabilized cool flame with a faster flow than the weak flame, as long as the low temperature oxidation is important.
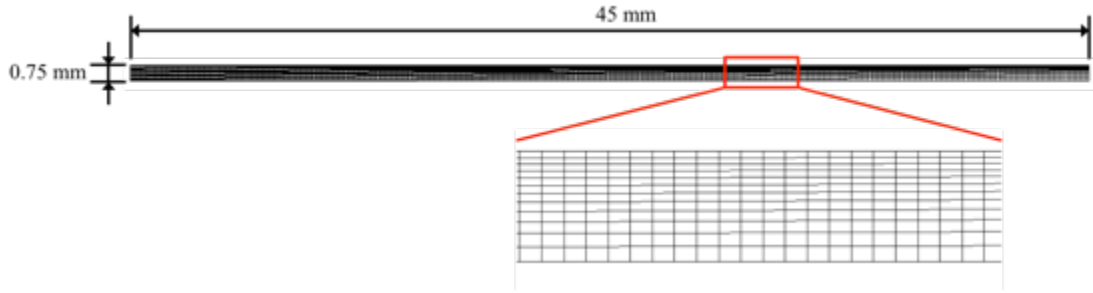
Figure 5-1 Mesh of the weak flame 2D simulation (half-width).
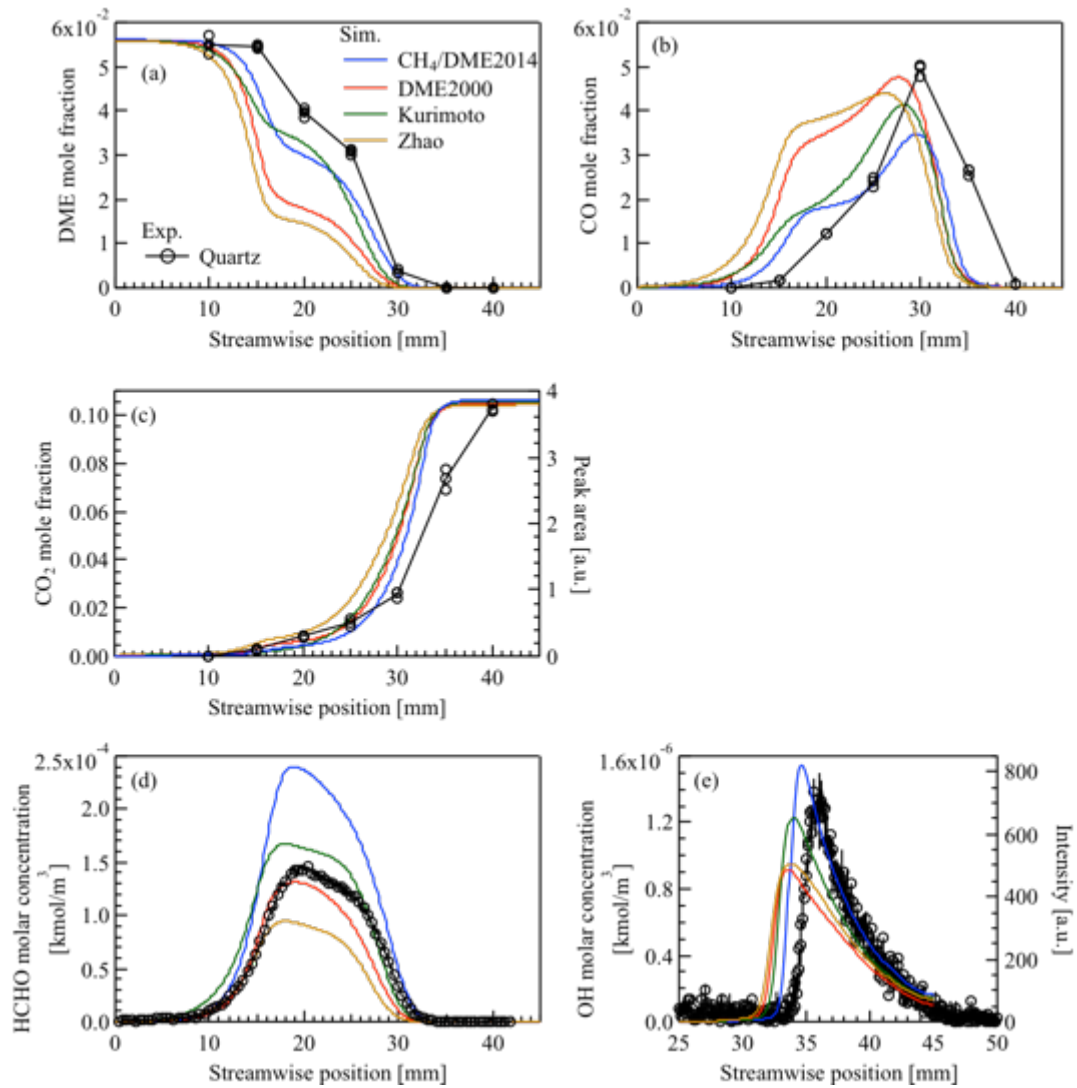


Figure 5-2 Species distribution comparison between the simulated inert channel with mechanism DME 2000 [21][22], CH4/DME 2014 [26], Zhao [68] and Kurimoto [69]. Experimental results of the quartz channel are also plotted.
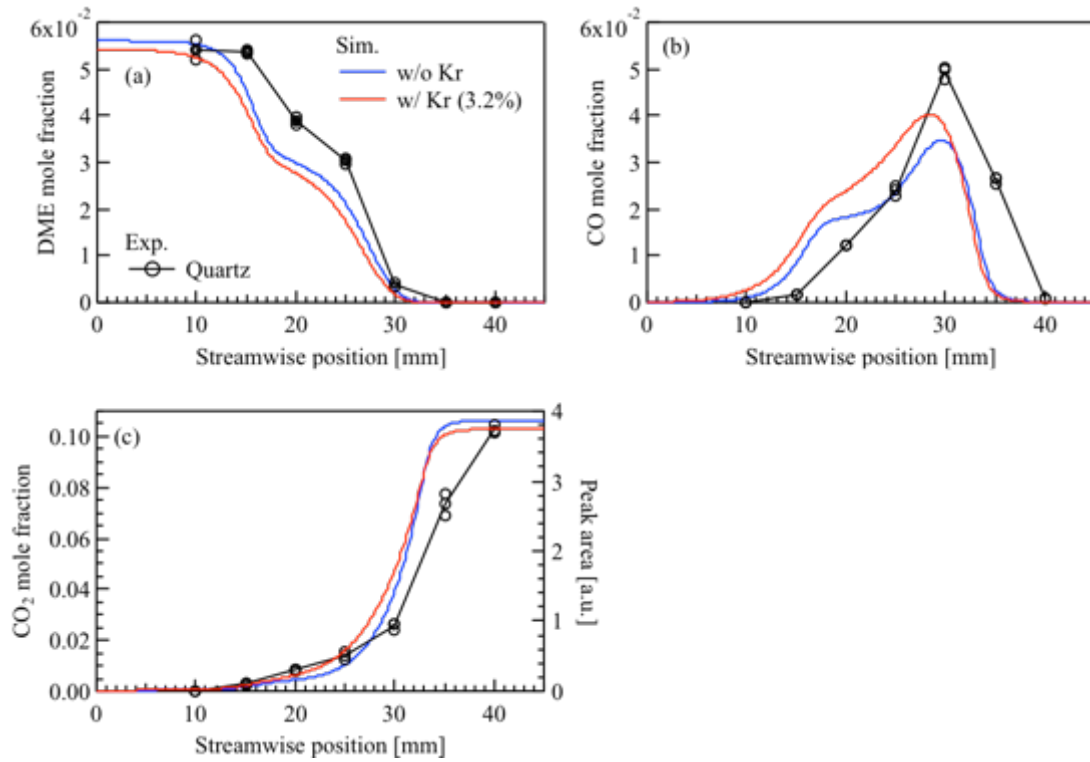
Figure 5-3 Species distribution comparison between the simulated inert channel with or without Kr. Experimental results of the quartz channel are also plotted.
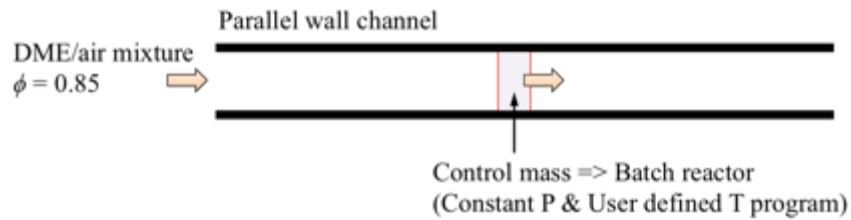


Figure 5-4 Scheme for transfer channel to batch reactor.
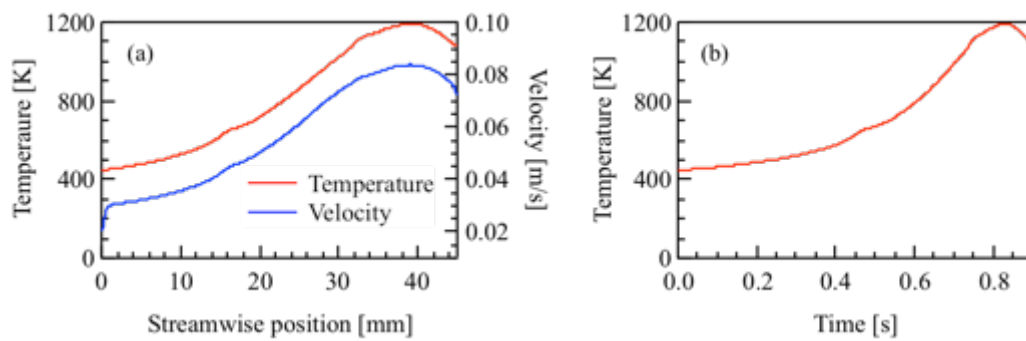


Figure 5-5 (a) Temperature and velocity profiles in the parallel wall channel. (b) Temperature program for the batch reactor.
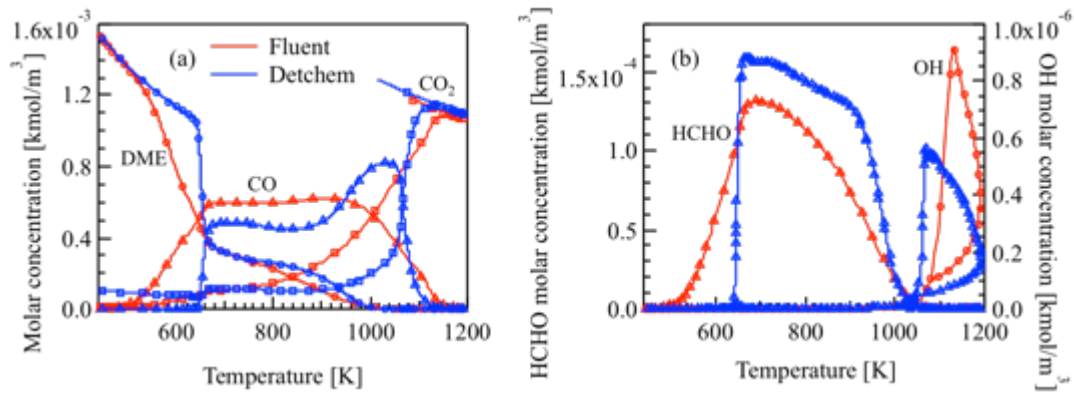
Figure 5-6 Comparison of the simulated species concentration in the inert channel with the 0D (DETCHEM Batch) and 2D (FLUENT) simulation.
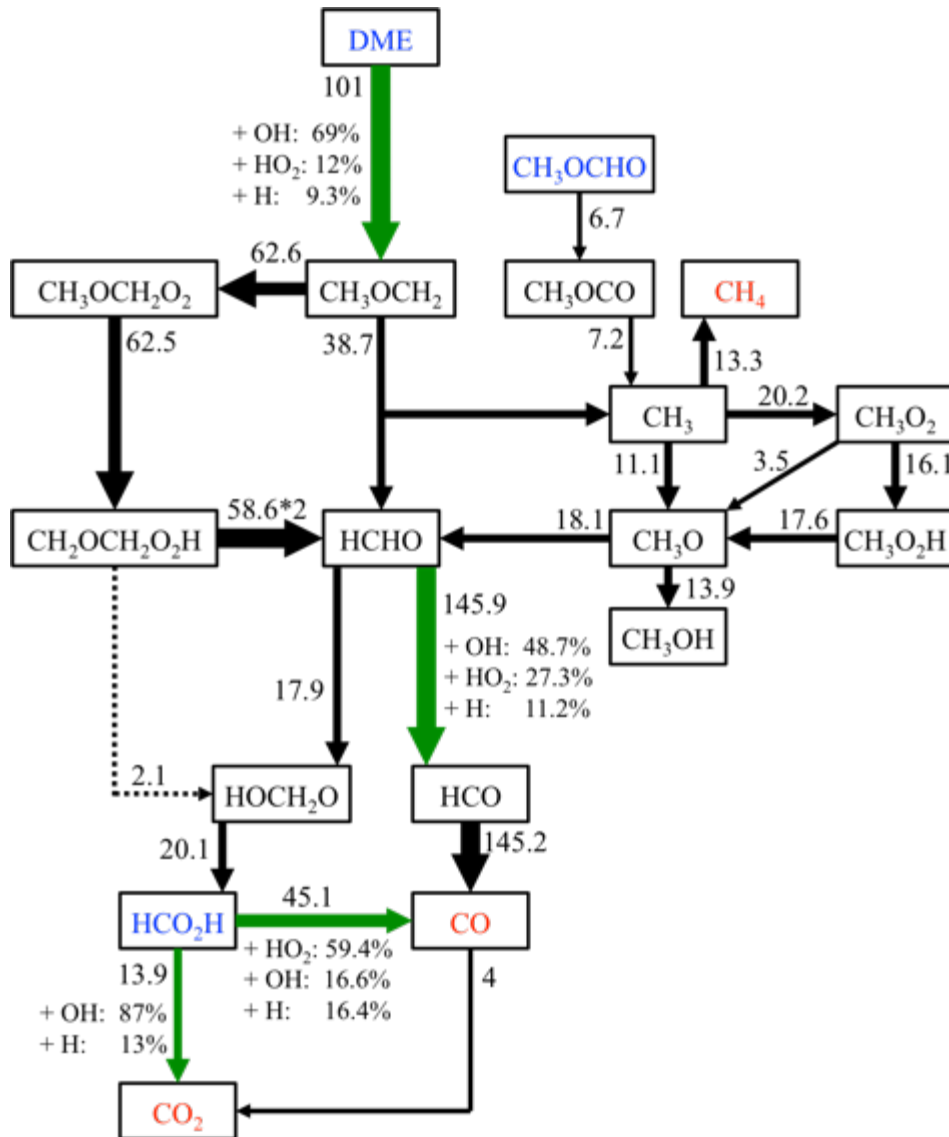


Figure 5-7 Reaction pathway analysis with DETCHEM at t = 0.6 s (770 K).
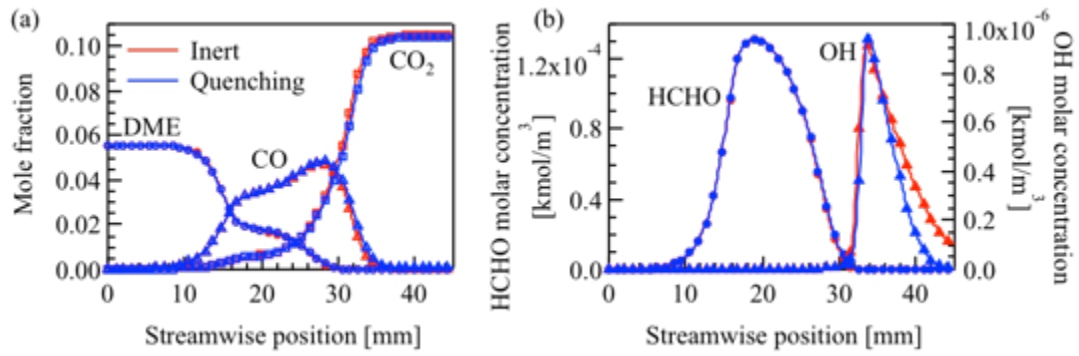
Figure 5-8 Species distribution comparison between the simulated inert channel and the channel with radical quenching model.
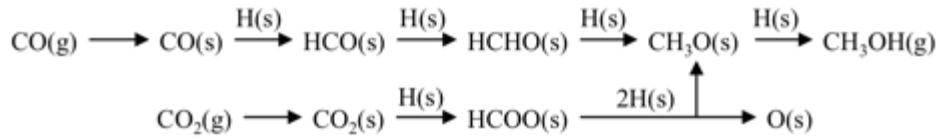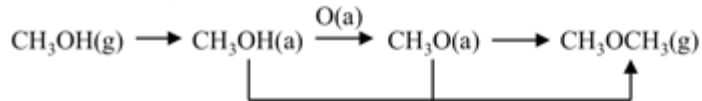


Figure 5-9 DME synthesis mechanism [70].
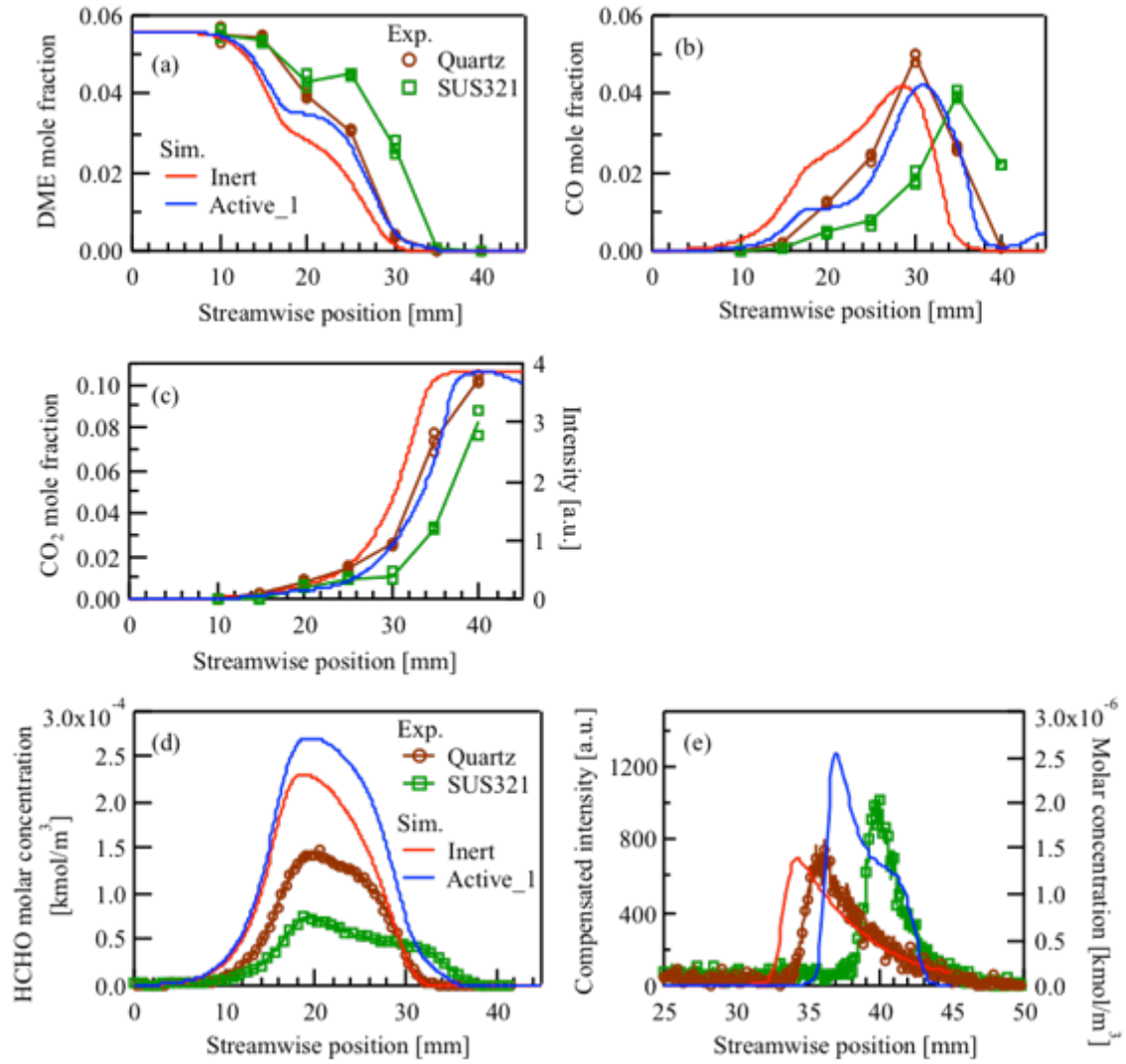
Figure 5-10 Species distribution comparison between the FLUENT simulated inert and active_1 channel (DME synthesis mechanism). Experimental results of the quartz and SUS321-coated channel are also plotted.
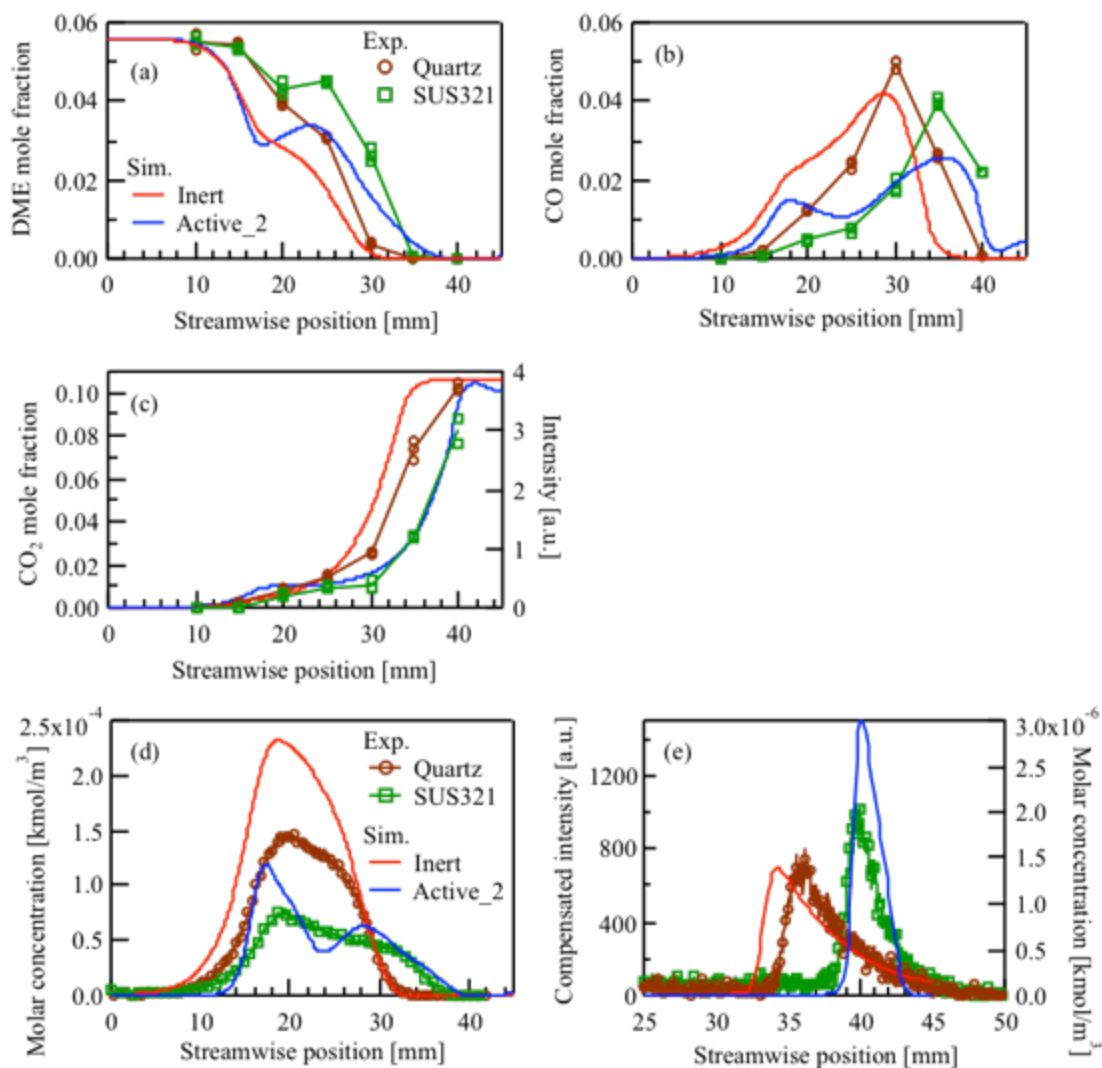
Figure 5-11 Species distribution comparison between the FLUENT simulated inert
and active_2 channel (including both HCHO adsorption and DME synthesis
mechanism). Experimental results of the quartz and SUS321-coated channel are also
plotted.
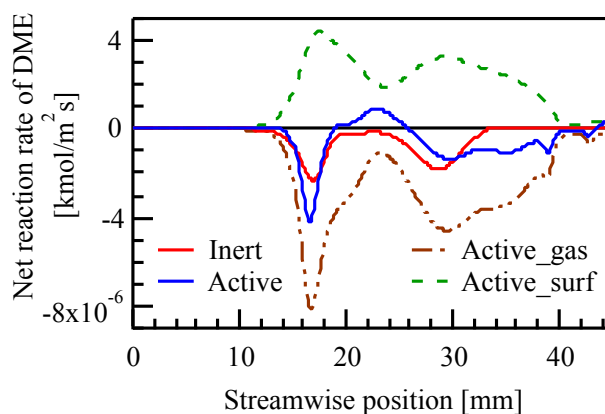


Figure 5-12 Net reaction rate of DME in the inert and the active_2 channel.
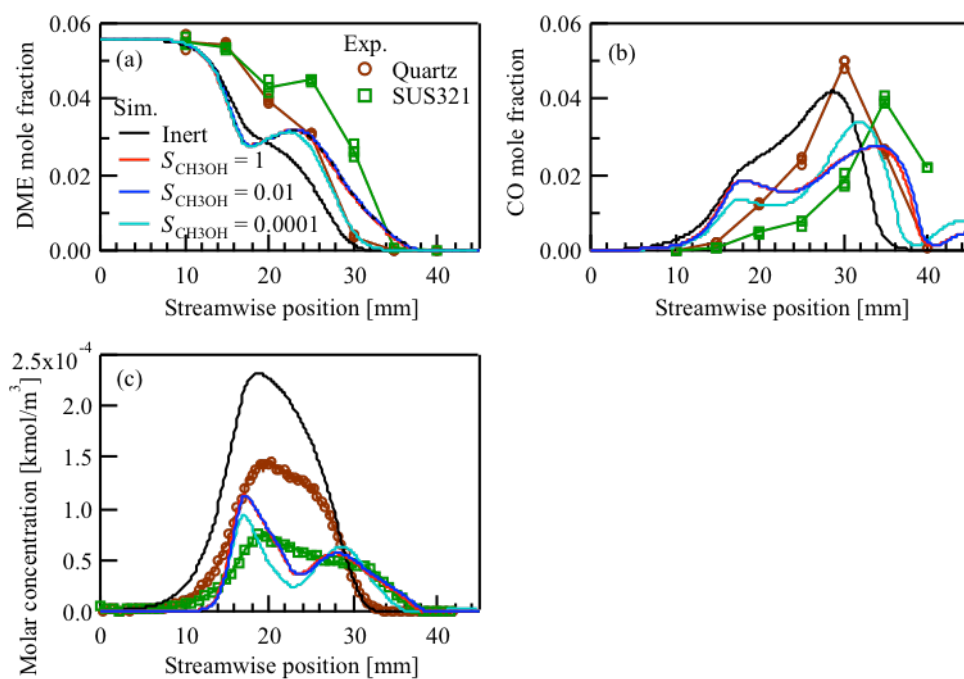
Figure 5-13 Sensitivity to $S_{CH3OH}$. (a) DME, (b) CO and (c) HCHO.
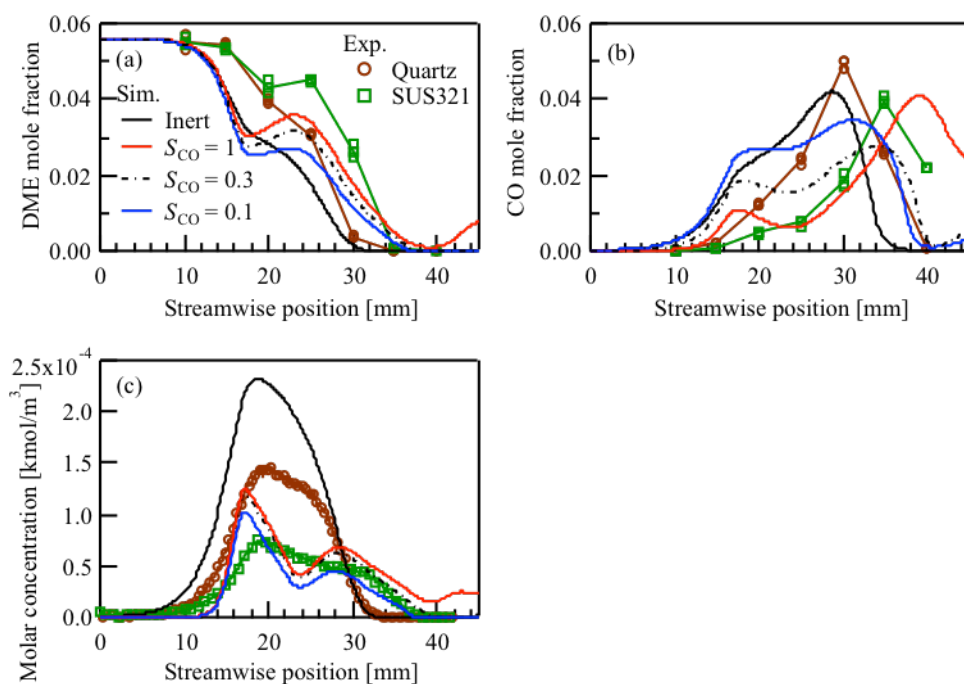


Figure 5-14 Sensitivity to $S_{CO}$. (a) DME, (b) CO and (c) HCHO.
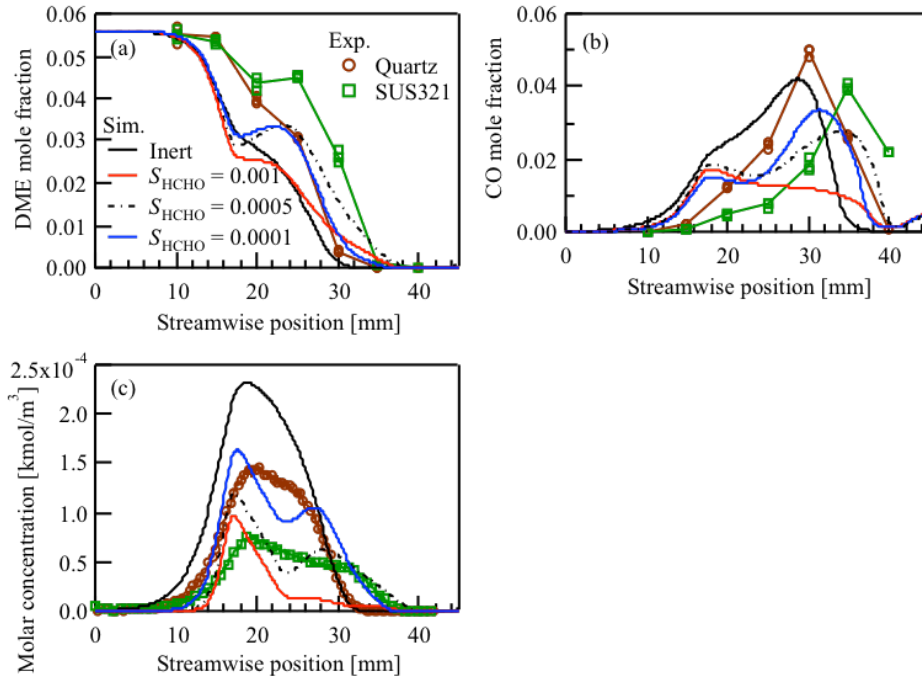
Figure 5-15 Sensitivity to $S_{HCHO}$. (a) DME, (b) CO and (c) HCHO.
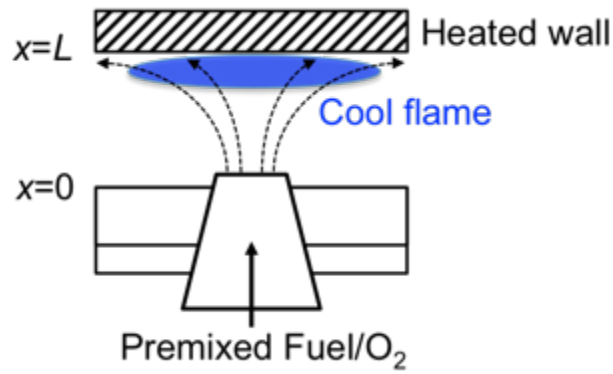


Figure 5-16 Schematic of the burner configuration and the stabilization of the cool flame near the wall [90].
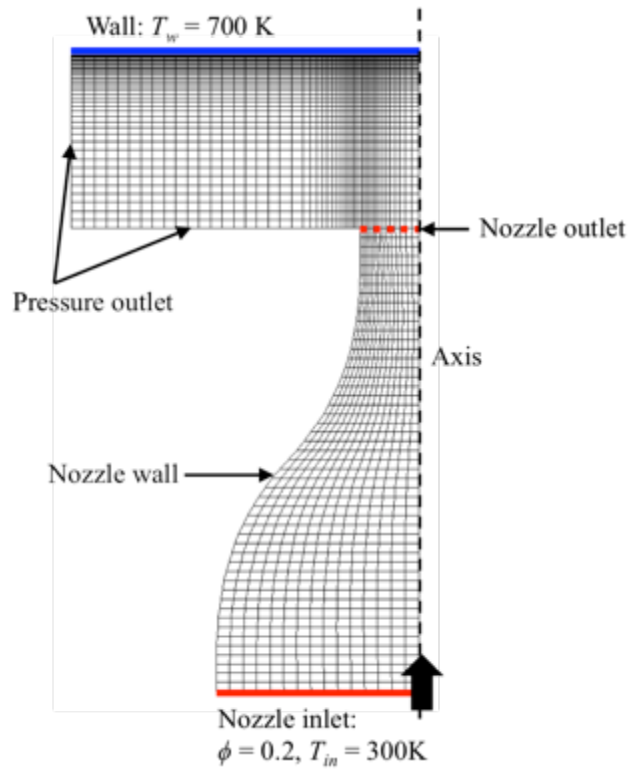
Figure 5-17 Calculation domain of wall-stabilized cool flame [90].
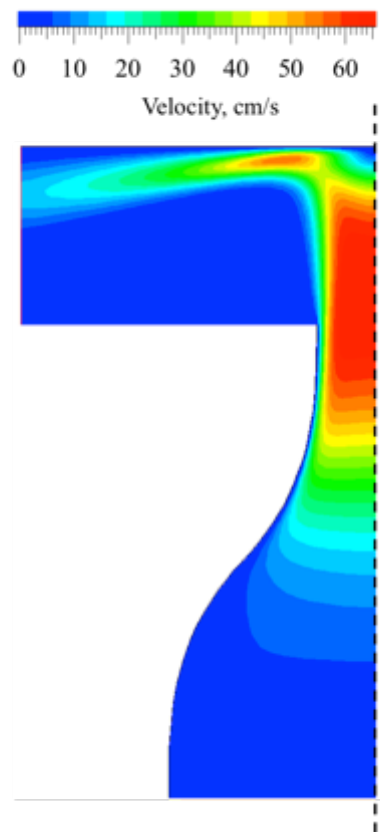


Figure 5-18 Velocity distribution of the wall-stabilized cool flame.
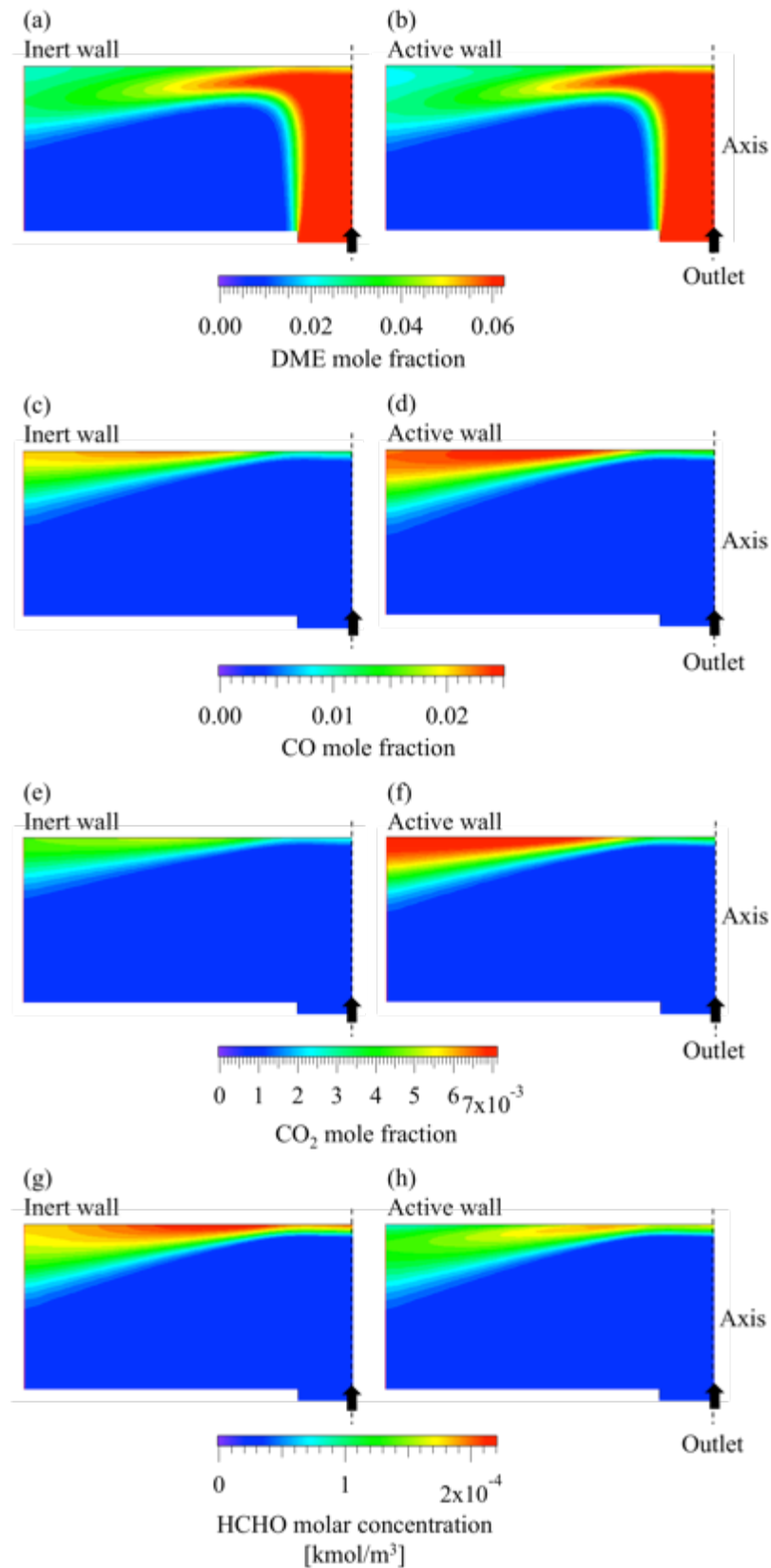
Figure 5-19 Species distributions in the wall-stabilized cool flame.
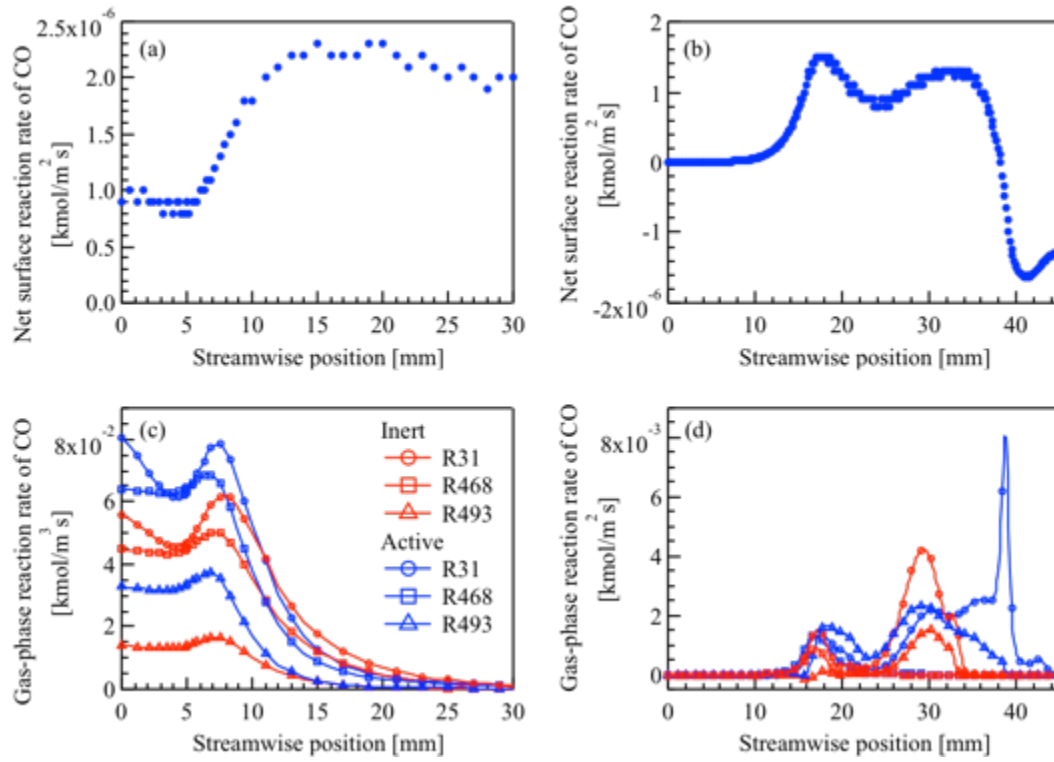
Figure 5-20 CO related reaction rate at the wall surface in the wall-stabilized cool flame and the weak flame.
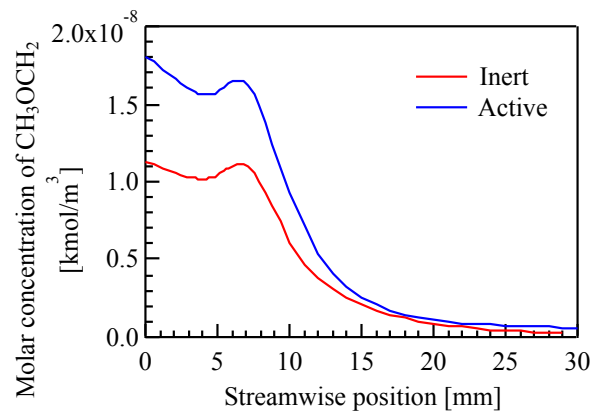


Figure 5-21 $CH_3OCH_2$ concentration over the wall surface in the wall-stabilized cool flame.

# Chapter 6 Conclusions

Wall chemical effect on the low temperature oxidation has been studied by examining the influence of wall surface materials on a DME/air weak flame. The weak flame was established in a quartz micro flow reactor with a rectangular cross section, where the wall temperature distribution has a prescribed gradient in the streamwise direction. Thin film (~ 150 nm) of different materials such as alumina, SiC, SUS321, Inconel600, iron, nickel and chromium were deposited on the inner surface of the quartz channel. Gas species including DME, CO, $CO_2$, and HCHO were measured with gas chromatography (GC). Two-dimensional distributions of HCHO and OH were captured with the planar laser-induced fluorescence (PLIF) system. These experimental data have been compared with different wall chemical boundary. Simulation with detailed gas-phase and surface reactions have also been made. Surface reaction model has been proposed for SUS321, for which peculiar wall chemical effect is observed. The conclusions are as follows:

(1) A rectangular micro flow reactor with a streamwise temperature gradient is developed for the wall chemical effect investigation. The present rectangular channel offers a better optical access than a circular tube. By using a detachable wall, thin-film of different materials can be deposited on the inner wall surface, to change the wall chemical boundary condition but to keep the thermal boundary condition unchanged. It is found that the same flame patterns as in the weak flame in the circular tube were observed at similar flow velocity.

(2) Wall chemical effect in the hot flame region of the DME/air weak flame is investigated using OH-PLIF. It found that the near-wall OH concentration is decreased in the order of alumina, quartz and SUS321, which is the same as previous results for the normal $CH_4$/air flame. The estimated initial sticking coefficients $S_0$ are lower than those for normal flame, and 0.001, 0.0015 and 0.006 for alumina, quartz and SUS321, respectively. Sensitivity analysis based on numerical simulation indicates that OH distribution is most sensitive to the adsorption of OH in the weak flame, while most sensitive to the adsorption of H in the normal flame.

(3) Streamwise distributions of gas species in the weak flame have been measured using GC-MS. It is found that, whereas SiC is identified as the active material for radical quenching in the normal flame, streamwise distributions of DME, CO and

121

# Conclusions

CO$_2$ in the SiC-coated channel are the same as those in the inert quartz channel. On the other hand, very unique distributions were found for SUS321-and Inconel600-coated channel. DME has much higher concentration in these alloys-coated channels at the NTC region. Since DME still remains in the steamwise position corresponding to the wall temperature of 1030 - 1150 K, the HCHO zone is also extended to the higher temperature region. As a consequence, the hot flame is shifted downstream for the SUS321 or Inconel600 surfaces. DME distributions in the Fe-, Ni- and Cr-coated channels indicate that Fe and Ni make the largest contribution to the DME increment. These findings suggest that the surface reaction over these alloys or metals has strong influence on the low-temperature oxidation, leading to delay of the hot flame region in the weak flame.

(4) Based on the present experimental data, two hypotheses have been proposed for the wall chemical effects on the SUS321 surface: the adsorption of HCHO and the synthesis of DME. Decrease in the HCHO concentration peak can be explained by the adsorption of HCHO, and the extended DME and HCHO zones can be explained by the synthesis of DME on the SUS321 surface. A new surface reaction model based on these hypotheses can predict the unique gas species distribution over the SUS321 surface. It is also found in numerical simulation that the wall-stabilized cool flame is markedly modified by the wall chemical effect, showing possibility of large wall chemical effect in the low temperature oxidation region.

# References

[1]   F. Birol. World energy outlook 2016. International energy agency, 2017.

[2]   U.S. EIA. Short–term energy outlook. Washington, 2017.

[3]   J.P. Angelos, et al. "HCCI Engine". http://cheme.scripts.mit.edu/green-group/hcci-engines/.

[4]   R.H. Stanglmaier, C.E. Roberts. Homogeneous charge compression ignition (HCCI): benefits, compromises, and future engine applications. SAE Technical Paper, 1999.

[5]   K. Okude, K. Mori, S. Shiino, et al. Premixed compression ignition (PCI) combustion for simultaneous reduction of NOx and soot in diesel engine. SAE Technical Paper, 2004.

[6]   T. Poinsot, D. Veynante, Theoretical and numerical combustion, 3rd ed., T. Poinsot, Bordeaux, France, 2012.

[7]   A. Dreizler, B. Böhm. Advanced laser diagnostics for an improved understanding of premixed flame-wall interactions. *Proceedings of the Combustion Institute.* 2015, 35(1): 37-64.

[8]   S. Demesoukas, C. Caillol, P. Higelin, et al. Near wall combustion modeling in spark ignition engines. Part A: Flame–wall interaction. *Energy Conversion and Management*, 2015, 106: 1426-1438.

[9]   S. Lloyd, E. Weinberg. A Burner for Mixtures of Very Low Heat Content. *Nature*, 1974, 251: 47-49.

[10]  J. Ahn, C. Eastwood, L. Sitzki, et al. Gas-phase and catalytic combustion in heat-recirculating burners. *Proceedings of the Combustion Institute*, 2005, 30(2): 2463-2472.

[11]   A. Bohlin, M. Mann, B.D. Patterson, et al. Development of two-beam femtosecond/picosecond one-dimensional rotational coherent anti-Stokes Raman spectroscopy: time-resolved probing of flame wall interactions. *Proceedings of the Combustion Institute,* 2015, 35(3): 3723-3730.

[12]  T. Fuyuto, H. Kronemayer, B. Lewerich, et al. Temperature and species measurement in a quenching boundary layer on a flat-flame burner. *Experiments in fluids*, 2010, 49(4): 783-795.

# References

[13] M. Mann, C. Jainski, M. Euler, et al. Transient flame–wall interactions: Experimental analysis using spectroscopic temperature and CO concentration measurements. *Combustion and Flame*, 2014, 161(9): 2371-2386.

[14] C. Miesse, R.I. Masel, Short M, et al. Experimental observations of methane–oxygen diffusion flame structure in a sub-millimetre microburner. *Combustion Theory and Modelling*, 2005, 9(1): 77-92.

[15] K.T. Kim, D.H. Lee, S. Kwon. Effects of thermal and chemical surface–flame interaction on flame quenching, *Combustion and Flame*. 2006, 146: 19-28.

[16] Y. Saiki, Y. Suzuki. Effect of wall surface reaction on a methane-air premixed flame in narrow channels with different wall materials. *Proceedings of the Combustion Institute*, 2013, 34(2): 3395-3402.

[17] Y. Saiki, Y. Fan, Y. Suzuki. Radical quenching of metal wall surface in a methane-air premixed flame. *Combustion and Flame*, 2015, 162(10): 4036-4045.

[18] C.E. Arrieta. Measurement of OH radical adsorption on a silicon carbide surface using OH-PLIF for an improved understanding of premixed combustion in porous media burners – Report. Unpublished.

[19] J.F. Griffiths, J.A. Barnard. Flame and Combustion, 3rd Edition, CRC Press, 1995.

[20] A. A. Pekalski, J.F. Zevenberge, H.J. Pasman et al. The relation of cool flames and auto-ignition phenomena to process safety at elevated pressure and temperature, *Journal of hazardous materials*, 2002, 93(1): 93-105.

[21] S.L. Fischer, F.L. Dryer, H.J. Curran. The reaction kinetics of dimethyl ether. I: High-temperature pyrolysis and oxidation in flow reactors. *International Journal of Chemical Kinetics*, 2000, 32(12): 713-740.

[22] H.J. Curran, S.L. Fischer, F.L. Dryer. The reaction kinetics of dimethyl ether. II: Low-temperature oxidation in flow reactors. *International Journal of Chemical Kinetics*, 2000, 32(12): 741-759.

[23] H. Davy. Some new experiments and observations on the combustion of gaseous mixtures, with an account of a method of preserving a continued light in mixtures of inflammable gases and air without flame. *Philosophical Transactions of the Royal Society of London*, 1817, 107, 77-85.

# References

[24] H.J. Emeléus. The light emission from the phosphorescent flames of ether, acetaldehyde, propaldehyde, and hexane. *Journal of the Chemical Society (Resumed)*, 1929,1733-1739.

[25] U. Azimov, N. Kawahara, E. Tomita. UV–visible light absorption by hydroxyl and formaldehyde and knocking combustion in a DME-HCCI engine. *Fuel*, 2012, 98: 164-175.

[26] U. Burke, K.P. Somers, P. O'Toole, et al. An ignition delay and kinetic modeling study of methane, dimethyl ether, and their mixtures at high pressures. *Combustion and Flame*, 2015, 162(2): 315-330.

[27] Z. Zhao, M. Chaos, A. Kazakov, et al. Thermal decomposition reaction and a comprehensive kinetic model of dimethyl ether. *International Journal of Chemical Kinetics*, 2008, 40(1): 1-18.

[28] S.H. Won, B. Jiang, P. Diévart, et al. Self-sustaining *n*-heptane cool diffusion flames activated by ozone. *Proceedings of the Combustion Institute*, 2015, 35(1): 881-888.

[29] C.B. Reuter, M. Lee, S. H. Won, et al. Study of the low-temperature reactivity of large n-alkanes through cool diffusion flame extinction. *Combustion and Flame*, 2017, 179: 23-32.

[30] K. Maruta, T. Kataoka, N.I. Kim, et al. Characteristics of combustion in a narrow channel with a temperature gradient. *Proceedings of the Combustion Institute*, 2005, 30 (2), 2429-2436.

[31] H. Oshibe, H. Nakamura, T. Tezuka et al., Stabilized three-stage oxidation of DME/air mixture in a micro flow reactor with a controlled temperature profile. *Combustion and Flame*, 2010, 157 (8), 1572-1580.

[32] A. Yamamoto, H. Oshibe, H. Nakamura, et al. Stabilized three-stage oxidation of gaseous *n*-heptane/air mixture in a micro flow reactor with a controlled temperature profile. *Proceedings of the Combustion Institute*, 2011, 33 (2), 3259-3266.

[33] K. Maruta. Flame Chromatography: Toward Fuel Indexing Based on Multiple Weak Flames in a Meso-Scale Channel with a Prescribed Temperature Profile. *ASME 2011 9th International Conference on Nanochannels, Microchannels, and Minichannels*. American Society of Mechanical Engineers, 2011: 593-598.

# References

[34] K. Hirata, "流れ方向に温度勾配を持つマイクロチャネルを用いた化学的消炎効果の LIF 計測", Master Dissertation, Mechanical Engineering Dept., The University of Tokyo, 2014.

[35] Thermal Riko, GA298 Manual.

[36] C.B. Willingham, W.J. Taylor, J.M. Pignocco, et al. Vapor pressures and boiling points of some paraffin, alkylcyclopentane, alkylcyclohexane, and alkylbenzene hydrocarbons. *Journal of Research of the National Bureau of Standards*, 1945, 35(3): 219-244.

[37] A. Lozano, B. Yip, R.K. Hanson. Acetone: a tracer for concentration measurements in gaseous flows by planar laser-induced fluorescence. *Experiments in Fluids*, 1992, 13(6): 369-376.

[38] M. Barret, S. Houdier, F. Domine. Thermodynamics of the formaldehyde−water and formaldehyde− ice systems for atmospheric applications. *The Journal of Physical Chemistry A*, 2010, 115(3): 307-317.

[39] J.M. Seitzman, R.K. Hanson. "Planar Fluorescence Imaging in Gases," in Experimental Methods for Flows With Combustion ed. A. Taylor. Academic Press, London, 1993.

[40] R.K. Hanson, J.M. Seitzman, P.H. Paul. Planar laser-fluorescence imaging of combustion gases. *Applied Physics B: Lasers and Optics*, 1990, 50(6): 441-454.

[41] R.K. Hanson. Combustion diagnostics: planar imaging techniques. *Symposium (International) on Combustion. Elsevier*, 1988, 21(1): 1677IN51681-1680IN81691.

[42] G.H. Dieke, H.M. Crosswhite. The ultraviolet bands of OH fundamental data. *Journal of Quantitative Spectroscopy and Radiative Transfer*, 1962, 2(2): 97-199.

[43] J.E. Harrington, K.C. Smyth. Laser-induced fluorescence measurements of formaldehyde in a methane/air diffusion flame. *Chemical Physics Letters*, 1993, 202(3-4): 196-202.

[44] C. Brackmann, J. Nygren, X. Bai, et al. Laser-induced fluorescence of formaldehyde in combustion using third harmonic Nd: YAG laser excitation. *Spectrochimica Acta Part A: Molecular and Biomolecular Spectroscopy*, 2003, 59(14): 3347-3356.

# **References**

[45] D.C. Kyritsis, V.S. Santoro, A. Gomez. The effect of temperature correction on the measured thickness of formaldehyde zones in diffusion flames for 355 nm excitation. *Experiments in fluids*, 2004, 37(5): 769-772.

[46] Lavision System, Software and Manual.

[47] S. Böckle, J. Kazenwadel, D.I. Shin, et al. Simultaneous single-shot laser-based imaging of formaldehyde, OH, and temperature in turbulent flames. *Proceedings of the Combustion Institute*, 2000, 28(1): 279-286.

[48] S. Böckle, J. Kazenwadel, T. Kunzelmann, et al. Single-shot laser-induced fluorescence imaging of formaldehyde with XeF excimer excitation. *Applied Physics B: Lasers and Optics*, 2000, 70(5): 733-735.

[49] P. Liu, Z. He, G.L. Hou, et al. The Diagnostics of Laser-Induced Fluorescence (LIF) Spectra of PAHs in Flame with TD-DFT: Special Focus on Five-Membered Ring. *The Journal of Physical Chemistry A*, 2015, 119(52): 13009-13017.

[50] Horiba, iHR Brochure.

[51] H. Yamada, K. Suzaki, H. Sakanashi, et al. Kinetic measurements in homogeneous charge compression of dimethyl ether: role of intermediate formaldehyde controlling chain branching in the low-temperature oxidation mechanism. *Combustion and Flame*, 2005, 140(1): 24-33.

[52] I. Liu, N.W. Cant, J.H. Bromly, et al. Formate species in the low-temperature oxidation of dimethyl ether. *Chemosphere*, 2001, 42(5): 583-589.

[53] S. Deng, P. Zhao, D. Zhu, et al. NTC-affected ignition and low-temperature flames in nonpremixed DME/air counterflow. *Combustion and Flame*, 2014, 161(8): 1993-1997.

[54] S.A. Skeen, J. Manin, L.M. Pickett. Simultaneous formaldehyde PLIF and high-speed schlieren imaging for ignition visualization in high-pressure spray flames. *Proceedings of the Combustion Institute*, 2015, 35(3): 3167-3174.

[55] P. Zhao, W. Liang, S. Deng, et al. Initiation and propagation of laminar premixed cool flames. *Fuel*, 2016, 166: 477-487.

[56] S. Raimondeau, D. Norton, D.G. Vlachos, et al. Modeling of high-temperature microburners. *Proceedings of the Combustion Institute*, 2002, 29(1): 901-907.

[57] Y. Kizaki, H. Nakamura, T. Tezuka, et al. Effect of radical quenching on CH 4/air flames in a micro flow reactor with a controlled temperature profile. *Proceedings of the Combustion Institute*, 2015, 35(3): 3389-3396.

# **References**

[58] ULVAC, Arc Plasma Deposition System Brochure.

[59] R. I. Masel, Principles of Adsorption and Reaction on Solid Surfaces, Wiley, New York, 1996.

[60] S.M. George, A.W. Ott, J.W. Klaus. Surface chemistry for atomic layer growth. *The Journal of Physical Chemistry*, 1996, 100(31): 13121-13131.

[61] R.L. Grob, F.B. Eugene, eds. Modern practice of gas chromatography. John Wiley & Sons, 2004.

[62] P.E. Miller, M.B. Denton. The quadrupole mass filter: basic operating concepts. *J. Chem. Educ*, 1986, 63(7): 617.

[63] P.L. Patterson, R.A. Gatten, J. Kolar, et al. Improved linear response of the thermal conductivity detector. *J. Chromatogr. Sci*, 1982, 20: 27-32.

[64] K.S. Harsha. Principles of vapor deposition of thin films. Elsevier, 2005.

[65] K. Wasa, T. Nagai, S. Hayakawa. Structure and mechanical properties of rf sputtered SiC films. *Thin Solid Films*, 1976, 31(3): 235-241.

[66] R.A. Surmenev. A review of plasma-assisted methods for calcium phosphate-based coatings fabrication. *Surface and Coatings Technology*, 2012, 206(8): 2035-2056.

[67] O. Deutschmann, S. Tischer, C. Correa, et al. DETCHEM Software package, 2.5 ed., www.detchem.com, Karlsruhe, 2014.

[68] Z. Zhao, M. Chaos, A. Kazakov, et al. Thermal decomposition reaction and a comprehensive kinetic model of dimethyl ether. *International Journal of Chemical Kinetics*, 2008, 40(1): 1-18.

[69] N. Kurimoto, B. Brumfield, X. Yang, et al. Quantitative measurements of HO 2/H 2 O 2 and intermediate species in low and intermediate temperature oxidation of dimethyl ether. *Proceedings of the Combustion Institute*, 2015, 35(1): 457-464.

[70] K. Sun, W. Lu, F. Qiu, et al. Direct synthesis of DME over bifunctional catalyst: surface properties and catalytic performance. *Applied Catalysis A: General*, 2003, 252(2): 243-249.

[71] F.S. Ramos, A.M.D. de Farias, L.E.P. Borges, et al. Role of dehydration catalyst acid properties on one-step DME synthesis over physical mixtures. *Catalysis Today*, 2005, 101(1): 39-44.

[72] J.L. Li, X.G. Zhang, T. Inui. Improvement in the catalyst activity for direct synthesis of dimethyl ether from synthesis gas through enhancing the dispersion

of CuO/ZnO/γ-Al2O3 in hybrid catalysts. *Applied Catalysis A: General*, 1996, 147(1): 23-33.

[73]  T. Ogawa, N. Inoue, T. Shikada, et al. Direct dimethyl ether synthesis. *Journal of natural gas chemistry*, 2003, 12(4): 219-227.

[74]  G.R. Moradi, S. Nosrati, F. Yaripor. Effect of the hybrid catalysts preparation method upon direct synthesis of dimethyl ether from synthesis gas. *Catalysis communications*, 2007, 8(3): 598-606.

[75]  J.H. Flores, D.P.B. Peixoto, L.G. Appel, et al. The influence of different methanol synthesis catalysts on direct synthesis of DME from syngas. *Catalysis today*, 2011, 172(1): 218-225.

[76]  I.N. Remediakis, F. Abild-Pedersen, J.K. Nørskov. DFT study of formaldehyde and methanol synthesis from CO and $H_2$ on Ni (111). *The Journal of Physical Chemistry B*, 2004, 108(38): 14535-14540.

[77]  F. Studt, F. Abild-Pedersen, Q. Wu, et al. CO hydrogenation to methanol on Cu–Ni catalysts: theory and experiment. *Journal of catalysis*, 2012, 293: 51-60.

[78]  J. Nerlov, I. Chorkendorff. Methanol synthesis from $CO_2$, CO, and $H_2$ over Cu (100) and Ni/Cu (100). *Journal of Catalysis*, 1999, 181(2): 271-279.

[79]  X. Huang, L. Ma, M.S. Wainwright. The influence of Cr, Zn and Co additives on the performance of skeletal copper catalysts for methanol synthesis and related reactions. *Applied Catalysis A: General*, 2004, 257(2): 235-243.

[80]  X.M. Liu, G.Q. Lu, Z.F. Yan, et al. Recent advances in catalysts for methanol synthesis via hydrogenation of CO and $CO_2$. *Industrial & engineering chemistry research*, 2003, 42(25): 6518-6530.

[81]  S. Mousavi, A. Zamaniyan, M. Irani, et al. Generalized kinetic model for iron and cobalt based Fischer–Tropsch synthesis catalysts: Review and model evaluation. *Applied Catalysis A: General*, 2015, 506: 57-66.

[82]  B.H. Davis. Fischer–Tropsch synthesis: reaction mechanisms for iron catalysts. *Catalysis Today*, 2009, 141(1): 25-33.

[83]  G.P. Van Der Laan, A. Beenackers. Kinetics and selectivity of the Fischer–Tropsch synthesis: a literature review. *Catalysis Reviews*, 1999, 41(3-4): 255-318.

[84]  F.G. Botes, B.B. Breman. Development and testing of a new macro kinetic expression for the iron-based low-temperature Fischer-Tropsch reaction. *Industrial & engineering chemistry research*, 2006, 45(22): 7415-7426.

# **References**

[85]  M.E. Dry. The fischer–tropsch process: 1950–2000. *Catalysis today*, 2002, 71(3): 227-241.

[86]  E.S. Hecht, G.K. Gupta, H. Zhu, et al. Methane reforming kinetics within a Ni–YSZ SOFC anode support. *Applied Catalysis A: General*, 2005, 295(1): 40-51.

[87]  V.M. Janardhanan, O. Deutschmann. CFD analysis of a solid oxide fuel cell with internal reforming: Coupled interactions of transport, heterogeneous catalysis and electrochemical processes. *Journal of Power Sources*, 2006, 162(2): 1192-1202.

[88]  L. Maier, B. Schädel, K.H. Delgado, et al. Steam reforming of methane over nickel: development of a multi-step surface reaction mechanism. *Topics in catalysis*, 2011, 54(13-15): 845.

[89]  K.H. Delgado, L. Maier, S. Tischer, et al. Surface reaction kinetics of steam-and $CO_2$-reforming as well as oxidation of methane over Nickel-based catalysts. *Catalysts*, 2015, 5(2): 871-904.

[90]  M. Lee, C.B. Reuter, Y. Suzuki, et al. Numerical study of wall-stabilized cool flames. *Proceedings of the Asian Conference on Thermal Sciences 2017, 1st ACTS*, Korea.

# Publication List

**International Conferences**

(1) "PLIF measurement of OH generated with pulsed arc discharge for radical quenching study", W. Lin, S. WAN, Y. Suzuki, 35th Int. Symp. Combustion (Combustion 2014), Work-in-Progress Poster, San Francisco, W1P053, 2014.

(2) "Wall chemical effect on DME weak flame in a rectangular micro channel with a streamwise temperature gradient", S. WAN, Y. Fan, K. Maruta, Y. Suzuki, The 10th Asia-Pacific Conference on Combustion, Beijing, 2015.

(3) "Investigation of Wall Chemical Effect on DME Weak Flame in a Rectangular Micro Channel with a Streamwise Temperature Gradient", S. WAN, Y. Fan, K. Maruta, Y. Suzuki, 36th Int. Symp. Combustion (Combustion 2016), Work-in-Progress Poster, Seoul, #8246, 2016.

(4) "HCHO-PLIF Measurement of DME Weak Flame for Investigation of Wall Chemical Effect", S. WAN, Y. Fan, K. Maruta, Y. Suzuki, 36th Int. Symp. Combustion (Combustion 2016), Work-in-Progress Poster, Seoul, #8503, 2016.

(5) "Investigation of Wall Chemical Effect on Weak Flame with GC and PLIF", S. WAN, Y. Fan, K. Maruta, Y. Suzuki, The 11th Asia-Pacific Conference on Combustion, Sydney, 2017, Accepted.

**Domestic Conferences**

(1) "PLIF Measurement of Discharge-based OH on Patterned Alumina for Radical Quenching Study", W. Lin, S. WAN, Y. Suzuki, The 51st National Heat Transfer Symposium of Japan, Hamamatsu, 2014.

(2) "Wall chemical effect on weak flame in a micro channel with a streamwise temperature gradient", S. WAN, Y. Fan, K. Maruta, Y. Suzuki, The 52nd National Heat Transfer Symposium of Japan, Fukuoka, 2015.

(3) "Investigation of radical quenching for the DME/air weak flame in a rectangular micro channel with a streamwise temperature gradient", S. WAN, Y. Fan, K. Maruta, Y. Suzuki, The 53rd Symposium (Japanese) on Combustion, Tsukuba, 2015.

(4) "Investigation of wall chemical effect on DME/air weak flame by HCHO-PLIF", S. WAN, Y. Fan, K. Maruta, Y. Suzuki, The 53rd National Heat Transfer Symposium of Japan, Osaka, 2016.

(5) "HCHO-PLIF Measurement of DME Weak Flame for Wall Chemical Effect Study", S. WAN, Y. Fan, K. Maruta, Y. Suzuki, The 54rd Symposium (Japanese) on Combustion, Sendai, 2016.

(6) "Effect of Wall Surface Reaction on a DME/air Weak Flame in a Micro Flow Reactor with a Streamwise Temperature Distribution", S. WAN, Y. Fan, K. Maruta, Y. Suzuki, The 54th National Heat Transfer Symposium of Japan, Saitama, 2017.